The development and characterization of precursor-derived silicon carbide based materials for direct power extraction applications

YiHsun Yang

A dissertation

submitted in partial fulfillment of the

requirements for the degree of

Doctor of Philosophy

University of Washington

2018

Reading Committee:

Fumio S. Ohuchi, Chair

Marjorie A. Olmstead

Rajendra K. Bordia

Program Authorized to Offer Degree:

Materials Science and Engineering

©Copyright 2018
YiHsun Yang

University of Washington

Abstract

The development and characterization of precursor-derived silicon carbide based materials for direct power extraction applications

YiHsun Yang

Chair of the Supervisory Committee:

Professor Fumio S. Ohuchi

Materials Science and Engineering

Direct power extraction is a method that converts thermal energy into electric energy without an intermediate state, such as mechanical energy. Despite the concept being proposed decades ago, there is not a real commercial implement due to various issues. In this thesis, the issue of suitable channel electrode materials will be addressed.

A novel class of SiC/C ceramic composite materials through a polymer-precursor-derived route with tailored compositions for high temperature electric materials has been developed by the collaboration between Clemson University (CU) and University of Washington (UW). CU investigated the fabrication and processing conditions, including hot-pressed (HP) and polymer-infiltration-pyrolysis (PIP); UW investigated the effects of different processes of fabrication, the resultant stoichiometry (specifically C/Si) nature of the carbon phase and its surface properties.

In the presented SiC/C system, a thorough characterization has been done including analyzing structural, morphological, elemental and surface electronic data. X-ray diffraction (XRD) was used for structure analysis; scanning electron microscope (SEM) was for morphologic analysis; X-ray photoelectron spectroscopy (XPS) and glow discharge optical emission spectroscopy (GDOES) was used for elemental analysis; ^{29}Si NMR provided bulk silicon chemical state; Raman spectra provided further information on carbon species. There are a few custom designed experimental apparatuses, including electrical resistivity measurement at elevated temperature to ensure suitability for electrode applications, in-situ Auger electron spectroscopy (AES) for high temperature surface property analysis, and thermionic emission energy distribution (TEED) developed to decipher the material's work function at desired temperature. We utilized two methods relating to thermionic emission to measure the material's work function. The first method takes advantage of the Richardson Dushman equation; it describes a relationship between total emission current density and work function for certain temperature range. Alternatively, the work function at certain temperature can be evaluated using the TEED technique by comparing the on-set energy with a tungsten reference sample.

In our investigation, specimens from the HP process are mostly 6H polytype, whereas specimens from PIP process created 3C polytype. The chemical compositions can be adjusted through changing the portion of the additives in the process. The electrical resistivity in the measured temperature range shows semiconductor behavior. Using in-situ AES coupled with thermionic emission experiments, spontaneous graphitization occurred at elevated temperature for all the specimens. The work function acquired from the two thermionic related methods did not agree with each other.

However, the TEED method would be better for work function measurement at elevated temperature.

A successful outcome of this research will result not only in the emergence of reliable and affordable designed materials for direct energy extraction applications but also suitable for other future material exploratoration.

TABLE OF CONTAINS

Chapter 1 Introduction 1

Chapter 2 Technology background... 8

2.1 Brief history of MHD channel electrode materials development 8

2.2 The nature of polytype for silicon carbide 11

2.3 The selected SiC fabrication method: Polymer derived synthesis 12

Chapter 3 Thermionic emission and energy distribution for surface investigation 16

3.2 Thermionic emission under weak external field 16

3.3 Thermionic emission for semiconductor.. 17

Chapter 4 Experimental Procedures & Development of Experimental Apparatus.. 20

4.1 Polymer-derived silicon carbide, polymer-infiltration-pyrolysis and hot-pressed.. 20

4.2 Customized high temperature electrical resistivity measurement apparatus 26

4.3 Versatile UHV Chamber for Surface Analysis 33

4.4 In-situ Auger electron spectroscopy... 34

4.5 Thermionic emission and its energy distribution 35

4.6 Specimen characterization 39

Chapter 5 Structural, morphology and elemental information of polymer derived silicon carbide 41

5.1 Structure analysis – 41

5.2 Electrical resistivity measurement at elevated temperature 58

Chapter 6 Thermionic emission, electron energy distribution and in-situ Auger Electron Spectroscopy 70

6.1 Thermionic emission achieved from direct heating and in-situ AES.......... 70

6.2 In-direct heating AES and thermionic emission and energy distribution ... 76

6.3 Energy distribution of thermionic emitted electrons.................................. 92

6.4 Detailed procedure and interpretation for TEED spectra............................ 99

Chapter 7 Conclusion 103

7.1 Development of HP and PIP method for polymer derived silicon carbide synthesis and the properties of the resulting samples 103

7.2 Proposed energy band structure for polymer derived silicon carbide....... 105

7.3 Areas of future work 107

Appendix 1. Spectroscopic Two-Color Pyrometry... 1

A1.1 Principle of the method: 1

A1.2 Instruments: 5

A1.3 Procedure: 5

A1.4 Results: 7

A1.5 Discussions and future work: 11

Reference 13

List of Figures

Figure 1.1. The simplified schematic diagram for the working principle of MHD generator. (a) a plume of ionized gas moves through a magnetic field (vertical) and the electrodes (horizontal) collects the induced power, (b) the arrows show the direction of magnetic field, plasma flow and electric field. 3

Figure 1.2. Electrical resistivity of potential electrode materials. (reproduced from Ceramic for Coal-fired MHD Power Generation) [7]... 5

Figure 2.1 Left: the chosen precursor for SiC, *Allylhydridopolycarbosilane* (Starfire SMP-10); center: additive for extra carbon source, *divinyl benzene*; right: boron additive for sintering, *decaborane*, $B_{10}H_{14}$. 15

Figure 4.1. A diagram of the PDCs procedure for fabricating SiC/C. 21

Figure 4.2. (a)*: Vacuum die set under uniaxial loading applied by an electric hydraulic press*; (b) pressed preceramic pellets; (c) SiC/C pellets after PIP synthesis.................... 25

Figure 4.3. Polymer infiltration set up including a flask containing the SiC pellets and a funnel containing liquid SMP10 polymer (a) the set up under vacuum when the lower valve is closed. (b) Lower valve is open and the liquid polymer is flowing down into the flask. 26

Figure 4.4(a) a typical design utilizing Al_2O_3 and Pt to construct the measuring apparatus; (b) a more detailed design showing the pushing mechanism on two sides of the sample and (c) a different design made use of gravity and vertically fastened the sample and secured the contacts. 27

Figure 4.5. Simple wrapping technique to ensure the contact between sample and wires. [44] 29

Figure 4.6 (a) Schematic diagram of two-wire resistance measurement; (b) schematic diagram of four-wire resistance measurement. 30

Figure 4.7. Modified "Matryoshka" design for the electrical conductivity measuring apparatus with the sample installed by the wrapping mechanism. 31

Figure 4.8. The UHV chamber setup has the capability for Auger electron spectroscopy, thermionic emission, ion gun and more. 34

Figure 4.9. The basic cylindrical mirror analyzer (CMA) and block diagram for Auger electron spectroscopy. [46] 35

Figure 4.10 Sample holding apparatus: (a) and (b) direct heating, sample is held with Pt wire and graphite wrap as previously described, heating wires are sandwiched with alumina plate; (c) and (d) indirect heating, sample is held on a stainless-steel plate (Kimball physics) with spark welded Tantalum ribbon. Plates are isolated using ceramic eV parts (Kimball physics). 37

Figure 5.1 XRD patterns of PIP specimens, (a) zero percent boron additive and zero percent carbon additive (denoted as 0C); (b) zero percent boron additive and five percent carbon additive (denoted as 5C); (c) zero percent boron additive and ten percent carbon additive (denoted as 10C); (d) zero percent boron additive and fifteen percent carbon additive (denoted as 15C). 42

Figure 5.2 XRD patterns of silicon carbide from PIP process with zero weight percent carbon additive (PIP0C, red), five weight percent carbon additive (PIP5C, blue), ten weight percent carbon additive (PIP10C, green) and fifteen weight percent carbon

additive (PIP15C, purple). The silicon carbide 3C polytype reference is marked as black stick. 43

Figure 5.3 XRD patterns of silicon carbide from HP process with zero weight percent carbon additive (HP(1B0C), red), one weight percent carbon additive (HP(1B1C), blue), three weight percent carbon additive (HP(1B3C), green) and five weight percent carbon additive (HP(1B5C), purple). The silicon carbide 6H polytype reference is marked as black triangle and the graphite reference is marked as black solid circle. 45

Figure 5.4. (a) C 1*s,* (b) O 1*s*, and (c) Si 2*p* XPS spectra for hot-pressed SiC/C specimen fractured surface with different amounts of carbon and boron dopant 47

Figure 5.5 GDOES spectra for silicon carbide fabricated through polymer infiltration and pyrolysis procedure. 49

Figure 5.6 Carbon to silicon atomic ratio versus sputtering depth for silicon carbide specimens fabricated through polymer infiltration and pyrolysis (PIP) procedure. 49

Figure 5.7 GDOES spectra for silicon carbide fabricated through hot-press procedure for HP:1B0C, HP:1B1C, HP:1B3C and HP:1B5C. 51

Figure 5.8 Carbon to silicon atomic ratio versus sputtering depth for silicon carbide specimens fabricated through hot-pressed (HP) procedure 52

Figure 5.9 Carbon to silicon ratio measured from GDOES plotted against nominal excess carbon from the weight percent of divinyl benzene, carbon additive for PIP and HP specimens. 52

Figure 5.10 ^{29}Si NMR spectra for three HP specimens, 1B0C (black), 1B1C (red), and 1B5C (blue). 54

Figure 5.11 (a) Raman spectrum of CVD silicon carbide; (b) Raman spectrum of commercial graphite.. 55

Figure 5.12 SEM images (left), optical microscopy (center) and Raman spectra (right) for (a) PIP0C, (b) PIP5C, (c) PIP10C and (d) PIP15C.. 56

Figure 5.13 Raman spectra of hot-pressed SiC with 1 weight percent of boron additive and 0, 1, 3 and 5 weight percent carbon additive were obtained. 57

Figure 5.14 Comparison between data taken from procedure 1 (green solid triangle) and procedure 2 (red open circle). 59

Figure 5.15. Electrical resistivity versus temperature for samples B(0B1C), C(1B5C), D(1B1C) and E(1B0C). 61

Figure 5.16. Arrhenius plots of the conductivity data from samples B, C, D and E. Activation energy is shown for each sample in two different temperature range. 62

Figure 5.17. Attempts to fit the electrical conductivity data by (a) small polaron hopping (SPH) and (b) variable range hopping (VRH) models.. 64

Figure 5.18. Electrical resistivity versus temperature for specimens PIP(0B0C) (red, open circle), PIP(0B5C) (blue, open square) and PIP(0B15C) (green, open triangle)............. 67

Figure 5.19. Arrhenius plots of the conductivity data from PIP specimens 0B0C, 0B5C and 0B15C. Activation energy is shown for each sample in two different temperature range.. 68

Figure 5.20. Electrical resistivity versus temperature for all specimens from the above sections are plotted in semi-log scale.. 69

Figure 6.1. AES taken from SiC single crystal to demonstrate the DC voltage brought into the spectrum... 71

Figure 6.2. A series of Auger electron spectra taken from (a) silicon carbide single crystal, (b) HP(0B1C), (c) HP(1B5/9.5C) and (d) HP(1B1/3.9C). 72

Figure 6.3. Thermionic emission data taken from (a) silicon carbide single crystal, (b) HP(0B1C) sample, and (c) HP(1B1/3.9C) sample; Richardson –Dushman of the TE data obtained from (d) silicon carbide single crystal, (e) HP(0B1C) sample and (f) HP(1B1/3.9C) sample. 74

Figure 6.4. A series of Auger electron spectra taken from silicon carbide specimen (0B0C) prepared from PIP route, as installed (red), sputtered 30 mins (blue), annealed to 640 ^{o}C (green), annealed to 740 ^{o}C (purple), annealed to 850 ^{o}C (brown), annealed to 950 ^{o}C (light blue), and annealed to 1000 ^{o}C (black) from top to bottom respectively................ 75

Figure 6.5(a) simplified setup for collecting thermionic emission from Joule heating; (b) simplified setup for collecting thermionic emission from indirect heating, mainly thermal radiation. 78

Figure 6.6 Experimental setup for control experiment 0, heating element only............... 78

Figure 6.7 Emission current, I_S, plotted versus retarding voltage, V_R for (a) V_B = 0 to V_B = 8, (b) V_B = 8 to V_{B1} = 15 and (c) first derivative of Is for V_B = 1 to V_B = 5 at 1030 ^{o}C. 79

Figure 6.8 Thermionic emission current versus retarding voltage, taken at (a) 1080 ^{o}C, (b) 1105 ^{o}C and (c) 1300 ^{o}C, varying V_{B1} from 0 volt to 15 volts. 80

Figure 6.9 Emission current at various temperature were plotted with respect to the difference between heating voltage and bias voltage, V_H – V_B. Figure on the right is the enlargement for the figure on the left 81

Figure 6.10 Emission current versus retarding voltage for PIP0B1C sample for various V_{B2}, at (a) $V_B = 0$, (b) $V_B = 5$, (c) $V_B = 10$ volts.. 82

Figure 6.11 Emission current versus retarding voltage for $V_H = V_B$ at the same temperature (959 °C) while chamber pressure is at 10^{-6} Torr, 10^{-7} Torr and 10^{-8} Torr for (a), (b) and (c), respectively.. 82

Figure 6.12 Auger electron spectra for polymorphous tungsten acquired at room temperature (blue) and at 1000 °C (red). 84

Figure 6.13 (a) Thermionic emission current versus retarding voltage for $V_{B2} = -8$ at the above temperature for polycrystalline tungsten; (b) emission current was plotted with respect to temperature and (c) the Richardson plot. 85

Figure 6.14 Emission current versus retarding voltage for sample PIP0B0C with $V_{B2} = -8$ to +8, $V_H = V_B$ at (a) 977 °C, (b) 993 °C and (c) 1009 °C at 1.2×10^{-8} Torr..................... 87

Figure 6.15(a) emission current versus retarding voltage at various temperature for $V_{B2} = -8$ and (b) emission current versus retarding voltage at various temperature for $V_{B2} = -4$. 88

Figure 6.16(a) Emission current plotted with temperature (K) for sample PIPSiC0B1C with $V_{B2} = -8$ and -4; (b) Richardson-Dushman plot for (a)... 89

Figure 6.17 Auger spectra of the PIPSIC, red: as installed, blue: after Ar ion bombardment for 30 mins, green, pink, orange, light blue and black is acquired at 640 °C, 740 °C, 850 °C, 950 °C and 1000 oC, respectively... 90

Figure 6.18 (a) Thermionic emission current versus retarding voltage for $V_{B2} = -8$ at the above temperature for HPSiC_1B1C; (b) emission current was plotted with respect to temperature and (c) the Richardson-Dushman plot. 91

Figure 6.19 In-situ Auger spectra from a polycrystalline tungsten after the surface was sputtered by Ar ion and annealed at 1000 ^{o}C. The temperature labelled is the temperature when the spectra were acquired. 91

Figure 6.20 A typical thermionic emission versus retarding voltage spectrum and its first derivative with specimen bias voltage (V_{B2}) equals to 8 volts. Black: total current versus retarding voltage, red: the derivative of the total current versus retarding voltage. 93

Figure 6.21 Thermionic emission energy distribution of PIP0C silicon carbide at (a) 958, (b) 968, (c) 994 and (d) 1009 ^{o}C with V_{B2} equals to -1, -2, -3, -4, -5, -6, -7, and -8 volts for blue, green, pink, light blue, brown, grey, black and red, respectively....................... 94

Figure 6.22 The peak positions of TEED with respect to sample bias voltage, with temperature at 958, 968, 994 and 1009 ^{o}C for red, blue, green and purple, respectively. 95

Figure 6.23 The FWHM of TEED with respect to V_{B2} for temperature equals to 958, 968, 994 and 1009 ^{o}C. 95

Figure 6.24 Energy distribution of emitted current from tungsten. (a) data was acquired while heating and (b) data was acquired during cooling. Chamber pressure is around 1×10^{-8} Torr. 96

Figure 6.25 Energy distribution of emitted current from tungsten at chamber pressure around 1×10^{-7} Torr. 97

Figure 6.26 Normalized TEED acquired from HPSiC for (a) V_{B2} equals -4 volts and (c) V_{B2} equals -8 volts; normalized TEED acquired from PIPSiC for (b) V_{B2} equals -4 volts and (d) V_{B2} equals -8 volts. 98

Figure 6.27 (a) Emission spectra versus retarding voltage for tungsten from various temperature, (b) adjust the retarding voltage by 8 volts to compensate specimen bias

voltage (V_{B2}), (c) x-axis multiply by -1 so it's showing electron energy instead of retarding voltage, and (d) set the fermi energy to zero using work function deduced from RD plot for tungsten and the on-set energy to 4.36 eV. 100

Figure 6.28 Adjusted TEED spectra for tungsten (top), PIP0C silicon carbide (middle) and HP silicon carbide (bottom). The energy was adjusted for tungsten on-set energy as 4.36 eV for all three figures. 101

Figure 7.1 Simplified band diagram for tungsten, PIP0C silicon carbide and HP1B1C silicon carbide. 106

ACKNOWLEDGEMENTS

The author would like to thank the Department of Energy (Grant#: DE-FE0023142) for providing the financial support necessary to conduct the research contained in the dissertation. There are countless people the author wish to express the appreciation, including but not limited to the reading committee Professor Fumio Ohuchi, Professor Marjorie Olmsted and Professor Raj Bordia; department lab staffs including: Tuesday Kuykendall and Tatyana Galenko. The author would also like to express special appreciation to his family, Yun-Pei, Oliver and Peter and his parents, Tung-Jung and Be-Ling for their unflagging support.

Chapter 1 Introduction

Inflated demand for limited natural resources calls for innovative sustainable, clean energy sources. While clean energy may not take over as the main power supply, researchers and scientists are keen to make the most use of current power sources. Direct energy extraction was proposed to ease the tension between the limited supply and the increasing demand of energy. Direct energy extraction is a concept of directly converting thermal and kinetic energy to usable electrical energy. Thermoelectrics (TE), thermionic energy conversion (TEC) and magnetohydrodynamics (MHD) are a few examples for direct energy extraction. Thermoelectrics utilize the mobility difference of different charge carriers in a temperature gradient. [1] Thermionic energy conversion, on the other hand, is based on the evaporation of electrons from conductors at high temperatures. [2] Lastly, magnetohydrodynamics (MHD) power generators transform the combustion energy of a gas into electric power similarly to how a turbo generator does, except the moving part is instead a thermally ionized gas. [3]

Our research is to make the best use of current fossil fuels by providing an extra step in the power generation cycle: MagnetoHydroDynamics (MHD) power generation. Direct energy extraction via MHD principles offers a potential step improvement in thermal efficiencies energy systems utilizing traditional turbomachinery. While MHD power generation drew significant interest from researchers in the 60s, the focus has been shifted to other interests due to electrode materials issues. The channel electrode materials must be able to withstand extremely high temperatures and complicated

chemicals including seeds and coal slag depending on the combustion type. [4] As technology advanced, the preferred combustion method is no long high sulfur containing coal combustion but potassium seeded oxy-fuel combustion. [5] The change of fuel drastically reduced the requirement for the channel electrode materials because of the cleaner combustion and thus an opportunity opened for researchers.

The history of MHD power generation can be traced to the last century. In the 1930s and early 1940s a concentrated effort was devoted to the development of two types of gas turbines: the mechanical turbine using moving blades and the electrical turbine making use of the interaction between conducting fluids, usually in the gas phase (plasma). The mechanical turbine found rapid implementation in the electrical power industry. The latter technology for power generation is called magnetohydrodynamic (MHD) generator. As shown in **Figure 1.1**, when a conductor moves through a magnetic field, it creates an electric field perpendicular to the magnetic field and the direction of motion. This is per Faraday's law of induction and quantified with Lorentz's law. In Lorentz's law, a charged particle moving in a constant magnetic field can be described using

$$F = QvB$$

where F is the force acting on the charged particle, Q is charge of particle, V is the velocity of particle and B is magnetic field in the direction perpendicular to the motion.

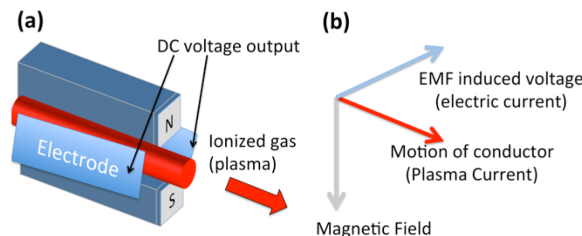

Figure 1.1. The simplified schematic diagram for the working principle of MHD generator. (a) a plume of ionized gas moves through a magnetic field (vertical) and the electrodes (horizontal) collects the induced power, (b) the arrows show the direction of magnetic field, plasma flow and electric field.

It started to draw attention from physicists and engineers and gradually became a laboratory reality in the 1960s. The MHD generator transforms the internal energy of a gas into electric power in much the same way that a turbine generator does because the basic physical phenomena that are employed are the same in both cases. For turbine generators the energy of the gas is converted into the motion of a solid conductor by means of turbine blades and a connecting mechanical linkage. For an MHD generator, the gas itself is the conductor, travelling through a magnetic field, and consequently generates electricity. The conductor moving through a magnetic field gives rise to an electromotive force and a flow of current in accordance with Faraday's law of induction. At that time, electrical manufacturers recognized the economic and technological potential of MHD power generation, by some utilities and by military agencies. These groups provided early support for research in the field of MHD power generation. However, as result of the construction of the first economical nuclear power plant and the slowing of the development of MHD power generation, the commercial interest of MHD began to wane. The major obstacle preventing this technology from commercialization is its material durability issue. In order to increase the electrical conductivity of the combustion product, alkaline metal salts (e.g., K_2CO_3) are added to the gas. The "seeded" gas has to be heated up to 2800 ^{o}K as it passes through the magnetic field where 10 - 20% of the thermal energy is converted to electrical power. Downstream to this MHD phase, a steam turbine can be coupled with about 40% conversion and it makes the overall process from 50 - 60% efficient.

The research and development activities for MHD power generation have been quiet for decades. However, advances in the materials science and engineering motivates us to revisit the issue. As time goes by, people now are no longer interested in coal-fired MHD generation because of environmental issues. Over the past fifteen years, a clean oxy-fuel combustion type of MHD has drawn a significant amount of attention. [6] This transition made the criteria for the electrode materials less strict. Since people are no longer interested in coal-fired combustion, slag contamination is no longer the primary issue to resolve for electrode research and development.

The electrical resistivity as a function of temperature of many prospective materials is shown in **Figure 1.2**. [7] It varies less across the measured temperature range for metallic type materials (Molybdenum, graphite, ZrB_2 and doped $LaCrO_3$) than the oxide type materials; there is a large variation with temperature for the semiconducting and partially ionic conducting ceramics (UO_2, Zirconia based oxides and $FeAl_2O_4$). Silicon carbide and graphite stand out among these materials. Silicon carbide is known for its high level of corrosion and erosion resistance with moderate electric conductive whereas graphite is a metallic type conductor with minimal resistance to corrosion and erosion. Silicon carbide may be one of the oldest materials, which was found in meteoroid. It was discovered and synthesized in 1893 by Edward G. Acheson. [8] It is currently one of the most interesting ceramic materials due to its superior properties, such as high hardness, high temperature strength, low bulk density relative to metal, and high oxidation resistance. In this thesis, a composite material consisting of silicon carbide and graphite will be discussed. An in-depth description of these materials is summarized in the following chapter.

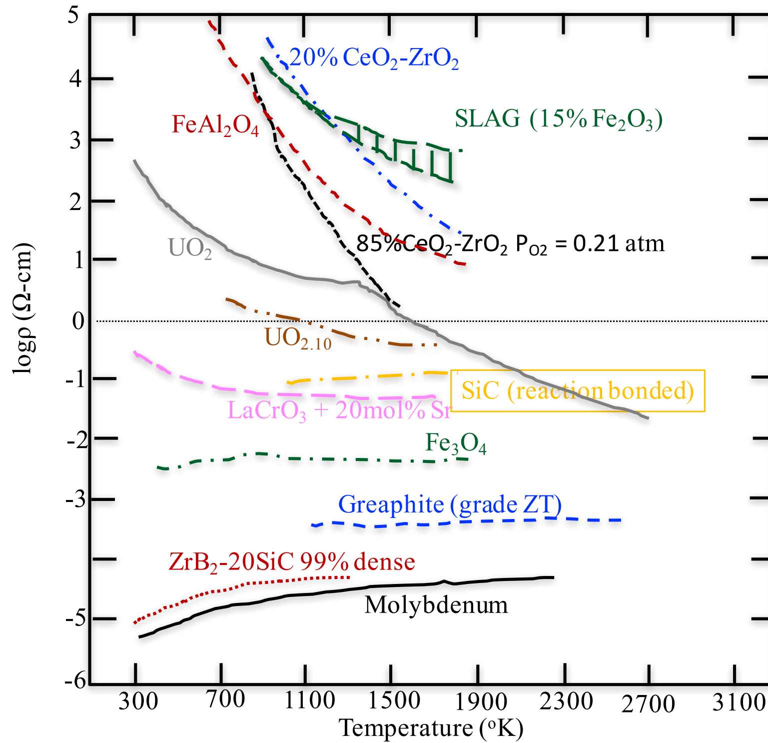

Figure 1.2. Electrical resistivity of potential electrode materials. (reproduced from Ceramic for Coal-fired MHD Power Generation) [7]

In the past, people have identified the objective for MHD power generation project is to develop coal-fired commercial open cycle MHD system. [9] There is one major difference between the past coal-fired and the current oxy-fuel; coal usually contains silicon, iron and sulfur. Electrode materials should meet not only those high temperature criteria but also have to withstand corrosion from coal slag. As addressed in 1979 [7], specific criteria for properties of MHD electrode materials have been proposed in **Table 1**. Multiple international joint research projects had set out to tackle this materials issue, however none of them came up with a promising solution.

Table 1 Proposed properties of MHD electrode materials [7]

1	Electrical conductivity (> 10^{-1} Ω^{-1} cm^{-1}) at current density of more than 1 A/cm^2.
2	Small temperature dependence of the electrical conductivity.
3	Good thermionic (electron) emission.
4	Corrosion resistance: to potassium seed and coal slag.
5	Erosion resistance: to the high velocity gas, to liquid droplets and to particulates in the gas stream.
6	Good thermal conductivity: to provide for adequate heat flux and to reduce thermal gradients and thermal stress.
7	Oxidation (or reduction) resistance: stability in the MHD at oxygen partial pressures of 10^{-4} – 10^{-2} atm.
8	Thermal stress damage resistance
9	Compatibility with insulator and combustion products.

To address the need for a stable, high temperature electrode, we propose a new polymer-derived composite material consisting of silicon carbide and graphite. The precursors have been selected for simplicity; however, the process could introduce considerable flexibility in its compositions. The purpose of this thesis is to evaluate the proposed SiC/C composite material as a candidate for high temperature electrode applications. It also supplies new tools for studying materials including the custom developed techniques for both the hardware and the software of high temperature electrical resistivity measurement, in-situ Auger electron spectroscopy (AES) coupled thermionic emission (TE) for surface analysis, and thermionic emission energy distribution (TEED) for learning the material's electronic structures for high temperature applications. These unprecedented tool sets would not only work for studying the presented materials but they can be further utilized for high temperature material exploration.

This thesis investigates many aspects of this novel class of materials including basic physical properties such as crystal structure by X-ray diffraction (XRD), morphology by electronic microscopy, compositional analysis by X-ray photoelectron spectroscopy (XPS), glow discharge optical emission spectroscopy (GDOES), silicon nuclear magnetic resonance (^{29}Si NMR), microscopic Raman spectroscopy and in-situ Auger electron spectroscopy (AES). Another emphasis of this thesis is on the development of custom designed research apparatus. Due to lack of suitable commercially available instruments, three custom designed experimental apparatuses were developed. This includes (**a**) a high temperature electrical resistance measurement executed with an in-house design apparatus placed within a commercial tube furnace, (**b**) an in-situ AES coupled with thermionic emission (TE) and (**c**) a thermionic emission energy distribution (TEED). The in-situ AES coupled with thermionic emission (TE) provides real-time surface analysis at elevated temperature. A rigorous thermionic emission (TE) and thermionic emission energy distribution (TEED) analysis were performed to evaluate the material electronic structure in an elevated temperature range that is close to MHD electrode working temperature. For thermionic emission, two different types of emission current were collected: emission from direct heating (Joule heating) and emission from indirect heating. A reasonable comparison between direct heating and indirect heating were made to elucidate the emission properties. For TEED, the on-set of emission current serves as an indicator of the vacuum level edge. The peak width of emission distribution under weak external field was evaluated and real distribution without bias can be estimated.

Chapter 2 Technology background

2.1 Brief history of MHD channel electrode materials development

The main thrust of the international MHD development effort was primarily centered in the U.S. and the former USSR. According to a joint report sponsored by the Defense Advanced Research Project Agency in 1974 [9], the USSR had a large MHD materials-development program while the United States had neglected MHD materials development. Both countries made progress but did not come up with viable technology before they shut off the program. The biggest issue was a problem with the electrodes which can be associated with corrosion, chemical resistivity with plasma, electric conductivity, and thermal conductivity.

There were a number of major MHD tests in the 70's and 80's. The first joint test between U.S. and USSR was done in 1974 [9], where the selected electrode materials were doped zirconia (85% ZrO_2-12%CeO_2-3%Y_2O_3 and 91% ZrO_2, 5% Nd_2O_3-4% Y_2O_3), chromite ($LaCrO_3$) and silicon carbide. The test was carried out under conditions with clean combustion and oxygen enriched air. The test lasted for 100 hrs with K_2CO_3 seed, and electrode wall temperature ~1500 ^oC. There was some cracking and seed penetration for zirconia, no significant erosion for chromite, and surface oxidation and forming of K_2SiO_3 for silicon carbide.

The second report came from another joint effort between the U.S. and USSR in the Soviet U-02 materials testing facility Phase I from 1973 to 1975 [10]. The electrode materials under testing were cerium and yttrium doped zirconia (88% ZrO_2 – 12% Y_2O_3, 82% ZrO_2 – 18% CeO_2, 50% ZrO_2 – 50% CeO_2, 25% ZrO_2 – 75% CeO_2, and 20% ZrO_2

– 78% CeO_2 – 2% Ta_2O_5). The test conditions were clean combustion similar to the previous one but K_2CO_3 was introduced as 50% aqueous solution. Total test time was 127 hrs and in which 100 hrs was under MHD operation condition. Out of 20 electrode pairs, 6 failed during the test. Failure was due to the melting of Pt wires from Joule heating of the electrode materials. Failure was observed with all compositions except 50% ZrO_2 - 50% CeO_2. Besides Pt melting, cracking, spalling, seed penetration observed from the tested specimens, cathode degradation was more extensive and all cathode surfaces were saturated with seed. Anodes showed less seed penetration. CeO_2 depletion was observed.

From same research collaboration Phase II final report [11], in addition to the zirconia (35% CeO_2 – 65% ZrO_2 and 78% CeO_2 – 20% ZrO_2 – 2% TaO_2) and chromite (Mg doped $LaCrO_2$), they also tested spinel type materials (75% $MgAl_2O_4$ – 25% Fe_3O_4 and 75% $FeAl_2O_4$ – 25% Fe_3O_4). The combustion scenario was similar with clean combustion, 50% oxygen enriched air, and K_2CO_3 introduced as 60% aqueous solution. For the Zirconia, most failures were found during the test and the electrodes were found with abundant cracking and spalling, significant erosion, and a modified microstructure. For the spinel, some degradation was observed for $MgAlO_4$-type and melting for $FeAlO_4$ type. Again, chromite showed most promising result, having the least deterioration.

Another set of experiments was performed to evaluate the combination of electrical and chemical properties of the candidate materials in 1978 [12]. The materials included 80% metallic (80% Pd – 20% Rh), chromite ($MgCrO_3$ and Cr_2O_3), and silicon carbide (CVD). The electrochemical corrosion was done in synthetic molten coal slag, which is the standard composition of non-volatile mineral impurities in coal. For the Pt-

Rh alloy, the (electrode) surface showed severe arc crater damage. Melting, corrosion, slag penetration, and platinum aluminide compounds formed on the surface were also observed. For $MgCr_2O_3$, metallic iron was found on surface. The composition of slag was enriched with Cr and depleted in Al and Fe. The grain boundary was penetrated by slag, and grains of complex spinel spalled off. As for Cr_2O_3, it also showed grain boundary penetration by slag and some metallic iron on surface. Corrosion products and rates were similar to $MgCr_2O_3$. Lastly, for silicon carbide, the main corrosion products on the surface were metallic iron, FeSi, and SiO_2. The maximum temperature the material can withstand is 1200 ^oC.

From Phase III of the Joint U.S. – U.S.S.R. test 1979 [13], they limited the candidate electrode materials to chromite and chromite zirconia. The test condition was identical to Phase II [11]. Having learned from Phase II, researchers decided to use $LaCrO_3$ doped with Mg, Al, a composite material that consisted of chromite ($La_{0.95}Mg_{0.05}CrO_3$) and zirconia (91% ZrO_2 – 9% Y_2O_3). Although various additives were added based on different assumptions, the electrode materials still showed degradation, erosion, cracking and spalling.

The last large scale MHD electrode materials investigation was done by researchers from Pacific Northwest National Laboratory (PNNL) in 1986. [14] Hafnia (indium, praseodymium and ytterbium doped) and chromite (yttrium, calcium and magnesium doped) were proposed. The electrical properties were analyzed and the testing channels have been built. However, due to the limitations of funding, the materials have never been tested. Despite the unfinished work on the development of channel electrodes, the change of objective conditions has shifted the interests of combustion type

as well as the requirement for channel electrode materials. As drilling technology advanced, fracking natural gas production increased 25% in the recent years [15], the focus of research shifted from coal-fired to oxy-fuel clean combustion MHD. Among the proposed materials, chromite has been ruled out due to potential carcinogenic risk and the rest of the candidates are ionic conductors and thus not ideal for long-term stability. As a reminder, a suitable electrode material for MHD applications should be (**a**) a moderate electricity conductor, (**b**) have low temperature dependence on electrical conductivity, (**c**) good thermionic emission properties, (**d**) have good corrosion and erosion resistance, (**e**) good re-dox resistance, (**f**) be resistant to thermal stress and (**g**) compatible with insulator and combustion products as proposed in **Table 1**. A composite material consisting with silicon carbide and graphite may be suitable as long as its electrical conductivity falls into the bracket.

2.2 The nature of polytype for silicon carbide

Silicon carbide is chemically simple considering it consists of two group four elements, carbon and silicon. However, it is structurally complex and there are many different crystallographic polytypes that can be found in silicon carbide. These polytypes differ from each other only in their stacking order in the [0001] direction. [13] Among the four most common polytypes, 3C, also known as β-SiC, is the only cubic polytype, which is mainly obtained when synthesized below 2000 ^{o}C. Above such processing temperature, it often creates a 6H or 4H hexagonal polytype or 15R rhombohedral polytype, which are referred as α-SiC, with wurtzite structure. [17] Under heat treatment, phase transformation occurs from β-SiC to α-SiC above 2000 ^{o}C for undoped silicon carbide.

There are methods to control the resulting polytype. For example, the addition of boron can lower the transformation temperature and also result in transformation to 4H polytype. [18]

The majority of silicon carbide is used as abrasive and still synthesized through Acheson process invented by Edward G. Acheson in 1893. [8] The method utilizes silica and carbon in a heated crucible. However, there is no way to control its polytype nor the purity of phase. While the Acheson process provides the least control on the resulting product, the Lely method provides a single crystal through sublimation. [19] There are methods providing control over structure. For instance, 3C-SiC or β-SiC can be synthesized utilizing chemical vapor deposition (CVD). [17] Among the three methods, Acheson does not offer control over structure and composition; the Lely method does provide fine control over structure but it is not a method typically used for introducing excess carbon and creating composite materials; CVD is good for making controlled structure but it is capital intensive and it is only suitable for small quantity productions. In order to test the capability for electrode materials, the specimens need to be machined into a certain shape. A fabrication method with conformity would be a huge advantage for the application. Due to the aforementioned reasons, we have chosen a novel method of fabrication which is capable of adjusting composition, has a low capital requirement, and is a conformal process.

2.3 The selected SiC fabrication method: Polymer derived synthesis

Silicon-based polymer-derived ceramics (PDCs) are ceramics fabricated by the pyrolysis of organosilicon polymers. The synthesis of PDCs was first introduced in

1960s [20]. Ainger and Herbert, Chantrell and Popper reported the production of non-oxide ceramics starting from molecular precursors. After a half century of development, it has gained a significant amount of attention. The first synthesis of a silicon carbide ceramic material from polycarbosilane was based on the work of Fritz [21] and the early work of Yijima [22] The Yijima Process was further developed for the synthesis of SiC ceramics at the end of 1970s. [23]

There are several advantages on the processability for using polymer-derived ceramics over conventional sintering. A specific characteristic of preceramic precursors is that they are polymeric in nature at the temperature at which they are shaped into components. Therefore, they can be subjected to a large variety of different plastic forming methods. For example, it can be formed through casting, injection moldings, pressing, tape casting, fiber drawing, coating and impregnating. [24] Furthermore, this technology offers a great advantage for controlling the composition by introducing other polymers.

Comparing with the traditional methods, the polymer derived process should provide advantages on cost, time or on the properties of the ceramics. Although the cost of the raw materials for the novel method is much higher than the conventional sintering, the polymer derived method still has several advantages. The process requires a much lower temperature, which means better energy efficiency; the ceramic's final properties are strongly dependent on the polymer composition so it provides predictable and engineer-able properties.

Silicon-based polymers have been proven to be ideal precursors for manufacturing silicon based ceramics, including binary systems such as Si-C [22,25] and

Si-N [26]; tertiary systems such as Si-C-N [27] and Si-C-O [28] and even the quaternary Si-B-C-N [29] system. The materials possess many unique features when compared to conventional sintering. For example, PDCs possess a unique structure which is consist of polycrystalline or amorphous nanodomains along with randomly distributed nanosized carbon cluster [13]. A detailed understanding of PDCs can be the key to deciphering the materials and make further improvements. However, due to the complexity of the materials, the structural properties relationship is a huge challenge and has not yet been developed. Knowing the capability of PDC silicon carbide, we needed to narrow down to a more realistic experimental condition. To be consistent, we started with simple polycarbosilane precursor, *Allylhydridopolycarbosilane (*AHPCS*), as the backbone structure.* The chemical formula for this precursor is shown **Figure 2.1**.

This precursor has been chosen because: **a**) on pyrolysis in an inert environment, it leads to stoichiometric SiC; **b**) it is commercially available (from Starfire System [31]). The Starfire product code for this precursor is SMP-10. To control carbon composition, the source molecule we chose is *divinyl benzene*. Divinyl functional groups react readily with allyl function groups on AHPCS in the presence of a catalyst and suitable conditions. Lastly, the additive *decaborane* was added for densification. Although densification does not happen until the sintering stage, adding in during the very beginning stage helps to get the most homogeneous mixing and further promotes uniform grain growth. Various ratios of the aforementioned compounds were formulated and of the presented results, only the 3C polytype and 6H polytype are successfully fabricated in the scope of discussion.

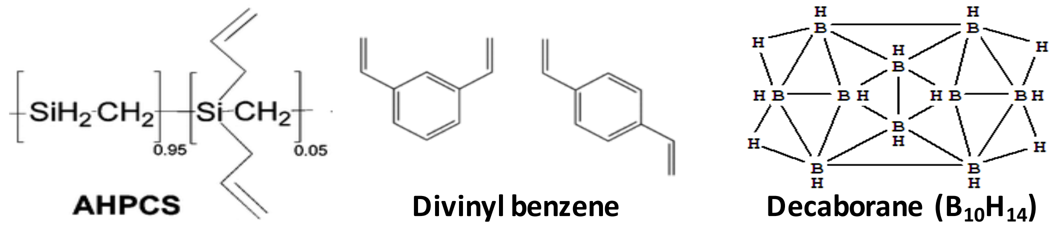

t7

Figure 2.1 Left: the chosen precursor for SiC, *Allylhydridopolycarbosilane* (Starfire SMP-10); center: additive for extra carbon source, *divinyl benzene*; right: boron additive for sintering, *decaborane*, $B_{10}H_{14}$.

Chapter 3 Thermionic emission and energy distribution for surface investigation

3.1 Thermionic emission and Richardson-Dushman equation

As mentioned, the materials are designed to work at elevated temperatures. In the target temperature range, it is unavoidable to deal with the thermionic emission phenomenon. The physics of thermionic emission for conductors was well developed and summarized. [32] [33] [34] The emitted current density follows the well-known Richardson-Dushman equation, which was derived based on thermodynamics and statistical mechanics to calculate the saturated current density *J* emitted from a metal at temperature *T*. The equation can be expressed as follows:

$$J(T) = A_R T^2 e^{-\frac{\Phi}{k_B T}}$$

where Φ is the material work function and A_R is the Richardson's constant is equal to $4\pi m k_B^2 e/h^3$, T is the temperature of the emitter surface and k_B is the Boltzmann's constant. Although Richardson's constant is a universal constant for pure metallic emitters, the experimental value often deviates from it. For example, some proposed that

$$A = A_R(1 - \bar{r}_e)$$

where and $\bar{r}$ is the zero-field reflection coefficient for incident electrons. [35]

3.2 Thermionic emission under weak external field

There are many assumptions made during the derivation and the most important are (a) the surface of the conductor is uniform, and (b) the applied field necessary to

produce saturation current is so weak that it may be set equal to zero. In the case of weak applied field, Herring and Nichols have demonstrated that the work function is reduced by an applied field with field strength E by

$$\Delta\Phi = 3.79\times10^{-4}E^{1/2}\ eV$$

where E is expressed in volts per centimeter. [33]

3.3 Thermionic emission for semiconductor

Although the basic theory of thermionic emission has been developed for conductors, it is also suitable for semiconductors only with some additional conditions. While the energy levels in the conduction band in a conductor are considered as completely degenerate, it is not usually the case for semiconductors. The Fermi level shifts toward the middle of bandgap while thermally exciting the charge carriers. Secondly, although the number of charge carriers is enough for immediate screening for a conductor at the surface while applying external electric field, it is more complicated for semiconductor. The applied field may penetrate the bulk depending on the charger carrier concentration of the material. The effect of this penetration is to bend energy bands near the surface, giving rise to a contribution to the Schottky lowering of the image force barrier. The presence of discrete charges in the impurity states and in surface state of a semiconductor also ensure that the surface properties are different from those of the bulk. The resultant charges can introduce charge imbalance and produce a space-charge layer that will depend on the external field. Due to the existence of space-charge layer, the emission will no longer follow Richardson-Dushman's equation.

3.4 Temperature dependency for semiconductor work function

The work function Φ is defined as the energy difference between the Fermi level and the vacuum level at absolute zero. [36] For extrinsic semiconductors, the carrier concentration turns on when the thermal energy is larger than the energy difference between dopant level and conduction band minimum for N-type and valence band maximum for P-type semiconductors. For intrinsic semiconductors, the equilibrium carrier concentration (n_i) is given by

$$n_i = \sqrt{N_c N_v} \exp\left(-\frac{E_g}{k_B T}\right)$$

N_c, N_v ,the effective density of states at the band edges, are dependent on temperature and the effective mass of electrons and holes, respectively. This effective density of states can be calculated as

$$N_c = 2\left(\frac{2\pi m_e^* k_B T}{h^2}\right)^{\frac{3}{2}}$$

$$N_v = 2\left(\frac{2\pi m_h^* k_B T}{h^2}\right)^{\frac{3}{2}}$$

where m_e^* and m_h^* are the effective masses for the electrons and holes, respectively. For semiconductor carrier concentration (n for electrons and p for holes), they can be expressed as

$$n = N_c exp\left(-\frac{E_c - E_F}{k_B T}\right)$$

$$p = N_v exp\left(-\frac{E_F - E_v}{k_B T}\right)$$

where E_c and E_v are the conduction band edge and valence band edge, respectively. In an intrinsic semiconductor, n = p and the Fermi energy for the intrinsic semiconductor E_{Fi} can be found from rearranging the above equations:

$$E_{Fi} = E_v + \frac{1}{2}E_g - \frac{1}{2}k_B T ln\left(\frac{N_c}{N_v}\right) = E_v + \frac{1}{2}E_g - \frac{3}{4}k_B T ln\left(\frac{m_e{}^*}{m_h{}^*}\right)$$

In most materials, if the effective mass of both charge carriers is close enough, the intrinsic Fermi energy, E_{Fi}, can be assumed to be at the middle of bandgap. In this case, the temperature dependence is not significant because the last term in the above equation is essentially zero. In the other cases, the intrinsic Fermi energy will be somewhere between E_v and E_c, and it will be a function of temperature, the effective density of state of both bands and the effective mass of charge carriers.

With that said, linearity of Richardson plot may be achieved for semiconductor surfaces. However, the interpretation of the result could be more complicated. It can be due to fortuitous mutual cancellation of the effects of large temperature variation of the work function and of the reflection coefficient. [37]

Chapter 4 Experimental Procedures & Development of Experimental Apparatus

Profound efforts have been made toward developing a unique experimental apparatus customized for the unique materials challenge. For one, a class of novel materials that claim to be electrode materials needs to be verified. A high temperature electrical conductivity measurement had been performed in the 1950s to 1980s [38], ; however, there is not a commercially available instrument on the market with the desired flexibility. On the other hand, materials may undergo transformation at its proposed working temperature. Conventional surface science instruments do not have the capability to observe the surface's chemical state at its working temperature, which is over 1000 ^{o}C. Work function measurements utilize thermionic emission characteristics along with in-situ Auger Electron Spectroscopy (AES) which complement one another for this task. In this chapter, the development of these aforementioned techniques are described in detail.

4.1 Polymer-derived silicon carbide, polymer-infiltration-pyrolysis and hot-pressed

All sample preparation is done by our collaborators, Dr. Bordia and his group in Clemson University. The synthetic route will be briefly described for the reader's information. As mentioned in Chapter 2, the polymer-derived ceramics (PDCs) technique was employed to fabricate pre-ceramic polymer and further SiC/C monolith; a diagram of the specific PDCs process devised in this work is shown in **Figure 4.1**.

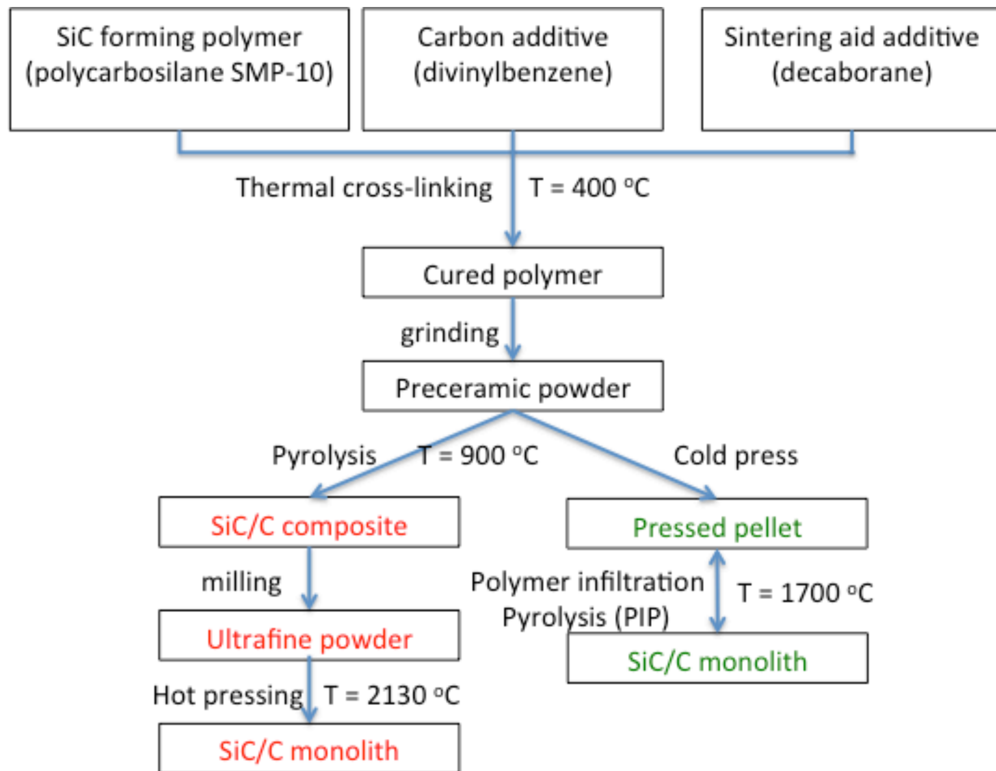

Figure 4.1. A diagram of the PDCs procedure for fabricating SiC/C.

The first step of the PDCs process is thermal cross-linking. The appropriate amount, based on the desired weight %, of the decaborane and divinylbenzene are mixed with the SMP-10 polymer in the inert glovebox, typically using a 20 mL scintillation vial as a container. Currently, we varied the amount of decaborane from 0 wt% to 1 wt% (based on the amount of SMP-10 precursor) and 0 wt% 5 wt% divinylbenzene (based on the amount of SMP-10 precursor). Once all the precursors have been added, the lid of the scintillation vial is closed in the inert glovebox. Electrical tape is placed around the outside of the edge of the cap to further seal the vial. The sealed vial is removed from the glovebox and placed in an ultrasonicator for 2 hours. Solid decaborane should not be observed in the vial after the two hours of sonication. The sonicated precursor mixture is placed in a crucible that can withstand a minimum of 400°C (e.g. quartz, alumina) and is

covered with graphoil. The graphoil ensures that contaminants do not fall in the precursor and also it removes any trace oxygen from the gas. The crucible is placed in the center of the tube in a tube furnace. The gas environment is ultra-high purity argon (Ar UHP 5.0-K, 99.999%) / hydrogen. The tube is purged with ultra-high purity argon with minimum three purges to minimize the residue oxygen contains. The polymer is cross-linked at temperature of 400 ^{o}C under a gas flow of a 2% Hydrogen in Argon gas mixture for various time durations; a typical heating profile for the crosslinking process is from room temperature to 400°C at 5°C/min, holding at 400°C for two hours, and cooling down at 5°C/min to room temperature. Upon crosslinking, the pre-ceramic products are transferred to polypropylene Nalgene vial that will fit in the mechanical mill in the inert gas glovebox. In addition to the polymer, SiC milling media is added. The Nalgene vial is sealed inside the inert glovebox. The cross-linked polymer is then milled in the Spex Mixer/Mill (SPEX SamplePrep LLC) to create the amorphous SiC powders. Once the samples are thoroughly milled, it is placed back into the glovebox and sieved to remove the milling media and any cross-linked SMP-10 that did not get pulverized.

There are two synthetic routes that we have applied in the study, hot press (shown in **Figure 4.1** (left)) and polymer infiltration pyrolysis, PIP, which is shown in **Figure 4.1** (right). Followed by thermal cross-linking is pyrolysis. The purpose of pyrolysis is to convert the preceramic polymer to ceramic. An alumina crucible is lined with graphoil in the inert gas filled glove box, and the milled preceramic powder is transferred to the crucible. The crucible is then covered with graphoil relocated from the glovebox to tube furnace for pyrolysis. The crucible is placed in the center of the tube furnace and the gas environment is identical to the thermal cross-linking step: the tube was purged with ultra-

high purity Ar for a minimum of three times and then flowing Ar with 2% H_2 gas. Using 2% Hydrogen in Argon gas, the sample is heated at 10°C/min to 400°C, held at 400°C for 10 minutes, increased at 5°C/min to 900°C, held for two hours, and cooled at 5°C/min to room temperature.

The third step is milling (attrition milling). Attrition milling shrinks the powder diameter for further shaping and densification. Approximately 75-120 grams of pyrolyzed powder were milled each time. Using 1 part of powder with 8-10 parts of 5 mm diameter SiC milling media, and SiC attritor arm in a 750 mL Teflon lined vessel, the samples were milled for 2 hours at 400 rpm in the presence of 200 mL of hexane. The powders were then removed and placed in a 1000 mL round bottom flask and placed in a rotary evaporator (Heidolph Instruments GmbH). After much of the hexane was removed from the sample, it was then placed in a vacuum oven, heated to 80 °C at a pressure around 200 mbar and left overnight to fully evaporate off the hexane. The sample was then sieved through a 125 μm sieve followed by the 71 μm sieve to remove the milling media and any large particles. This fine powder was then hot-pressed into a monolith.

The hot pressing was conducted in a FCT HP W 150/200-2200-100-LA at the University of Vienna. The pyrolyzed powders were hot-pressed with a round graphite die with 15 mm diameter. The die was coated with a thin layer of h-BN, and the powder was wrapped with graphite foils to avoid direct contact with the die. The pellet was pre-compacted at 28 MPa. The amount of powder used corresponds to a final height of 5 mm, assuming complete densification. After closing off the chamber, it was purged with ultra-high purity argon twice. The process was conducted at a slight Ar overpressure (pa = 1050 mbar), with a very small rate of flowing Argon. The heating and loading profiles

are shown in **Table 2**. The maximum temperature is 2130 ^{o}C for 60 minutes; the loading is 5.0 ~ 5.4 kN throughout the process. Afterwards, the samples were carefully removed from the die body and the remaining graphite on the sample surface was ground off using diamond-grinding media. The density (ρ) of the densified pellets was obtained from the Archimedes technique, and the percentages of the theoretical density (i.e., the relative density, ρ_{rel}) at each composition were calculated using lattice parameters extracted from the X-ray diffraction (XRD) patterns.

Table 2 The temperature ramping and pressing load profile for the hot-press.

Temp. at start of segment / °C	Temp. at end of segment / °C	Ramp / K min^{-1}	Holding time / min	Load / kN (MPa)
20	650	~ 15	-	5.0 (28)
650	1700	10	-	5.0 (28)
1700	1850	6	-	5.0 (28)
1850	1850	-	5	→ 5.4 (30.6)
1850	2130	10	-	5.4 (30.6)
	2130	**-**	**60**	**5.4 (30.6)**
2130	2130	-	5	→ 5.0 (28)
2130	1550	5	-	5.0 (28)
1550	600	10	-	5.0 (28)
600	20	~ 5	-	5.0 (28)

In an effort to develop a conformal and low temperature process to utilize the advantages of polymer-derived synthesis, a route that enables better control of the nanostructure was investigated. This process involves repeated infiltration and thermal cross-linking, and thus is called polymer-infiltration pyrolysis (PIP) synthesis.

As shown in **Figure 4.1**, PIP route shares the same steps, including thermal cross-linking and milling to get preceramic powder. The preceramic powder can be then shaped using many different methods, such as casting, injection molding, pressing, tape casting, fiber drawing coating and impregnation. [24] For a demonstration, we chose to press the powder into pellets. 0.8 g of the polymer powder was cold pressed under vacuum at 150 MPa pressure using a 25 mm die set. As shown in **Figure 4.2** (a), the vacuum die set

under uniaxial loading applied by an electric hydraulic press. The cold-pressed polymer pellets with a thickness of ~ 2 mm are then pyrolyzed in flowing Ar atmosphere in order to obtain the SiC ceramics with the heating profile as 2°C/min to 275°C with 1 h dwell time; 1°C/min to 400°C with 2 h dwell time; 1°C/min to 700°C; 2°C/min to 1100°C with 1 h dwell time). The pellets before and after the pyrolysis are shown in **Figure 4.2** (b) and (c). A linear shrinkage of ~ 30 % and a mass loss of ~ 20 % due to the polymer-to-ceramic phase transformation were measured for the first pyrolysis. The density of the pyrolyzed ceramics is ~2.85 g/cm^3 (relative density 60-63%). A post-annealing was performed at 1700 ^oC to get rid of minor residual oxygen and to further crystallize.

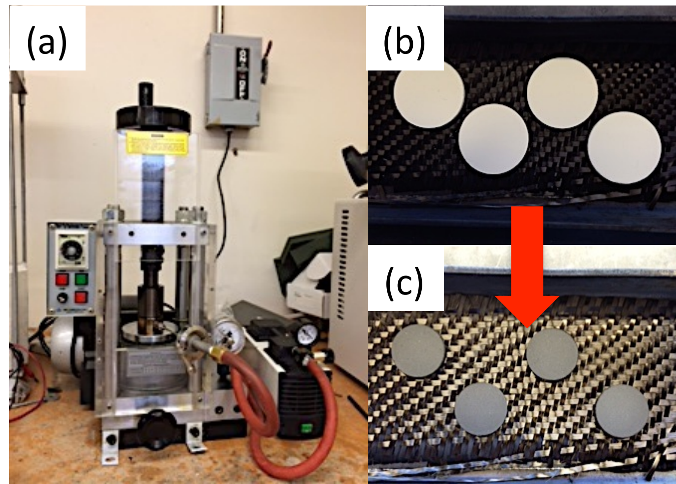

Figure 4.2. (a)*: Vacuum die set under uniaxial loading applied by an electric hydraulic press*; (b) pressed preceramic pellets; (c) SiC/C pellets after PIP synthesis

To increase the relative density of the post-annealed ceramics, multiple liquid polymer infiltration and pyrolysis (PIP) cycles needs to be done. For an effective polymer infiltration, a glass set up was designed. As shown in **Figure 4.3**, the ceramic samples are placed into a 100 ml glass flask. A 60 ml funnel containing liquid SMP-10 polymer is adjusted on top of the flask in a way such that a valve controls the flow of the liquid polymer from the funnel into the flask. The funnel has a pressure-equalizing arm with a

valve connected to a vacuum pump. Before opening the lower valve the liquid polymer is degassed under vacuum and, concurrently, the flask containing the ceramic samples is evacuated (**Figure 4.3** (a)). By opening the lower valve after 1-2 hr the degassed SMP10 flows down, fills the flask, and infiltrates into the open pores of the ceramic pellets (**Figure 4.3** (b)). The setup is left for 24 hr to ensure a complete infiltration process. Then the samples are removed from the flask and pyrolyzed. After 3 repeats of the PIP cycle the ceramics are annealed at 1700°C. Then the PIP cycle is repeated three more times and after the last cycle the ceramics are post annealed again.

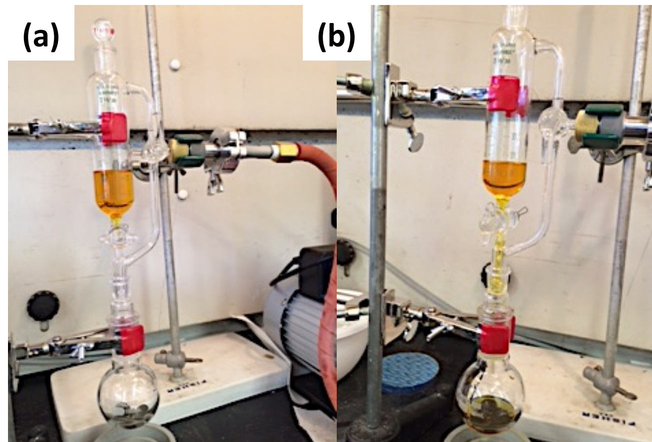

Figure 4.3. Polymer infiltration set up including a flask containing the SiC pellets and a funnel containing liquid SMP10 polymer (a) the set up under vacuum when the lower valve is closed. (b) Lower valve is open and the liquid polymer is flowing down into the flask.

4.2 Customized high temperature electrical resistivity measurement apparatus

In this section, the development and the data acquisition routine are described. Before jumping into detail, a brief literature review will be done first. In the development of high temperature electrical resistivity measurement apparatus, we adopted techniques from our previous project in collaboration with Dr. Ma [39] for making custom Seebeck

coefficient tester and many other people's work. The data acquisition is realized through an in-house developed LabVIEW program.

4.2.1 High temperature electrical conductivity measurement from literature

High temperature electrical conductivity for materials has been reported in the literature for various materials. However, the literature about high temperature electrical conductivity measurement is relatively spotty. Typical measuring apparatus can be summarized in the following. In **Figure 4.4(a)**, Grone et al. [40] have created a standard electrical conductivity measuring apparatus, in which the sample is sandwiched by the two Pt electrodes. The whole apparatus is made of Al_2O_3 and the electrodes are made of Pt; in **Figure 4.4(b)** [41], Zhou and et al. have shown a more detailed design on how the sample holding is realized with perpendicular pushing force from both sides; in **Figure 4.4(c)** [42], Boor and et al. have done similar work with a more sophisticated design where the clamping force comes from the top and bottom.

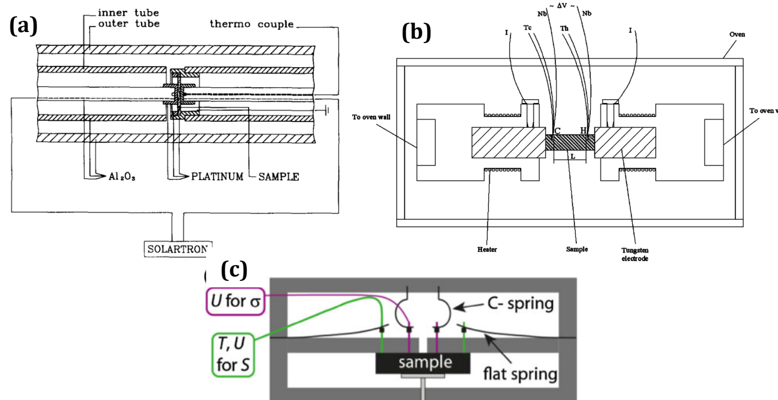

Figure 4.4(a) a typical design utilizing Al_2O_3 and Pt to construct the measuring apparatus; (b) a more detailed design showing the pushing mechanism on two sides of the sample and (c) a different design made use of gravity and vertically fastened the sample and secured the contacts.

We found that people adopt four-point contacts unanimously from the literature review. The four-point contact method will be discussed in the following section. Despite

the physical similarity, we found that the main constraint for the apparatus is on the material selection for the metal contact and for the frame work. Due to the high working temperature, material selections are limited. The refractory metal may be used for an electrical contact, but it oxidizes quickly in the presence of oxygen. The oxide from refractory metal, such as MoO_3, with sublimation temperature at 1155 ^{o}C, can be deposited everywhere. This jeopardizes the measurement above 1155 ^{o}C. Besides the deposition issue, the other issue in the presence of a pushing mechanism is high temperature annealing for the spring. Despite the huge temperature gradient, the cool end of the testing device may remain hot enough to lose its compression strain during a prolonged test. In other words the contact may become loose at high temperature.

In general, there are only two ways to secure the contact between sample and the electrode: 1. The sample having pressure contacts which are either weighted or spring loaded; 2. The specimen with a wrapped wire contact [43]. To meet these requirements, we found the latter option to be a better solution in order to hold the sample tightly through direct wire wrapping. This is design shown in **Figure 4.5** [44]. In this design, the mechanism has the beauty of simplicity but also the easiness to repair. In the actual setup, we only used a high density alumina and Pt at the hot zone, making it easier to swap and repair when compared to other mechanical clamping mechanisms. As shown in **Figure 4.4** and **Figure 4.5**, there are many ways to maintain physical contact for conductivity measurement and it turned out the most reliable mechanism was to utilize wire-wrapping. The next task is to identify the best approach for resistance measurement.

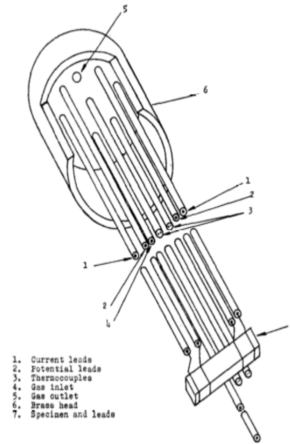

Figure 4.5. Simple wrapping technique to ensure the contact between sample and wires. [44]

Convenient resistance measurements typically consist of two-wire contacts employing Ohms law. For a more accurate measurement, a four-wire setup is usually adopted. As shown in **Figure 4.6 (a)**, while the resistance of the device under test (DUT) is adjacent to the lead, the lead resistance contributes to the measured resistance and is not negligible. Because the test current (I) causes a small but significant voltage drop across the lead resistances, the voltage (V_M) will not be the same as the voltage drop (V_R) across the resistor R. Due to the limitation of two-wire method, a different approach is used for precise resistance measurement. The four-wire (Kelvin) resistance measurement (in **Figure 4.6 (b)**) is used to reduce the effects of test lead resistance. With this configuration, the test current (I, ~1 mA) is forced through the test resistance (R) via one set of test leads (source leads) while the voltage (V_M) across the DUT is measured through a second set of leads (sense leads). Although some small current (typical less than 100 pA) may flow through the sense leads, it is usually negligible and can generally be ignored. Since the sense current is significantly smaller than test current, voltage measured (V_M) essentially equals to voltage drop across DUT (V_R).

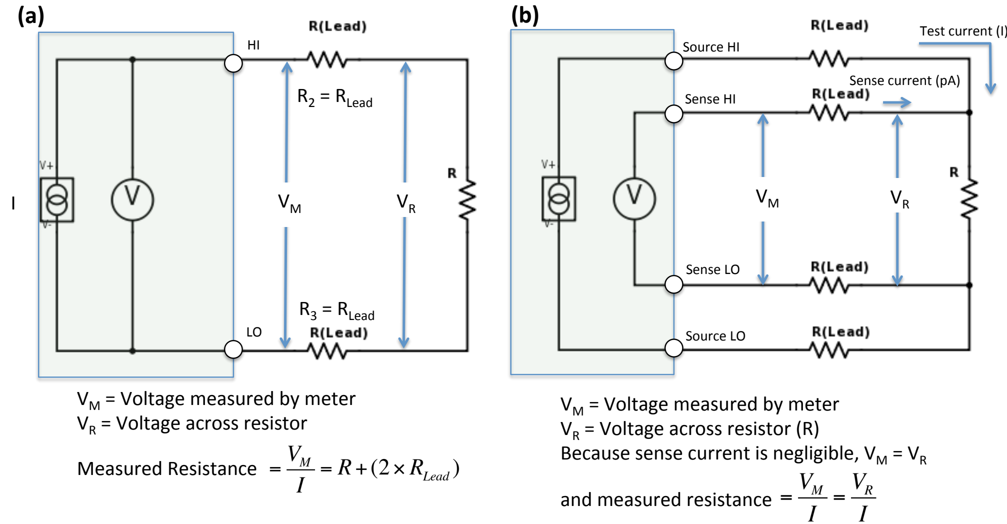

Figure 4.6 (a) Schematic diagram of two-wire resistance measurement; (b) schematic diagram of four-wire resistance measurement.

4.2.2 Electrical conductivity apparatus in the present research

As shown in **Figure 4.7,** adopting design shown in **Figure 4.5**, is our most effective design. In this design, unlike others, simplicity is the main principle to follow. The wires directly wrap onto a bar shape specimen. The second design principle is called "Matryoshka doll". We utilized a 2.5" O.D. tube furnace (Across International TF1700 Tube furnace) and we inserted a 2.0" O.D. alumina tube, attached with quick-disconnect to Kwik-Flange KF (MDC Vacuum Products, LLC). The advantage of this design is to ensure a good control over the test atmosphere, and we are capable of running designated gas during the test. Besides the control over the atmosphere, it is also easy to swap to different tube furnace if there is a need. Lastly, the tube in tube design gives us better control over the cleanliness of the tube, preventing undesired deposition and environmental contamination.

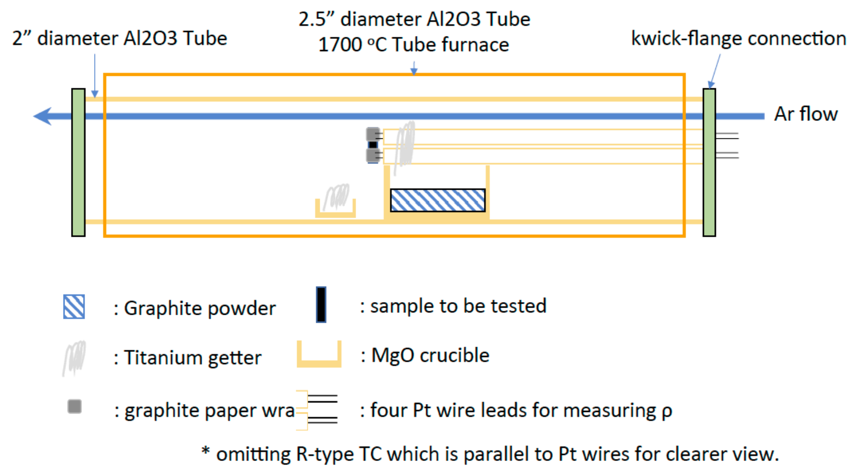

Figure 4.7. Modified “Matryoshka” design for the electrical conductivity measuring apparatus with the sample installed by the wrapping mechanism.

Three double-bore alumina ceramic tubes (0.188” O.D. and 0.063” I.D., McMaster-Carr) were bounded with an alumina based ceramic paste (Ceramabond 503, Aremco products, Inc.). Two bores provide channels for the thermocouple, the other four channels leave the possibility for high accuracy with a four-point measurement. The thermocouple chosen here is 0.01inch diameter, uninsulated and fine gauge platinum based thermocouple (Omega Engineering). The length of alumina tube is 1.5 feet, which locates the sample in the middle of the high temperature furnace. The lengthy alumina tubes ensure metal gaskets and viton® elastomer O-ring stay cool during the testing period.

As for sample holding, although the wrapping design circumvents the issue of mechanical contact at elevated temperature, the high temperature causes another issue regarding the platinum silicide alloy (α-Pt_3Si) formation. The eutectic point of such compound can be as low as 830 ^{o}C. [45] The direct contact between Pt wires and SiC samples or any Si containing materials leads to wire breakage above the eutectic temperature. As a preventive action, a piece of graphite paper is used to wrap the SiC

sample, and prevent direct contact between the Pt wire and SiC sample. For reference, the eutectic temperature for Pt and C is around 1705 ^{o}C which is close to the Pt melting temperature.

The introduction of graphite paper successfully prevented the formation of platinum silicide alloy for the Pt wire; however, it also creates another issue. While the graphite paper wrapping solved the problem of the Pt silicide formation, it creates a physical difficulty to put four graphite stripes on the same sample and wrap them with a Pt wire individually. Since the sample resistance is several order magnitudes higher than the resistance of the Pt wires, a small error caused by the wire resistance can be negligible. This measurement technique, called the Kelvin clip, is more appropriate for our case, and makes it much easier to assemble the devices. The Kelvin clips method utilizes a clip to facilitate a probe for current meter and a probe voltage meter on the same point. It is under the assumption that the resistance of the tested specimen is much higher than the connection / wire. In our case, there are at least 2 orders of magnitude difference so the assumption holds valid. Again, this method may be optional depending on the specimens for future applications and we still maintain the capability of measuring different resistance ranges.

4.2.3 Measurement procedure

To fully access the efficacy and optimize the electrical resistivity measurement, two procedures were put together to verify the data taken.

Procedure – 1: The measurements were made intermittently every 20 ^{o}C increment while furnace temperature is increasing to **1500 ^{o}C** from room temperature,

utilizing the quartz tube furnace (Lindberg/Blue MTM Mini-Mite tube furnace, Thermo Scientific). At each temperature, the computer generated eleven different sets of current (+1, -1, +2, -2, +3, -3, +4, -4, +5, -5, and 0 mA), and corresponding voltages were recorded. Using this protocol, five consecutive I-V measurements were made, during which the furnace temperature remains the same within ±3˚C. The resistance was evaluated from a linear regression analysis of each cycle. Five measured resistance values were further analyzed to determine their standard deviation (i.e., error bar) for measurements. Four-wire contact was applied in this procedure.

Procedure – 2: The measurements were made continuously while furnace temperature is increased to **1500 ^{o}C** from room temperature using alumina tube furnace (Across International TF1700 Tube furnace). The same protocol to determine the electrical resistance value was used. Temperature was ramped at 5˚C/min. Psedo-four-wire (Kelvin clamp) arrangement was applied in this procedure.

4.3 Versatile UHV Chamber for Surface Analysis

To study the surface properties, the efforts have been made to construct the UHV chamber (shown in **Figure 4.8**) dedicated for in-situ surface characterizations and modifications. The chamber is pumped with turbo molecular pump, titanium sublimation pump, and ionization pump. The chamber base pressure is at 5.0×10^{-9} Torr when chamber is rest and doing Auger Electron Spectroscopy (AES); the chamber pressure goes up to 1.5×10^{-8} Torr during the acquisition of thermionic emission and high temperature in-situ AES. Thermionic emission and its energy distribution can be recorded

through a modified LEED optics. Lastly, ion gun and inertial-electrostatic confinement (IEC) plasma source help to modify surface and simulate plasma impingement.

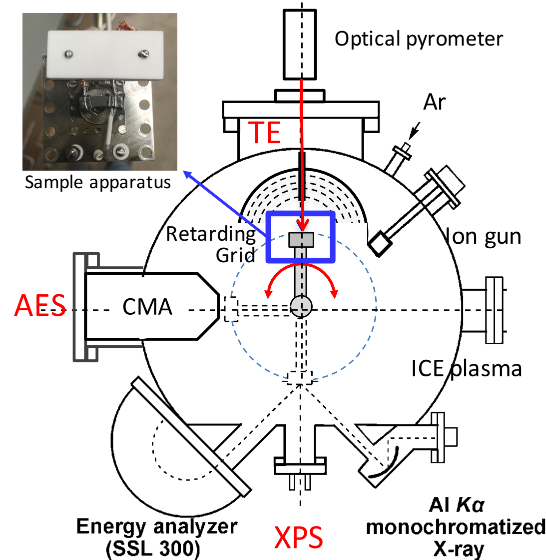

Figure 4.8. The UHV chamber setup has the capability for Auger electron spectroscopy, thermionic emission, ion gun and more.

4.4 In-situ Auger electron spectroscopy

We chose to utilize a double pass cylindrical mirror analyzer (CMA) to acquire AES spectra. CMA is also called coaxial cylindrical analyzer because it basically consists of two coaxial cylinders. The schematic diagram of CMA is shown in **Figure 4.9**. The inner cylinder is grounded and has two gridded apertures suitably positioned along its length. The outer cylinder has a negative voltage, V_a applied to it so that the secondary electrons leaving a suitably located grounded sample and entering the first of the apertures tend to be reflected towards the second aperture. For a fixed cylinder voltage, V_a, there are only electrons with kinetic energy $E_k = eV_e$ can pass through the gridded apertures, where V_a is proportional to V_e. And thus, the AES spectra can be realized. In addition, we took advantage of lock-in amplifier to filter out unwanted noise and to be able to detect the derivative of the electron distribution. The lock-in amplifier is the

instrument that can extract signals with a known carrier wave from a noisy environment. To do so, the lock-in amplifier generates a sinusoidal wave and modulates the signal by applying an oscillating voltage to the outer cylinder. Through Taylor expansion, we know that the first derivative term corresponds to the first harmonic. By neglecting higher order terms, *dN(E)/dE vs. E* can be acquired.

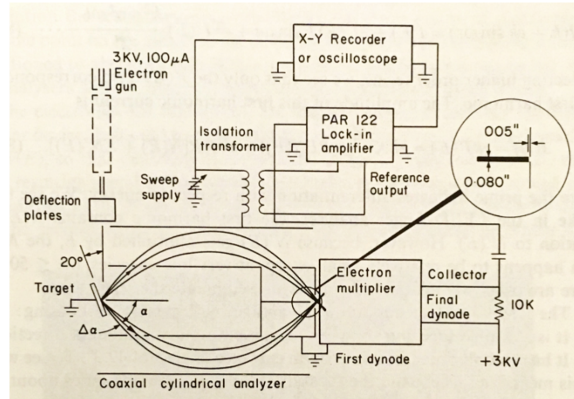

Figure 4.9. The basic cylindrical mirror analyzer (CMA) and block diagram for Auger electron spectroscopy. [46]

Thermionic emission characteristics of the electrode materials play a significant role in determining the mode of current transfer (diffusing versus arcing) near the electrode region in the MHD channels. Current transfer via arcing causes mechanical damages to the electrode, so it is essential to suppress the plasma induced arcing. Technically this can be achieved by enhancing the rate of thermionic emission from the electrode surface; therefore, a key technical aspect is to reduce the surface work function of the materials. Deposition of alkaline metal oxide on surface is widely known for lowering the surface work function and even creating negative electron affinity. [47] [48]

4.5 Thermionic emission and its energy distribution

Thermionic emission is the thermally induced flow of charge carriers from a hot cathode surface. This occurs because the thermal energy given to the carrier overcomes

the work function of the materials. It is common to utilize a current preamplifier to enhance the signal to noise ratio. In this section, two types of thermionic emission will be addressed; direct heating and indirect heating.

The objective in this experiment is not only to collect the emitted electrons but also to analyze the energy. In general, the electron analyzers utilize an electromagnetic field types to deflect electrons and sort them according to their initial kinetic energy. There are a retarding field analyzer (RFA), a cylindrical mirror analyzer (CMA) and a hemispherical sector analyzer (HSA). RFA is the simplest in structure and is often coupled with other techniques. In the presented research, a low energy electron diffraction (LEED) optics was modified to act as an RFA; an electron gun in the center was removed and left a center path for remote temperature probing. This modified LEED optics was installed in the versatile UHV chamber to act as the retarding grid (**Figure 4.8**). The current is collected using the retarded grid and then fed to a low noise current preamplifier (Stanford Research System, SR570); it is capable of measuring current to the picoamp level and communicates through the LabVIEW program. For the temperature measurement, a direct-contact thermocouple is not realistic due to potential metal deposition at the high temperature. Thus, an infrared pyrometer (Chino IR-AH, Chino) is utilized here. This is a single wavelength pyrometer with a detecting window with a wavelength of 0.65 μm. This external pyrometer is reliable from 600 ^{o}C to 3000 ^{o}C, with 1 ^{o}C resolution. It is worth to note that most of the commercially available portable pyrometers use a much longer spectral wavelength and the infrared does not transmit through the glass window. The base pressure is generally at low 10^{-9} Torr and the pressure went up to low 10^{-8} Torr while the sample was heated to around 1000 ^{o}C.

The samples are held on to a XYZR manipulator, which is able to shift and move three dimensionally for optimal emission current. This means the sample can maneuver from the thermionic emission position to Auger spectrum position without venting the chamber. All the in-situ work relies on this flexibility.

To achieve direct heating and indirect heating for sample in a vacuum chamber, it depends on the assembly of sample holding apparatus. During assembly, a piece of stainless-steel plate (EV parts, Kimball Physics) was fixed on the manipulator as "platform". As shown in **Figure 4.10(a)** and **(b)**, the heater wires were sandwiched with alumina plates, and the plates were held with nuts and screws and isolated with ceramic eV parts (Kimball physics). A piece of silicon carbide is held using the previously described graphite paper wrapping mechanism. In the case of indirect heating, as shown in **Figure 4.10(c)** and **(d)**, another stainless-steel plate is installed in front of the first piece with smallest gap possible for the highest heat transfer efficiency. The sample is cut into a disk shape with 1.5 mm thickness and held by the spark welded Tantalum ribbon. At the bottom of plate, a bare copper wire is attached for applying bias to the sample.

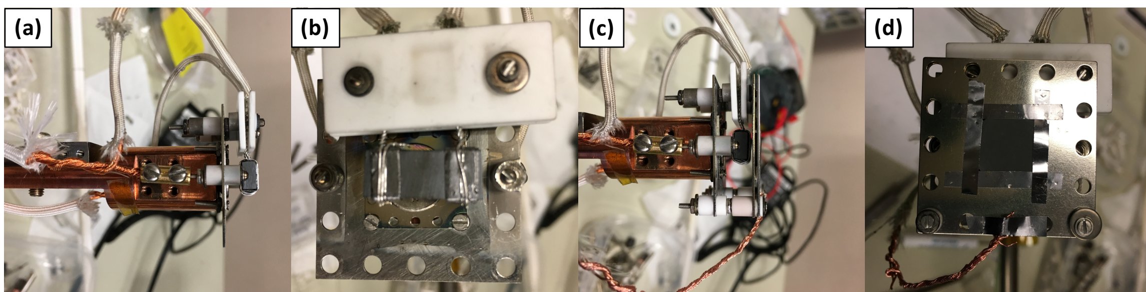

Figure 4.10 Sample holding apparatus: (a) and (b) direct heating, sample is held with Pt wire and graphite wrap as previously described, heating wires are sandwiched with alumina plate; (c) and (d) indirect heating, sample is held on a stainless-steel plate (Kimball physics) with spark welded Tantalum ribbon. Plates are isolated using ceramic eV parts (Kimball physics).

The cleanness of specimen surface is key to acquire reliable data and hence in situ treatments and modifications were carried out in situ in the chamber. Specifically, an Ar

ion gun is installed for sputtering the surface is installed. Argon ion bombardment is for general-purpose surface cleaning because there are always organic carbon contaminants from the atmosphere. The Argon ion gun ionizes and accelerates argon ions and bombards off the surface contaminants.

4.5.1 Direct heating and in-direct heating

Specimens of interest can be firmly held with previously discussed graphite paper wrapping method. The graphite paper ensured good electrical contact and prevented the alloy formation due to thermal migration. Simplicity is the advantage of direct heating method. However, under some circumstances, the direct heating method is not feasible. For example, there is no way to distinguish emission currents between currents from sample and currents from background and also the voltage drop across the sample can broaden energy distribution curves. Another detrimental disadvantage occurs when the electrical resistance is low, and sample cannot be heated to desired temperature range.

A heating element can be placed behind the sample. The advantage of in-direct heating is that both the heating element and the sample can be biased independently. The issue of insufficient heating using the direct heating method can be resolved. However, there are new issues that need to be addressed with in-direct heating.

Ideally, the emission from sample can be distinguished from background emission. The disadvantage of this method is caused by the nature of indirect heating. In order to heat up the sample to emit electrons, enormous amounts of heat have to be dumped into the chamber. There is a 200 ~ 300 ^{o}C temperature difference between heating element

and sample. Experimentally, the thermally promoted outgassing is a critical factor to acquire thermionic emission that needs to be addressed.

4.5.2 Thermionic emission energy distribution

Lastly, with the above mentioned in-direct heating arrangement, heating element and sample can be biased separately. On one hand, the heating element can be positively biased, and all the electrons will be drained to ground and the emission from the heating element will be suppressed regardless the high temperature. On the other hand, the sample can be biased negatively and this additional energy will drive the emission electrons to the collector even if the work function of the sample is smaller than that of the detector.

4.6 Specimen characterization

The microscale morphology of the samples from both hot pressed and polymer infiltration pyrolysis was examined via transmission electron microscopy (TEM, Tecnai G2 F20, FEI) with an acceleration voltage of 200 kV and scanning electron microscopy (SEM, JEOL JSM-6010) with acceleration voltage 5 – 15 kV. The crystal structure was verified by XRD patterns obtained with a Bruker D8 Discover instrument (Cu K_α radiation, λ = 1.5418 Å). A PHI 5000 VersaProbe X-Ray photoelectron spectroscopy (XPS) system (Al Kα radiation, hν = 1486.6 eV) was employed for surface elemental analysis. Unless otherwise indicated, the specimens were fractured prior to the photoemission spectroscopy measurement to obtain information characteristic of the bulk specimen and not the oxidized surface. Raman scattering spectrum was acquired by a Renishaw inVia system with laser source at 514 nm and 785 nm, which is equipped with

the Leica DMIRBE inverted optical microscope. Glow Discharge Optical Emission Spectrometry (GDOES) was measured by Horiba GD-Profiler-2.

Chapter 5 Structural, morphology and elemental information of polymer derived silicon carbide

As a new fabrication process for materials is developed, a thorough characterization is crucial to understand how the process affects the material's properties. In this chapter, polymer-derived silicon carbide fabricated through hot-pressed (HP) and polymer-infiltration-pyrolysis (PIP) were examined. Structural, morphological, and elemental data were obtained and analyzed. X-Ray diffraction (XRD) was used for structure analysis; scanning electron microscopy (SEM) were used for morphologic analysis; X-Ray photoelectron spectroscopy (XPS) and glow discharge optical emission spectroscopy (GDOES) were used for elemental analysis; ^{29}Si NMR provided the bulk silicon chemical state; Raman spectra provided further information on carbon species.

5.1 Structure analysis –

5.1.1 X-Ray diffraction (XDR)

To optimize processing parameters and confirm the efficacy of the devised PDCs technique, structural and morphological data were first obtained. In this section, the focus is on the structural characterization for specimens fabricated via both hot-pressed and polymer-infiltration-pyrolysis (PIP) utilizing polymer-derived powders. First, we analyzed specimens fabricated through PIP process. Despite the previously claimed advantage for simple additive method to alter composition [49], the boron additive increases the viscosity of polymer, and the resulting polymer is too viscous for the infiltration process. As such, PIP samples were synthesized with zero weight percent

boron additive and various weight percent carbon additives. **Figure 5.1**, shows the XRD patterns acquired from multiple batches of PIP pellets, stacked with the most likely diffraction pattern, silicon carbide polytype 3C structure [50]. The diffraction peaks perfectly matched with the pattern for silicon carbide 3C, regardless how much carbon additive was added.

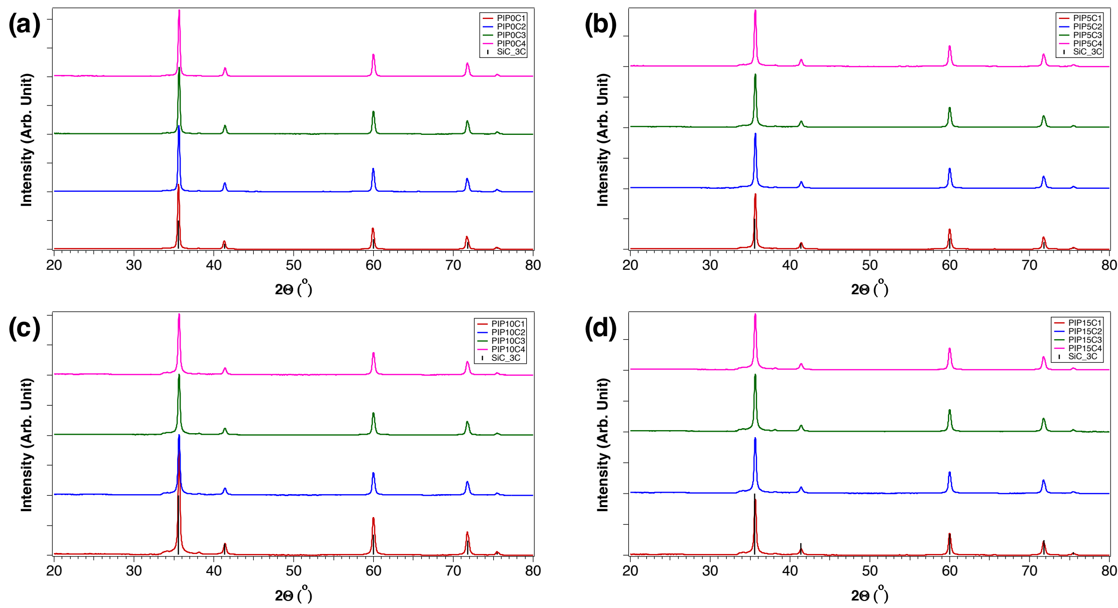

Figure 5.1 XRD patterns of PIP specimens, (a) zero percent boron additive and zero percent carbon additive (denoted as 0C); (b) zero percent boron additive and five percent carbon additive (denoted as 5C); (c) zero percent boron additive and ten percent carbon additive (denoted as 10C); (d) zero percent boron additive and fifteen percent carbon additive (denoted as 15C).

This result for XRD patterns is an indication that the process of making is stable and consistent. Specimens from different batches consisted of the same crystal structure. To take a closer look, the diffraction patterns were averaged for each composition and all resulting patterns for four compositions were stacked (**Figure 5.2**). There is no observable difference between patterns from different compositions. Almost all the diffraction peaks can be attributed to silicon carbide polytype 3C except for one peak at

2θ equals 38, which may be attributed to other silicon carbide polytypes, such as (1 0 3) for silicon carbide polytype 6H.

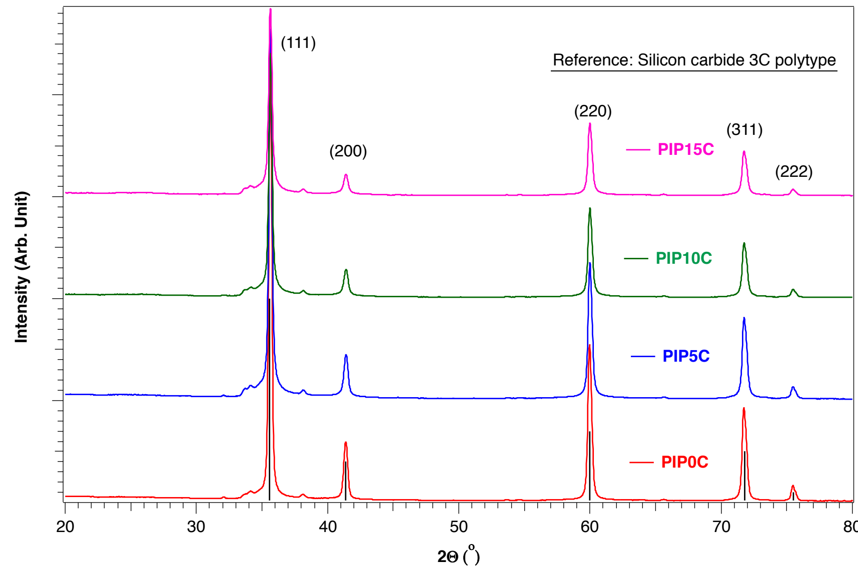

Figure 5.2 XRD patterns of silicon carbide from PIP process with zero weight percent carbon additive (PIP0C, red), five weight percent carbon additive (PIP5C, blue), ten weight percent carbon additive (PIP10C, green) and fifteen weight percent carbon additive (PIP15C, purple). The silicon carbide 3C polytype reference is marked as black stick.

Ideally, through multiple infiltration and pyrolysis cycles, one can gradually fill the void and densify the specimens, and thus complete densification can be achieved through infinite cycles. As a proof of concept for demonstration, ten cycles have been implemented. As shown in **Table 3**, the calculated relative density were ranged from 72.27% to 67.72% under the assumption that the extra carbon added would be completely transferred into the excess carbon in the resulting specimens. This calculation also assumed graphite density is 2.09 g/cm^3 and silicon carbide density 3.21 g/cm^3, and the theoretical density of such composition is the linear combination of the two components. The assumption regarding composition needs verification and will be addressed later this chapter.

Table 3 The average density measurement of the PIP specimens. Assuming graphite density 2.09 g/cm^3 and silicon carbide density 3.21 g/cm^3.

acronym	carbon (wt%)	Boron (wt%)	Bulk Density (g/cm3)	Theoretical Density* (g/cm3)	Relative Density
PIP0C	0	0	2.32	3.21	72.27%
PIP5C	5	0	2.165	3.154	68.64%
PIP10C	10	0	2.165	3.098	69.88%
PIP15C	15	0	2.06	3.042	67.72%

Boron additive is not applicable in the current stage because of the viscosity issue. The lack of boron additive weakens the densification process and thus, the resulting specimens are relatively porous. As the process developed, we understood the limitations of the PIP process. Boron additive is crucial for densifying the resulting pellets. On the other hand, specimens fabricated through hot-pressed process can proceed with the presence of the boron additive. Secondly, the process temperature was higher than the PIP process. Thus, the density of the hot-pressed (HP) specimens was expected to be higher.

In terms of structure, there is also significant difference between the two processes. As shown in **Figure 5.3**, X-Ray diffraction patterns for HP specimens were taken. All the specimens were consistent with one weight percent boron additive and various (0, 1, 3, or 5) weight percent carbon additive. Despite the difference in carbon additive, the XRD patterns show unanimously silicon carbide 6H [51] pattern with one extra peak. After analysis, this peak, at 2θ equals to 25.5, may likely be graphite. The relative density of HP specimens, however, is above 97% for all specimens under the same assumption. This variation in density between processes may be attributed to high temperature (2130 ^{o}C) and pressurized sintering.

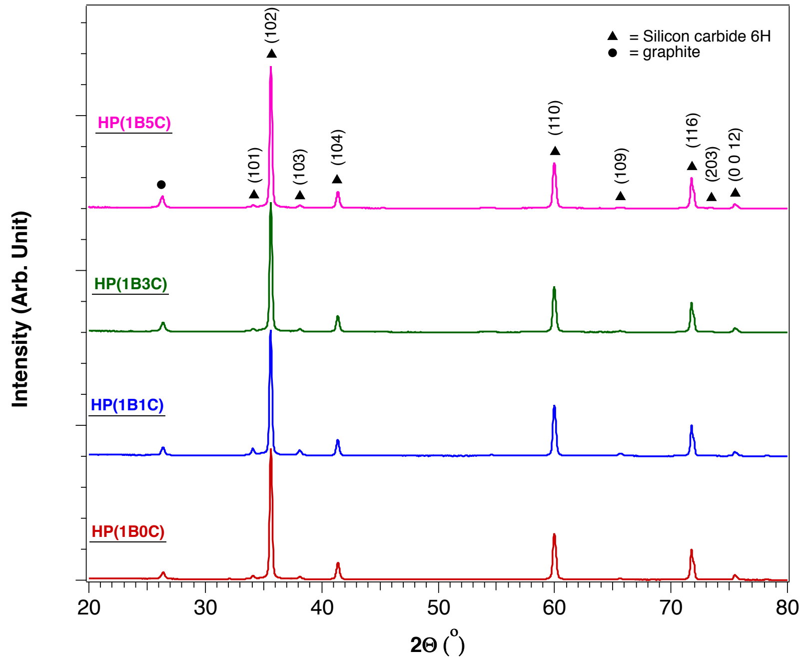

Figure 5.3 XRD patterns of silicon carbide from HP process with zero weight percent carbon additive (HP(1B0C), red), one weight percent carbon additive (HP(1B1C), blue), three weight percent carbon additive (HP(1B3C), green) and five weight percent carbon additive (HP(1B5C), purple). The silicon carbide 6H polytype reference is marked as black triangle and the graphite reference is marked as black solid circle.

Table 4 The average density measurement of the HP specimens. Assuming graphite density 2.09 g/cm^3 and silicon carbide density 3.21 g/cm^3.

acronym	carbon (wt%)	Boron (wt%)	Bulk Density (g/cm3)	Theoretical Density (g/cm3)	Relative Density
HP1B0C	0	1	3.13075	3.21	97.53%
HP1B1C	1	1	3.1318	3.1988	97.91%
HP1B3C	3	1	3.11925	3.1764	98.20%
HP1B5C	5	1	3.10075	3.154	98.31%

To summarize the structure analysis, the PIP process yields silicon carbide polytype 3C and the HP process yields silicon carbide polytype 6H. Another important fact is that the relative density of PIP specimens can only reach ~70% whereas the relative density of HP specimens can reach above 90%. Lastly, the amount of excess

carbon in PIP samples was found to be much higher, there is no crystallized carbon constituent found in XRD patterns acquired from PIP specimens.

5.1.2 Elemental analysis – X-ray photoemission spectroscopy (XPS) for hot-pressed samples

XPS probes the surface properties utilizing the electron spectrum from photo-emitted core electrons. The probing distance of this technique depends on the kinetic energy of the energy and the escape depth. For carbon 1*s* photoemission electrons, the mean-free-path is about 2.5 to 3 nm. [52] In order to examine the carbon species, C 1*s*, O 1*s* and Si 2*p* XPS spectra were acquired from the fractured specimen surfaces with different amounts of boron and carbon doping; the results are shown in **Figure 5.4**. These spectra were taken from the fractured surface to reveal the intragranular chemical species. Since the specimens were not sufficiently electrically conductive at room temperature, the peak positions might be affected with different magnitude of charging. The spectra were purposely not shifted and aligned for better interpretation. Upon examining the C 1*s* spectra, there are at least two peaks, one with binding energy ~ 283 eV and the other with binding energy 284.5 ~ 285 eV. The lower binding energy peak of C 1*s* dominates in the spectra and can be attributed to carbidic carbon, whereas the higher binding energy peak can be attributed to graphitic carbon. [53] Oxygen is observed in every case because of surface oxidation by residual oxygen. Si 2*p* emission peaks show broadening and are asymmetric with binding energy equals to 100.5 eV; this echoes the phenomenon of oxidation and the forming higher binding energy species.

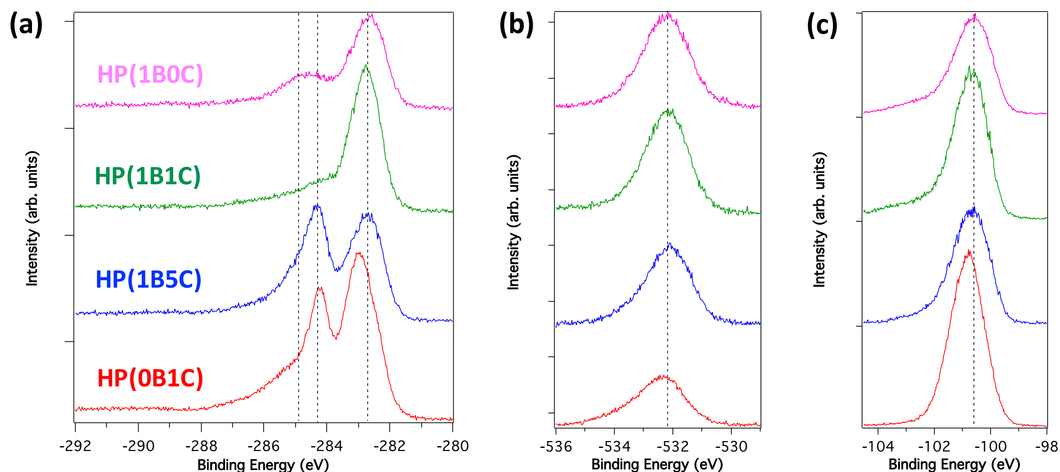

Figure 5.4. (a) C 1*s*, (b) O 1*s*, and (c) Si 2*p* XPS spectra for hot-pressed SiC/C specimen fractured surface with different amounts of carbon and boron dopant

As shown in **Figure 5.4 (a)**, there are clearly two patterns, for specimens **HP(1B5C)** and **HP(0B1C)**, the area of carbidic peak (282.5 eV) and graphitic peak (>284 eV) [53] are roughly 1:1 ratio; for specimens D and E, there is only one dominated peak with a higher binding energy shoulder for each spectrum. This distinct difference leads to drastic difference on electrical properties, which will be detailed in the following section.

Although maximum efforts have been made to acquire XPS spectra from a pristine specimen surface, there is still a significant oxygen peak. It is important to know if oxidation is merely a surface phenomenon or if the silicon oxy-carbide is the product of the process. Since there is no way to distinguish the source of oxygen, XPS may not be an ideal tool for oxygen analysis. An optical spectral analysis that can reveal the relative chemical compositions on a larger scale will be described for both HP and PIP specimens in the next section.

5.1.3 Elemental analysis – GDOES

Glow discharge optical emission spectrometer (GDOES, GD-Profiler-2, Horiba) measures the optical emission induced by Argon ion bombardment. From the emission intensities, relative elemental compositions of the surface, in particular the C:Si ratio, were quantified. [54] Ar sputtering can also provide depth profiling of the compositions. As addressed in the previous XRD section, the specimens fabricated through polymer infiltration and pyrolysis (PIP) are mostly 3C polytype; the specimens processed through hot-pressed (HP) are mostly 6H poly-type. The absolute emission intensity of each element may be affected for multiple reasons, such as Ar pressure and sputtering efficiency. For consistency, all specimens were examined at the same time and pretreated in the same way. Prior to the measurements, all the samples were ultrasonicated in acetone and isopropyl alcohol to remove organic contaminants (mostly grease), and the samples were further baked in air at 200 ^{o}C for 4 hours to remove adsorbed moisture and solvent.

A silicon carbide with 3C poly-type (Albany, NETL) fabricated with chemical vapor deposition (CVD) is used as a reference for its accurate stoichiometry which is C:Si = 1:1. Upon measuring the emission from CVD SiC, we could determine the sensitivity factors for Si and C, assuming that the stoichiometry of CVD silicon carbide is 1:1. This sensitivity factor was applied to evaluate C/Si atomic ratios for all PIP specimens. In **Figure 5.5**, the GDOES spectra taken from PIP specimens, **PIP0C**, **PIP5C**, **PIP10C** and **PIP15C** are shown. Samples showed high amount of H and O near the surface, but those species were retained even in the bulk, implying that moisture penetrated throughout the sample due to low bulk density (67.7% to 72.2%). Despite the

presence of hydrogen and oxygen, we can extract the silicon and carbon intensity, and convert it to C to Si atomic ratio using the scaling factor acquired from SiC(CVD). In **Figure 5.6**, the elemental depth profiles for PIP specimens are shown. The depth profiles were converted from the depth of resulting craters and assuming homogeneous sputtering. From the GDOES analysis, the amount of excess carbon was 20% to 60% instead of 0 wt% to 15 wt% as originally designed.

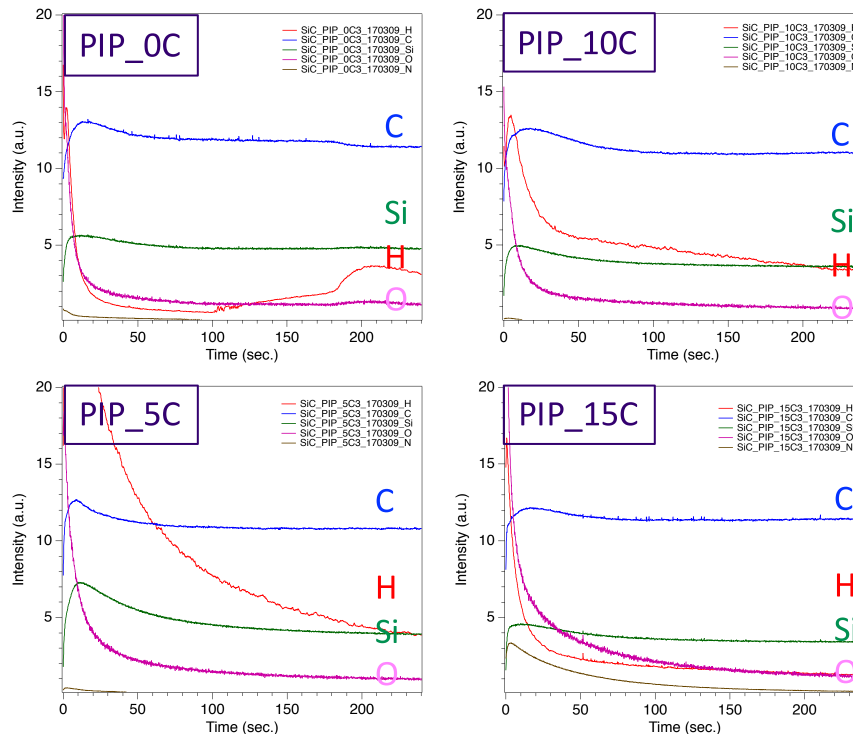

Figure 5.5 GDOES spectra for silicon carbide fabricated through polymer infiltration and pyrolysis procedure.

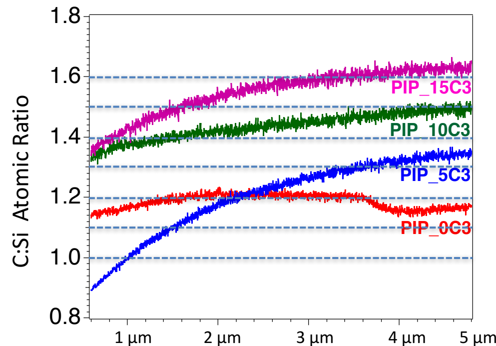

Figure 5.6 Carbon to silicon atomic ratio versus sputtering depth for silicon carbide specimens fabricated through polymer infiltration and pyrolysis (PIP) procedure.

There are several possible reasons that can lead to the above results. In the present study, it could be explained with differential sputtering that leads to abnormally high intensity of certain species. In theory, GDOES utilizes RF derived Ar sputtering to vaporize the sample, so preferential sputtering of C between SiC and graphite is possible. Using the CVD SiC specimen as pure silicon carbide and commercially available graphite as the two extreme cases, we found CVD SiC left ~ 5 μm depth crater and graphite left ~ 40 μm depth crater with the same amount energy of Ar sputtering for 300 secs. For reference, all the PIP specimens left 10 um depth crater after the same amount of energy Ar sputtering for 300 secs.

Acknowledging the disadvantage of the PIP procedure, the specimens fabricated through hot-pressed process were also examined using GDOES. The hot-press procedure shares the same steps with the PIP procedure up to the cross-linking step. For PIP, the cross-linked powders were pressed into a pellet for further infiltration and pyrolysis; for hot-pressed (HP) procedure, the cross-linked powders were pyrolyzed, resulting in amorphous SiC powders. The amorphous SiC powders were hot-pressed into high density pellets.

The samples were pretreated with the same method as PIP specimens before taking measurements. The GDOES spectra was taken from four HP specimens, **HP:1B0C**, **HP:1B1C**, **HP:1B3C** and **HP:1B5C** and are shown in **Figure 5.7.** The absolute intensity of carbon emission is around 8 for HP specimens and 12.5 for PIP specimens with the same intensity of Ar sputtering. The carbon and silicon intensity ratios were similarly evaluated using the sensitivity factors acquired from the SiC(CVD) reference sample. In general, the C:Si ratios for the HP samples are much less than those

found in the PIP samples. One thing worth noting is the intensity of hydrogen and oxygen acquired from HP specimens is consistently lower than those from the PIP specimens. This is likely due to the densely packed nature of the sample preventing moisture from entering.

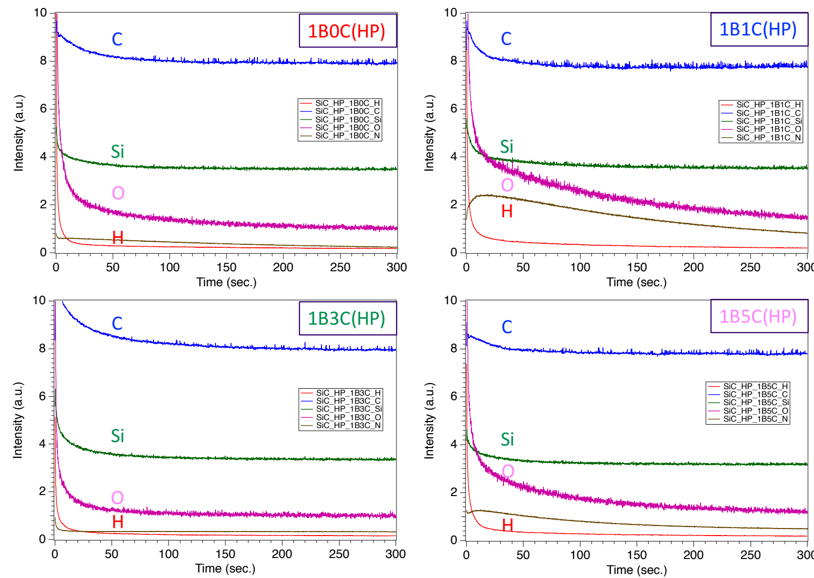

Figure 5.7 GDOES spectra for silicon carbide fabricated through hot-press procedure for HP:1B0C, HP:1B1C, HP:1B3C and HP:1B5C.

Using previously mentioned procedure, the carbon to silicon ration depth profile for hot-pressed specimens can be evaluated. As shown in **Figure 5.8**, the C / Si ratio for **HP:1B0C**, **HP:1B1C, HP:1B3C and HP:1B5C** are 1.075, 1.1, 1.15 and 1.2 respectively. For the reference, all the hot-pressed specimens left ~5 um depth crater after the same amount of energy Ar sputtering for 300 secs.

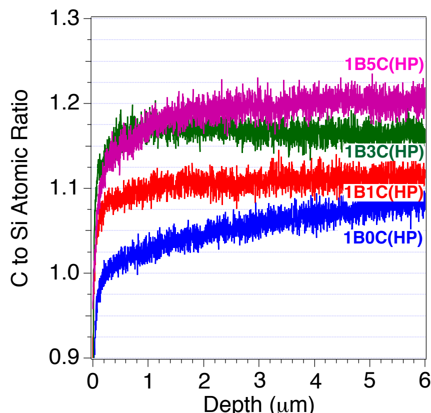

Figure 5.8 Carbon to silicon atomic ratio versus sputtering depth for silicon carbide specimens fabricated through hot-pressed (HP) procedure

From **Figure 5.6** and **Figure 5.8**, the accumulated carbon to silicon ratio can be determined. There is intrinsic excess carbon even without doping. Taking the average of C to Si ratio from 3 to 5 μm, the nominal excess carbon versus GDOES measured C to Si ratio is summarized in **Figure 5.9**. In the silicon carbide forming agent, AHPCS, there is 95% carbon to silicon 1:1 and 5% consisted with two allyl group for polymerization. In the ideal case, the divinyl group should be decomposed and form propene gas. Due to incomplete decomposition, the measured excess carbon is 7.6% for a pristine HP specimen and 16.7% for a PIP specimen. The difference may be attributed to the fabrication processes and it will be addressed in the Raman section.

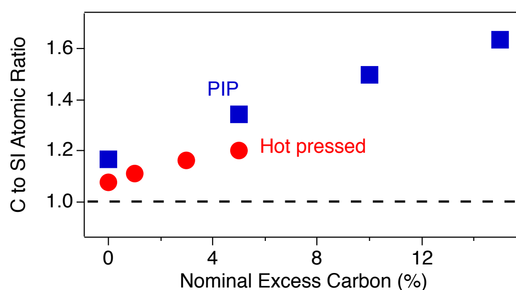

Figure 5.9 Carbon to silicon ratio measured from GDOES plotted against nominal excess carbon from the weight percent of divinyl benzene, carbon additive for PIP and HP specimens.

To summarize the GDOES analysis, there are two major findings. First, the elemental analysis exhibits a similar trend from the polymer additive; however, there is

always much more excess carbon found in the system. Detailed number are collected in **Table 5**. Secondly, by measuring the depth of craters after Ar sputtering, the hot-pressed (HP) specimens exhibited the same erosion resistance as the 100 % dense CVD specimen, which was 1/8 of the erosion of the graphite sample; the polymer-derived-pyrolysis (PIP) specimens showed two times faster erosion when compared to the CVD specimens and a quarter when compared to graphite sample.

Table 5 Summarized nominal excess carbon, total excess carbon and measured excess carbon for hot-pressed (HP) silicon carbide and polymer-infiltration-pyrolysis (PIP) silicon carbide.

Hot-pressed (HP)		
Nominal Excess C (%)	Total Excess C (%)	Measured Excess C (%)
0	30	7.6
1	31	11.3
3	33	16.4
5	35	20.2
Polymer-infiltration-pyrolysis (PIP)		
Nominal Excess C (%)	Total Excess C (%)	Measured Excess C (%)
0	30	16.7
5	35	34.4
10	41	49.8
15	48	63.6

5.1.4 Elemental analysis - ^{29}Si NMR

As part of the efforts in analyzing chemical composition, solid state ^{29}Si Nuclear Magnetic Resonance (NMR) spectroscopy can probe the bulk silicon's chemical state. Using some HP specimens as an example, ^{29}Si NMR spectra are measured and shown in **Figure 5.10.** The three major peaks at -14.3, -20.4 and -25.0 ppm are caused by the silicon carbide 6H polytype [55]; the relatively smaller peaks at -12, -16 and -23.9 ppm may be attributed to the silicon carbide 3C polytype [56]. It is worth noting there are no

peaks found outside of shown spectra, which means there is no silicon oxycarbon nor silicon oxide in the bulk.

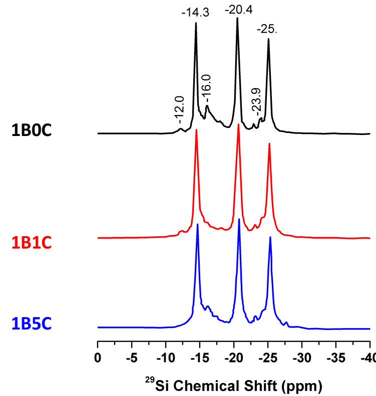

Figure 5.10 ^{29}Si NMR spectra for three HP specimens, 1B0C (black), 1B1C (red), and 1B5C (blue).

5.1.5 Carbon bonding characteristic – Raman Spectroscopy

From GDOES, the carbon to silicon ratio was estimated to exceed unity for nominally Si:C = 1:1 specimens . From the ^{29}Si NMR, all the silicon was attributed to silicon carbide polytype. Knowing the fact that most silicon chemical state is attributed to silicon carbide 3C and 6H polytype, the focus is shifted to carbon chemical state. Raman spectroscopy, as a visible range counterpart to infrared spectroscopy, uses the fact molecules absorb electromagnetic energy characteristic of their structures. It is an ideal tool to learn the local vibration mode of different species. We could use it to differentiate silicon carbide from graphite. In the following section, Raman spectroscopy was applied using the 514 nm (green) laser to probe the bulk properties along with optical microscopy (OM) and scanning electron microscopy (SEM). The Raman spectra of reference are CVD silicon carbide (Albany, NETL) with 3C polytype and commercial graphite and are shown in **Figure 5.11**. For SiC(CVD), the peaks at 797.8 and 970.1 cm^{-1} can be attributed to transverse optic phonon (TO) modes and longitudinal optic (LO) phonon modes,

respectively [57]. For graphite, the peaks at 1583 and 1350 cm^{-1} can be interpreted as G mode and D mode respectively. [58,59]

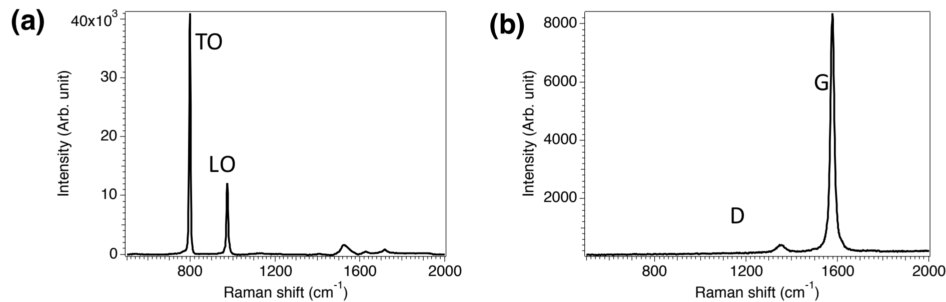

Figure 5.11 (a) Raman spectrum of CVD silicon carbide; (b) Raman spectrum of commercial graphite.

From left to right, the SEM images, OM images and Raman spectra in the 500 – 2000 cm^{-1} region taken from the high contrast (in red) and low contrast (in black) are shown in **Figure 5.12 (a)** to **(d)**, for **PIP0C**, **PIP5C**, **PIP10C** and **PIP15C** (0 wt% - 15 wt% excess carbon polymer additive). From the SEM images, there is not too much of a difference between the compositions at first glance, they all are consistent with small (~1 μm) and big (~10 μm) grains. However, upon close examination, one can identify the larger grains in **PIP15C** as an agglomerate of smaller grains, whereas the bigger grains in **PIP0C**, **PIP5C** and **PIP10C** come with smoother facets.

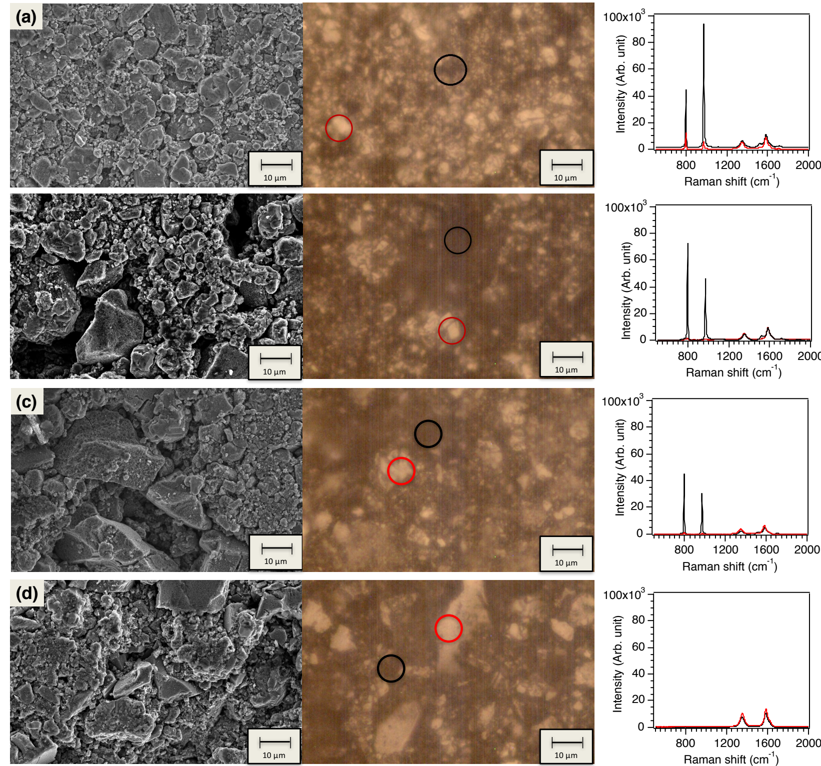

Figure 5.12 SEM images (left), optical microscopy (center) and Raman spectra (right) for (a) PIP0C, (b) PIP5C, (c) PIP10C and (d) PIP15C.

From optical microscopy images, we discovered that there are high contrast domains and low contrast domains for all the specimens we examined. The images from the two methods were properly scaled to the same magnification so it is likely that the high contrast domains could be the larger grains. There is a distinct difference between high contrast domain and low contrast domain for **PIP0C**, **PIP5C** and **PIP10C** but not for **PIP15C**. Since the probing distance for SiC is several orders of magnitude higher than the probing distance for graphite for Raman spectroscopy, this result indicates that graphite is abundant for all compositions and it is not equally spread out for **PIP0C**, **PIP5C** and **PIP10C**; interestingly, for **PIP15C**, the graphite layer is thick enough that it blocked the majority of the SiC signal.

Contrary to specimens fabricated with PIP process, specimens fabricated with the hot-pressed process are relatively dense, with over 95% relative density. The microscopy images were not presented due to a lack of difference with each other. As shown in **Figure 5.13**, the intensity of transverse optic phonon (TO) modes and longitudinal optic (LO) phonon modes for silicon carbide in all hot-pressed specimens is comparable to the intensity for the G band and D band for graphite. Despite the slight non-uniformity of graphite concentration, the intensity attributed to graphite is always comparable to the intensity attributed to silicon carbide.

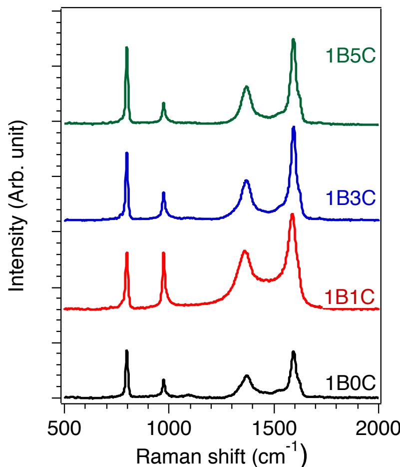

Figure 5.13 Raman spectra of hot-pressed SiC with 1 weight percent of boron additive and 0, 1, 3 and 5 weight percent carbon additive were obtained.

With the probing depth of 100-200 nm for graphite, 100 μm for SiC 3C polytype, and 300 μm for SiC 6H polytype it seems there is better intermixing for hot-pressed specimens and better localized enrichment for PIP specimens. Besides the previously discussed intrinsic excess carbon from the silicon carbide forming polymer, AHPCS, there is a fabrication factor. For the PIP process, there is further enrichment on the surface due to the disproportional presence of reactive function groups on the polymer,

AHPCS, and on the carbon additive, divinyl benzene. Since divinyl benzene is more active than the AHPCS, a carbon rich layer formed with multiple cycles of the PIP process. The fact that graphite signature pattern only found in Raman spectra but not in XRD suggests that the carbon layer has local bonding characteristic of graphite, but that no crystalline graphite was found. For the HP process, there have been grinding and milling to ensure homogeneous mixing and thus there is no enrichment of carbon observed from the Raman spectra.

In summary, we attempted to characterize this novel class of materials created with both the PIP process and HP process using various techniques. XRD, XPS, ^{29}Si NMR, GDOES and Raman spectroscopy were applied. The PIP process produces samples with low relative density, more carbon rich areas and mostly silicon carbide 3C polycrystalline. The HP process generated samples with high relative density, comparable excess carbon and with mostly silicon carbide 6H polytype. The source of excess carbon is from intentionally added vinyl benzene and residual allyl group in the polymer AHPCS.

5.2 Electrical resistivity measurement at elevated temperature

Many efforts have been made to improve the data acquisition procedure and prevent such silicon deposition from occurring to minimize sources of error. In summary, the graphite wrapping mechanism can prevent Pt-Si alloy formation by preventing physical contact, graphite powder in adjacent to specimens for gettering and the titanium wire serves as Si scavenger. The author hopes this work can serve as a guideline so researchers do not go through the same testing process.

5.2.1 Electrical resistivity of hot-pressed SiC/C

The electrical resistivity results obtained for hot-pressed PDC-SiC/C utilizing the customized high temperature apparatus will be discussed. First, two procedures for electrical resistivity measurement were compared to assess the reliability of the pseudo-4-wire arrangement. Then the electrical resistivity results come next based on the finding of this comparison between the two data acquisition procedures. Detail about these two procedures can be found in page 32.

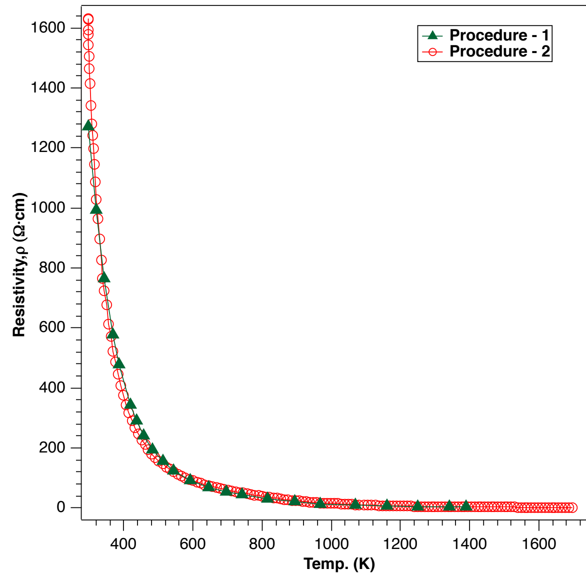

Figure 5.14 Comparison between data taken from procedure 1 (green solid triangle) and procedure 2 (red open circle).

As shown **Figure 5.14,** the comparison of the resistivity-temperature relationship obtained by the two experiments. Data represented by green solid triangles were obtained using **Procedure – 1**, whereas data shown by red-open circles were collected using **Procedure – 2**. From this demonstration, no differences in the quality of data were identified in the temperature range of room temperature to 1400 K. Since the resistivity of samples remains in the same range, the error due to pseudo-four-wire arrangement remains the same, which is negligible; therefore, we adopted **Procedure-2** as a standard

measuring technique to study the temperature dependence of electrical conductivity in this program.

Table 6. Chemical analysis of the hot-pressed ceramics in weight percentage and atomic percentage in parenthesis

Sample ID	B(0B1C)	C(1B5C)	D(1B1C)	E(1B0C)
Si	NA	62.2 ± 0.2 (44.5)	64.9 ±1.8 (47.3)	66.4 ± 0.6* (47.8)
C	NA	32.3 ± 0.1 (54.0)	30.1 ± 0.1 (51.2)	30.2 ± 0.0 (50.7)
B†	NA	0.4 ± 0.0 (0.8)	0.4 ± 0.0 (0.8)	0.4 ± 0.0 (0.8)
O†	NA	0.6 ± 0.1 (0.7)	0.6 ± 0.1 (0.7)	0.6 ± 0.1 (0.7)
Free-carbon#	NA	5.6 (9.5)	2.2 (3.9)	1.7 (2.9)
Relative density	87%	94%	99%	96%

* wt%, mol% in parenthesis. Error is two standard deviation of the mean.
† Measured only for **E(1B0C)**. The values for **D(1B1C)** and **C(1B5C)** were assumed equal to those measured for **E(1B0C)**.
\# Estimated assuming all the Si atoms are bonded to carbon.

Electrical resistivity measurements of samples **B**, **C**, **D** and **E** were carried. The detailed doping, density and chemical composition information of each sample are show in **Table 6**. The numbering in the parentheses xByC indicates the nominal weight percentage for excess boron and carbon, respectively. Samples **C(1B5C)** and **E(1B0C)** are two distinctly different sets of materials in terms of carbon additive. Resistivity of these two samples were measured for temperatures up to 1750˚C, and shown in **Figure 5.15**. For comparison, data from sample **D(1B1C)** and **B(0B1C)** were also plotted in **Figure 5.15**. The resistivity versus temperature curves measured from samples **D** and **E** were nearly identical, and samples **C** and **B** behaved similarly.

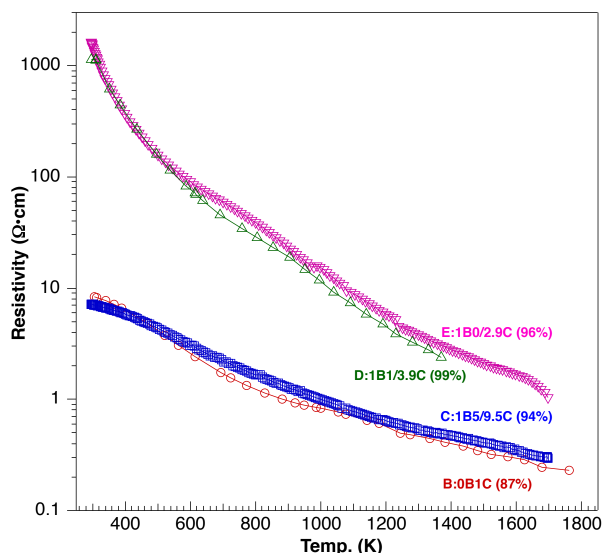

Figure 5.15. Electrical resistivity versus temperature for samples B(0B1C), C(1B5C), D(1B1C) and E(1B0C).

The results presented here bring a couple interesting perspectives; first, the electrical conductivity was measured up to 1750˚K (or 1477˚C), and all materials showed semiconducting behavior, where as the electrical resistivity decreases as the temperature is raised, at all temperatures examined. It is also found that the electrical conductivity does not depend to the density. Interestingly, the materials with lower density exhibited better electrical conductivity by approximately 2 orders of magnitudes around RT and 1 order of magnitude at T>1000˚K, which is opposite of the expected behavior. This implies that samples **D** and **E** may have electrically connecting phase within the materials. Although the amount of excess carbon (by looking at the amount of divinylbenzene added) does not show a strong correlation to the electrical conductivity at first glance, we may still surmise the extra carbon species facilitates electrical conductivity from, the XPS C1*s* spectra (**Figure 5.4(a)**) and ICP-AES (**Table 6**). XPS analysis showed distinct graphitic carbon phase in samples **B** and **C**; thus, better electrical conduction must come from these conducting pathways established by the existing graphitic components. This

finding is also consistent with the elemental analysis result in which high free carbon was found in sample **C** (9.5 mol%).

In the attempt to elucidate the nature of electron transport, the measured data were plotted to fit an Arrhenius equation $\sigma = \sigma_0 \exp(-\Delta E / k_B T)$ in **Figure 5.16**.

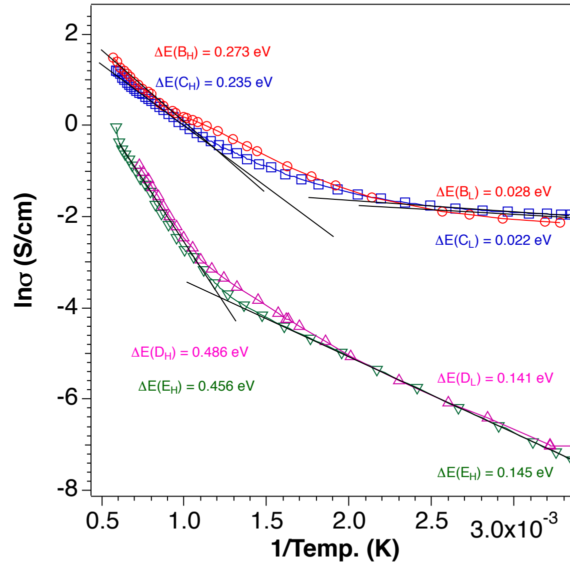

Figure 5.16. Arrhenius plots of the conductivity data from samples B, C, D and E. Activation energy is shown for each sample in two different temperature range.

In the equation, σ_0, ΔE and k_B are a pre-exponential factor, the activation energy, and the Boltzmann constant, respectively. While the activation energy ΔE is the gap between the Fermi level and the energy state to which the electrons are excited, the data does not follow this equation for all temperatures; however, the Arrhenius fit can be accommodated by two different activation energies. In this analysis, it is found that the activation energies from RT up to ~800 ˚K were in the range of 25 meV for samples **B** and **C**, and 140 meV for samples **D** and **E**. Recalling that the thermal energies are 26 meV and 70 meV at RT and ~800 ˚K, respectively, the electrical conduction at T < 800˚K might be explained by the thermal activation of the charge carriers. Difference in the activation energies for samples B and C versus sample D and E are correlated with the

difference in the level of free carbon in the samples. For temperatures higher than 800˚K, however, the activation energy becomes much larger (~240 meV for samples **B** and **C**, and ~460 meV for sample **D** and **E**, indicating that the Fermi energy is moved away from the conduction band minimum. This kind of two activation energies behavior has been reported for other polymer-derived ceramics (SiCNO). [60]

In the band-gap model for semiconductors, the conductivity is controlled primarily by the concentration of the charge carriers, which is determined by thermal activation of charge carrier from highest occupied state to the mobile state. While the band conduction model reasonably explains the temperature dependence of the conductivity data, there are other models that can be also applied to fit the data. Shown in **17** (a) and (b) are the results of fitting the electrical conductivity (σ) data of the samples at different temperatures with the adiabatic small polaron hopping (SPH) model and 3-D variable range hopping (VRH) models, respectively. For small polaron (i.e., nearest neighbor) hopping, the relationship between the electrical conductivity and temperature may be expressed as:

$$\sigma = \frac{A}{T}\exp\left(-\frac{E_a}{kT}\right)$$

where A is a pre-exponential factor, T is temperature, k is the Boltzmann constant, and E_a is the activation energy for small polaron hopping. Alternatively, the electrical conductivity arising from 3-D variable range hopping may be modeled as:

$$\sigma = \sigma_0 \exp[-(T_0/T)^{1/4}]$$

where σ_0 is a temperature-independent constant and T_0 is a constant known as the characteristic temperature.

Conductivity data obtained from Samples **B**, **C**, **D** and **E** were analyzed using the polaron models described above. To identify the nature of the electron transport mechanism, on the left is the data plotted into a ln(σT) vs 1/T form based on the small polaron hopping (SPH) model, whereas a ln(σ) vs $1/T^{1/4}$ form for the variable hopping (VRH) is on the right in **Figure 5.17**. As is evident from these analyses, both models yield reasonable fits to the data; therefore, it is difficult to draw any definitive conclusions as to which model describes the behavior.

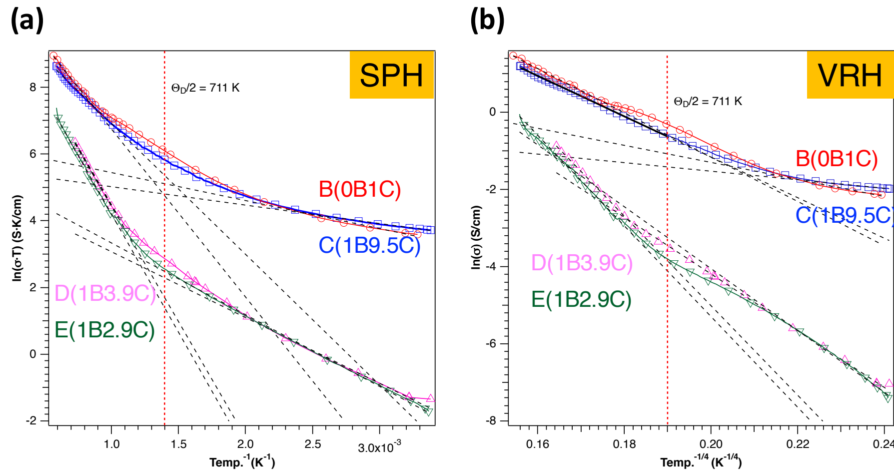

Figure 5.17. Attempts to fit the electrical conductivity data by (a) small polaron hopping (SPH) and (b) variable range hopping (VRH) models.

The small polaron hopping (SPH) model was achieved over two temperature ranges below and above 600K (designated "low temperature" and "high temperature", respectively). The activation energies calculated from the slopes of the lines in **Figure 5.17** (left) are shown in **Table 7** below. An optimum fit with the 3-D VRH model was also observed in the temperature range of above and below 600˚K.

Table 7. Activation energy of the samples estimated with SPH transport mechanism.

Activation Energy (meV)	**B(0B1C)**	**C(1B9.5C)**	**D(1B3.9C)**	**E(1B2.9C)**
High temperature	434	338	597	610
Low Temperature	72	48	170	185

Conventionally, VRH model is based on single phonon emission or absorption, and may only be valid for hopping between impurity state at very low temperatures. [58] On the other hand, the SPH model describes electrical conduction that occurs by small polarons between different states in the temperature higher than half of the Debye temperature (Θ_D). [59] For a system in which the SPH model is observed, strong electron-phonon coupling results thermally activated electrical conduction above Θ_D /2. Below Θ_D /2, the number of thermally activated charge carriers is reduced and so is the electrical conductivity. In this scenario, electrical transport relies on hopping between impurity states around the Fermi level. The fact that both polaron models are achieved indicates that localized electrons simply do not have sufficient energy to overcome the potential barrier associated with movement to an adjacent site. Consequently, it is energetically favorable for an electron to hop further to a site where the potential barrier is much lower. As the temperature is raised to within a certain range, the thermal energy required for the excitation of electrons to the conduction band is still too great. However, the barrier associated with an electron hopping to an adjacent site is much lower and thus, small polaron hopping ensues.

5.2.2 Electrical resistivity of polymer-infiltration-pyrolysis (PIP) SiC/C

The electrical resistivity results obtained for polymer-infiltration-pyrolysis (PIP) PDC-SiC/C will be discussed. Since we gained many valuable insights from the electrical

resistivity data acquisition at high temperature from hot-pressed specimens, the results presented here are straightforward.

As shown in **Figure 5.18**, the electrical resistivity for specimens **PIP(0B0C**) (red, open circle), **PIP(0B5C)** (blue, open square) and **PIP(0B15C)** (green, open triangle) were plotted versus temperature (Kelvin). The measurements were made continuously. While each measurement takes about 60 seconds, there is a halt for every 30 seconds between measurement. Only one of every five data points is shown in the plot for a clearer figure. All the data were collected during the heating process, in which the ramping rate was set as 5 ^{o}C / min.

While the electrical resistivity for hot-pressed samples were from 10 to 1000 Ω·cm at room temperature and 0.2 to 1 Ω·cm at elevated temperature, the resistivity for PIP SiC ranges from 10 to 1 Ω·cm at room temperature and 0.4 Ω·cm at elevated temperature. The electrical resistivity of **PIP(0B0C)** almost overlaps with **HP(0B1C)** and **HP(1B9.5C)**. With excess carbon doping, the electrical resistivity can be further lowered 1 order of magnitude.

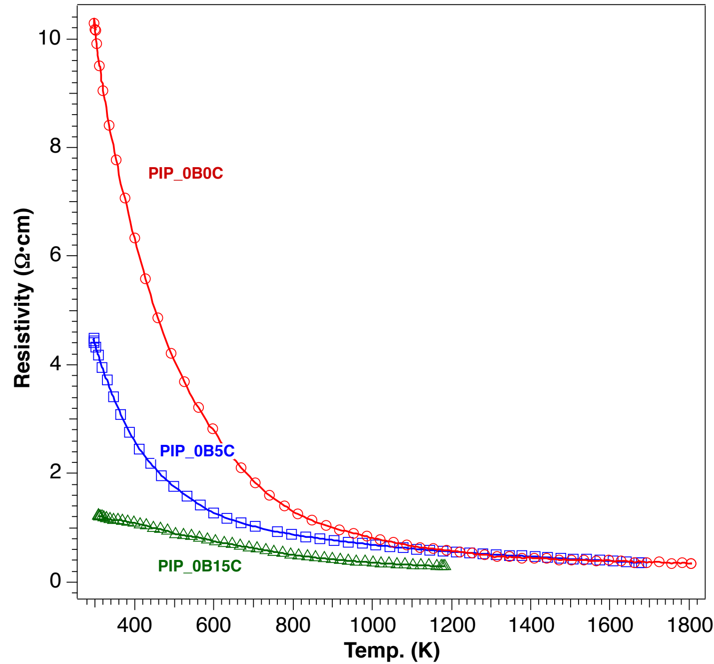

Figure 5.18. Electrical resistivity versus temperature for specimens PIP(0B0C) (red, open circle), PIP(0B5C) (blue, open square) and PIP(0B15C) (green, open triangle).

Knowing that the electrical resistivity of PIP SiC/C samples varies from 10 Ω·cm to 1 Ω·cm at room temperature but not so much different at elevated temperature leads us to think there must be different conduction mechanism. Using the previously mentioned Arrhenius equation, we may be able to solve for the thermal activation energy for electrical conduction. **Figure 5.19** shows the Arrhenius plot of the electrical conductivity as a function of temperature and the corresponding activation energies. It is similar to the Arrhenius plot for hot-pressed specimens. There is no one linear fitting that fits the entire temperature range but there are two activation energies for the materials depending on the temperature. In the low temperature range, the activation energy ranges from 17 to 56 meV; at high temperature range, the activation energy is an order of magnitude higher between 169 to 116 meV.

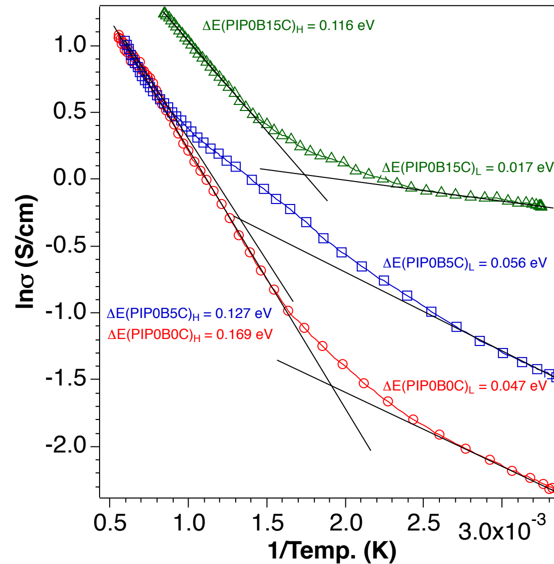

Figure 5.19. Arrhenius plots of the conductivity data from PIP specimens 0B0C, 0B5C and 0B15C. Activation energy is shown for each sample in two different temperature range

It is known that $k_B T$ equals 25 meV at room temperature, 86 meV at 1000 K and 155 meV at 1800 K. Since the activation energy derived from the Arrhenius equation is within the proximity to the thermal energy, we may assume these types of materials follows the band-gap model. This may explain the extraordinarily low resistivity for the heavily carbon doped specimen (**PIP(0B15C)**). In the band-gap model, the conductivity is governed by the majority charge carrier, which in this case is thermally activated from the localized trap states near the Fermi level to its mobile state.

To summarize the electrical resistivity measurements, the data collected from the above-mentioned sections is plotted in **Figure 5.20**. A dotted line for 2 Ω·cm (50 S/m) is drawn to show the maximum requirement for MHD electrode applications. This drastic improvement on the electrical conductivity is due to a surface graphitization which will be demonstrated in the next section.

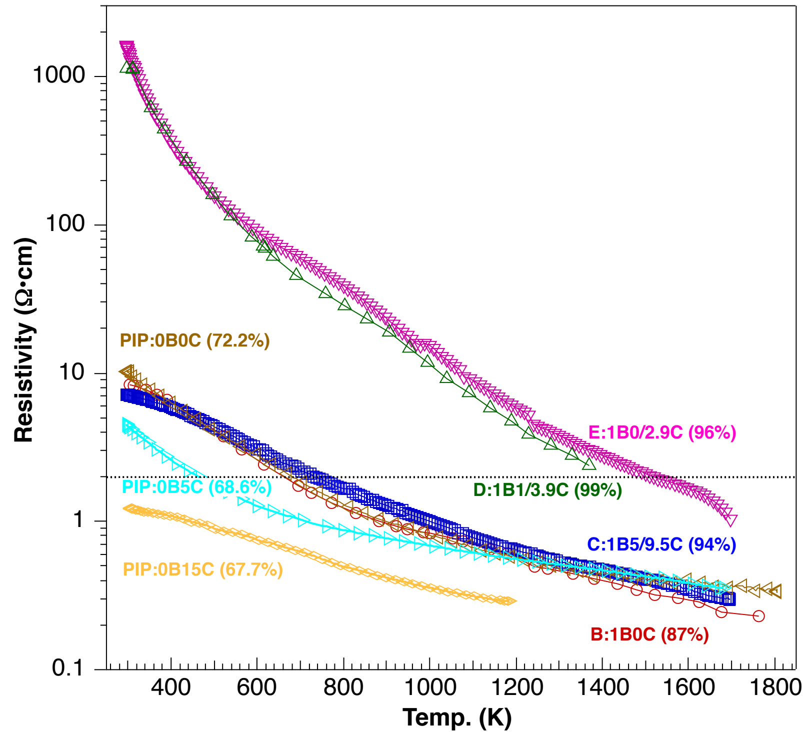

Figure 5.20. Electrical resistivity versus temperature for all specimens from the above sections are plotted in semi-log scale.

In the first phase of material exploratory research, we set out to validate if the materials are suitable for use as a channel electrode in the MHD generator. The efforts have been made on verifying the electrical resistivity at elevated temperature. The later evidence suggested that there is a versatile surface transformation at elevated temperature which will be discussed in **Chapter 6**. On the other hand, the post-measurement examination suggests different magnitudes silicon evaporation. Some silicon species evaporate and deposit at an adjacent location. The silicon species can further form alloys with Pt wire or oxidize and become an insulator.

Chapter 6 Thermionic emission, electron energy distribution and in-situ Auger Electron Spectroscopy

To understand the surface properties of the newly developed materials, the work function of the materials was measured while the Auger electron spectra were taken in-situ. In this section, there are two methods are presented, direct heating and in-direct heating. Direct heating utilizes the Joule heating by passing a D.C. current through the specimens to heat up the specimens resistively; in-direct heating, on the other hand, has the heating element located adjacent to the specimens.

6.1 Thermionic emission achieved from direct heating and in-situ AES

In the case of direct heating, the specimen was heated with a D.C. current. While the cylindrical mirror analyzer (CMA) captures the emission electrons with respect to its kinetic energy, it is essential to know how the applied voltage affects the emission electron spectra. As shown in **Figure 6.1**, AES were taken from single crystal silicon carbide one after another while the specimen was heated resistively to 730 ^{o}C (1000 K). The first spectrum (red) was taken while specimen was negatively biased, and followed by the second spectrum (blue) which was positively biased for 3 eV, the third spectrum (green) was taken while specimen was negatively biased for 3 eV, the forth spectrum (pink) was taken while specimen was not grounded, and the fifth spectrum (light blue) was taken while the specimen was positively biased. Despite the intensity increase for C *KVV*, we notice there is a consistent 6 eV difference between the negatively biased and positively biased spectra. The increase for C *KVV* may be due to carbon layer formation which we will address in detail below. The source of the energy difference may be

attributed to the DC Joule heating voltage. Because of the fact that the heating voltage may accelerate the emitted electron and consequently shift the spectra, the spectra should be adjusted back accordingly for future analysis.

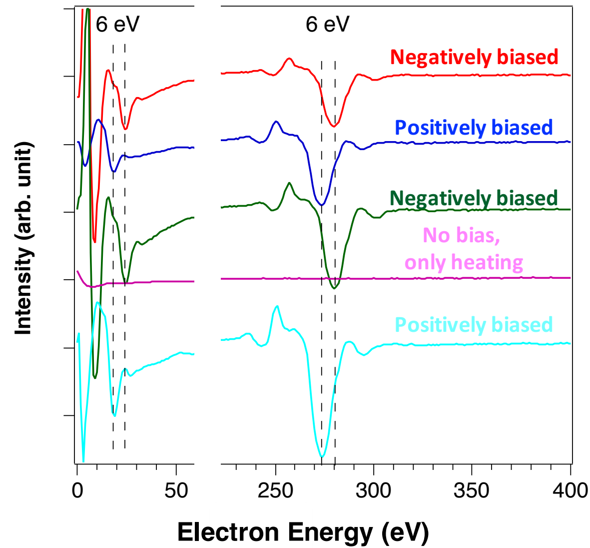

Figure 6.1. AES taken from SiC single crystal to demonstrate the DC voltage brought into the spectrum.

In the following section, AES data acquired from (a) single crystalline SiC, (b) **HP(0B1C)** sample (c) **HP(1B5/9.5C)** sample and (d) **HP(1B1/3.9C)** sample are shown in **Figure 6.2**. For all cases, AES was used to monitor the surface compositions during preparation of the sample surfaces. During the data acquisition, multiple modifications were introduced to the testing specimens including annealing at elevated temperature and Ar-ion sputtering. Ar-ion sputtering was a necessary treatment to clean up the specimen surface. Often times the treatment introduces defects which may alter the chemical shift for the elements of interest. High temperature annealing promotes the surface rearrangement and allows the surface to resume a more reliable state for us to study. High temperature annealing can also provide some insight regarding how the materials react when the temperature approaches to MHD working temperature.

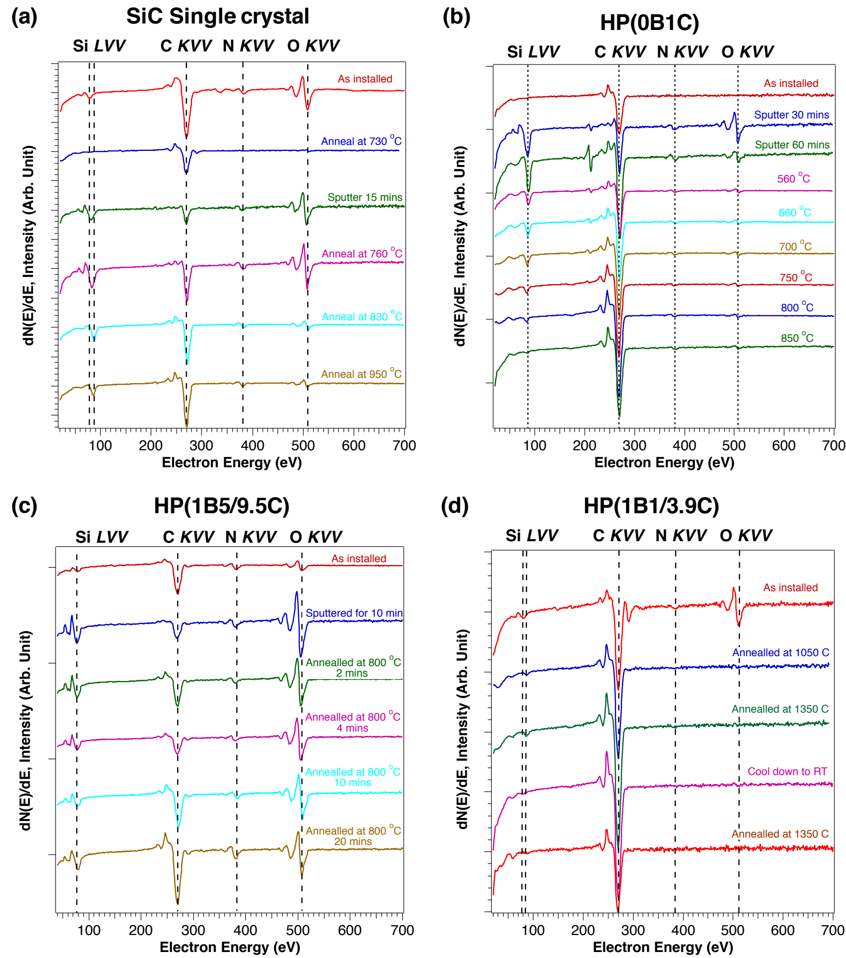

Figure 6.2. A series of Auger electron spectra taken from (a) silicon carbide single crystal, (b) HP(0B1C), (c) HP(1B5/9.5C) and (d) HP(1B1/3.9C).

For every specimen, we saw not only silicon and carbon in the spectrum but also nitrogen and oxygen. The nitrogen and oxygen are surface contaminants from the atmosphere. The Ar-ion gun sputtering was carried out at Ar 10^{-5} Torr while the chamber's nitrogen and oxygen are lower than 10^{-9} Torr. While annealing, oxygen intensity decreased along with silicon intensity and carbon peak became the largest for all cases. The annealing temperature is limited by the resistance of the specimens due to limited power input from the Joule heating power supply.

Thermionic emission (TE) currents were then measured as current to ground as a function of temperature from the following three conditions: "as-installed" in red, "after

Ar-ion sputtering" in blue and "after the last stage of annealing in the AES measurement" in green. Thermionic emission data taken from (a) single crystal silicon carbide, (b) **HP(0B1C)** and (c) **HP(1B1/3.9C)** are shown in **Figure 6.3** (a), (b) and (c), respectively.

The data were then analyzed by the Richardson-Dushman's thermionic emission theory [32] by plotting $\ln(I_{TE}/T^2)$ versus 1/T in **Figure 6.3** (d), (e) and (f). There are two important physical parameters constituted the Richardson-Dushman equation

$$J(T) = A_R T^2 e^{-\frac{\Phi}{k_B T}}$$

where Φ is the material work function and A_R is the Richardson's constant equals to $4\pi m k_B^2 e/h^3$, T is temperature of emitter surface and k_B is Boltzmann's constant. Although Richardson's constant is a universal constant for pure metallic emitters assuming a standard free electron density of state, experimental value often deviates from it. Nevertheless, rearranging the above equation allows for direct determination of the work function from the emission current versus temperature data without the concern of Richardson constant. The work function can be determined in the conventional manner from the slope of the Richardson plot; however, it is not able to obtain a good linear fit through the whole temperature range for "as installed" samples. This is because the surface composition changes with temperature, thus the work function and the Richardson constant are constantly changing. However, after annealing to 900 ~ 1350 ^{o}C (i.e. "after anneal"), estimated values of the work function converge to around 4.1 eV, which is in the range of graphite (4.6 eV) [61] and graphene (4.2 eV) [36]. The details of the work function in different stages are tabulated in **Table 8**.

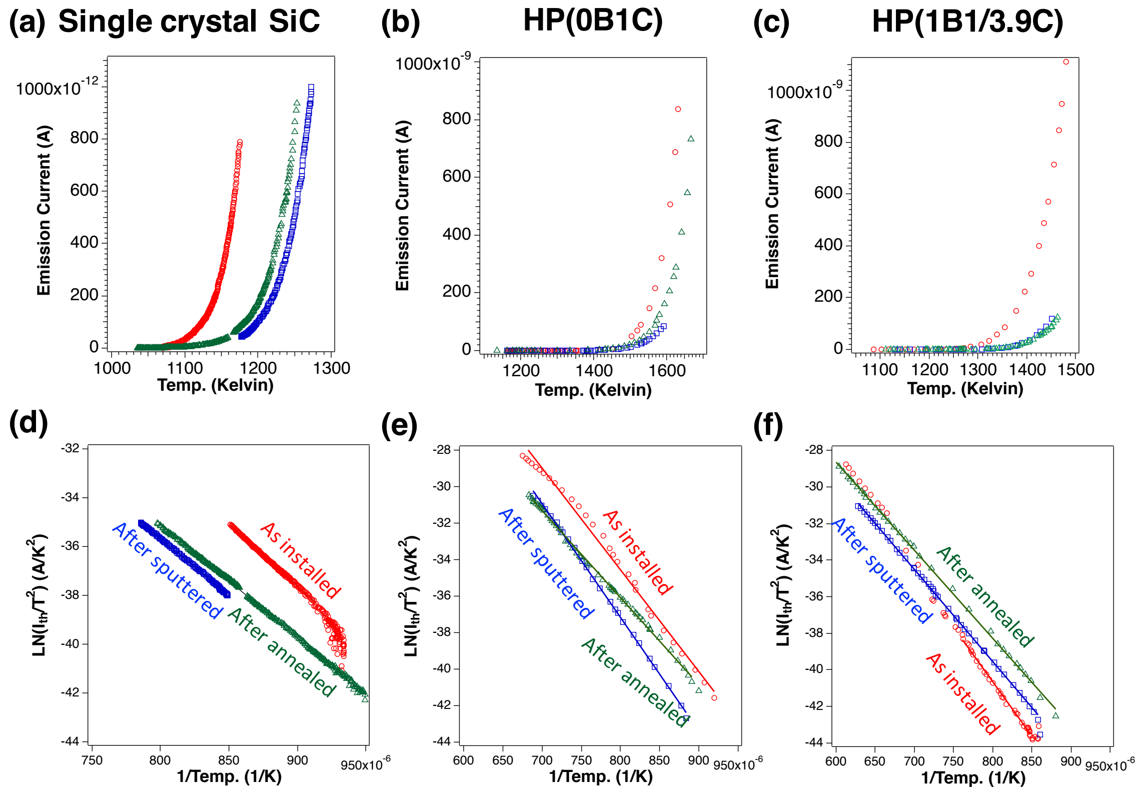

Figure 6.3. Thermionic emission data taken from (a) silicon carbide single crystal, (b) HP(0B1C) sample, and (c) HP(1B1/3.9C) sample; Richardson –Dushman of the TE data obtained from (d) silicon carbide single crystal, (e) HP(0B1C) sample and (f) HP(1B1/3.9C) sample.

Table 8 Work function values estimated from slope deduced from Richardson-Dushman's equation in eV.

	SiC_SC	HP(0B1C)	HP(1B1/3.9C)
As installed	3.39	4.8	5.52
After sputtering	4	5.36	4.34
After annealing	4.02	4.09	4.12

Followed the in-situ AES-TE for hot-pressed specimens, one attempt to acquire in-situ AES – TE correlation data for PIP specimen is presented.

AES data acquired from **PIP(0B0C)** is shown in **Figure 6.4**. As described in the previous section, the data acquisition involves Ar ion gun sputtering and high temperature annealing through Joule heating. The data was taken while the specimen was heated to the indicated temperature, and when the data acquisition was done (~ 5 mins),

the specimen was heated to next temperature. Above 950 ^{o}C, there is no significant oxygen peak can be observed.

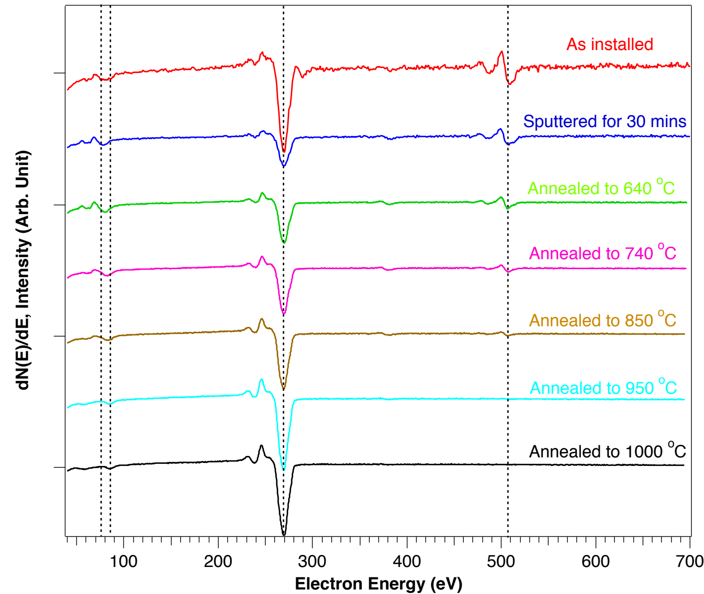

Figure 6.4. A series of Auger electron spectra taken from silicon carbide specimen (0B0C) prepared from PIP route, as installed (red), sputtered 30 mins (blue), annealed to 640 ^{o}C (green), annealed to 740 ^{o}C (purple), annealed to 850 ^{o}C (brown), annealed to 950 ^{o}C (light blue), and annealed to 1000 ^{o}C (black) from top to bottom respectively.

This higher rate of graphite formation observed from AES only applies to the r surface composition. However, upon the completion of 1000 ^{o}C AES data acquisition, the sample cooled down spontaneously. The sample was too conductive and thus the power supply was not able to heat the sample up resistively.

To summarize the direct heating for in-situ AES and TE section, the HP specimens showed similar graphite layer growth on the surface regardless of the sample compositions; the PIP specimens exhibited the same trend of graphitization on the surface with a faster rate. Besides the aforementioned disadvantage, the applied external voltage provides an unknown amount energy to the emitted electrons and makes it impossible to study the electron energy distribution. And thus, in the following section, an external

heating source were installed and a series of experiments were done to validate this data acquisition procedure.

Thermionic emission and in-situ Auger electron spectroscopy for various silicon carbide specimens has been analyzed in the previous chapter. There are great advantages on the simplicity of using direct Joule heating. However, with some adjustments to the sample holding apparatus, in-direct heating is possible to utilize the full potential of this AES-TE high vacuum chamber for surface investigation.

6.2 In-direct heating AES and thermionic emission and energy distribution

In the era of thermionic emission investigation (from 1930s to 1960s), there are plenty of experiments reported from various sources. For typical experiments conducted in those days, a dedicated cell or chamber was assembled and baked to outgas for as many as 2500 hours, and emission currents were measured under a steady state condition. [62] As for temperature measurement, both direct temperature through simple thermocouples [63] and in-direct pyrometer [62] were utilized. Thermocouples can be used for straightforward and quick for temperature measurement. However, there is always a concern temperature gradients between the sample and thermocouple should they not be touching, or inter-diffusion and reaction if they are. On the other hand, a pyrometer is a non-contact method but it requires more information such as the temperature dependent spectral emissivity. [64] As novel class of materials are created, such temperature dependent spectral emissivity information are often unavailable and thus, in the appendix, we investigated a measurement method that utilized a spectrometer

for multiple two-color pyrometer that does not require known temperature dependent spectral emissivity.

Experimental procedure: In the previous section, section 6.1, thermionic emission currents were collected from the sample heated by a passing D.C. current. The Joule heating setup is shown in **Figure 6.5(a)**, in which a total current to ground was collected using a metal screen in front of the sample. In this method, in addition to the disadvantages mentioned above, an entire sample never reaches the same temperature due to non-uniformity of the contacts and resistivity, as well as heat loss from thermal conduction through the wires. An aperture in front the sample can collect emitted electrons from a uniform-temperature region, and better temperature uniformity shall be reached. In the re-design for indirect heating, the same Joule heating setup was retained as heat source; as shown in **Figure 6.5(b)**, the specimens were attached on a stainless-steel eV part and installed in front of the heating element as close as 1 mm distance. The specimens were cut into 15 mm diameter and 1.5 mm thickness, and attached to the stainless-steel Kimball eV part [65] using Ta ribbon with minimum area of contact. The sample holder is electronically isolated and it allows us to adjust the bias voltage, $\mathbf{V_{B2}}$, shown in **Figure 6.5(b)**.

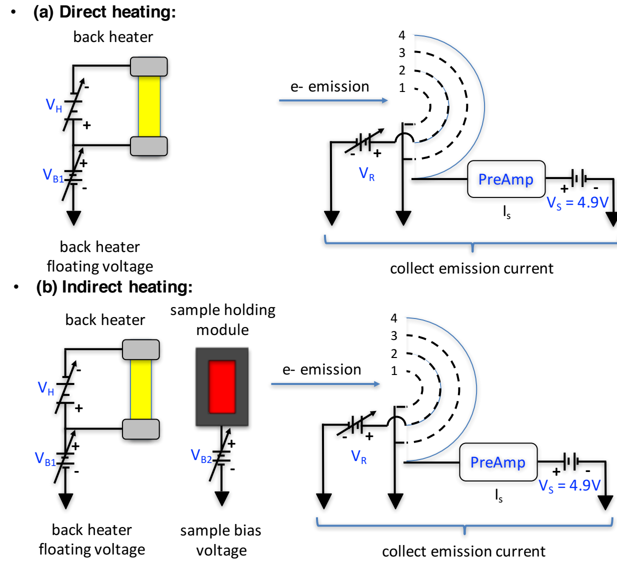

Figure 6.5(a) simplified setup for collecting thermionic emission from Joule heating; (b) simplified setup for collecting thermionic emission from indirect heating, mainly thermal radiation.

6.2.1 Control Experiment 0, no sample

In the *Control Experiment 0*, the setup is almost identical to the setup shown in **Figure 6.5(b)**, except there is no sample installed on the stainless-steel plate (Kimball Physics Inc.). The purpose for this control experiment is to eliminate the thermionic emission from heater, as we intend to acquire thermionic emission from another hot spot in the chamber. As shown in **Figure 6.6**, heating element, CVD SiC, is supplied with heating voltage, $\mathbf{V_H}$, and biased with bias voltage, $\mathbf{V_{B1}}$. Emission current, $\mathbf{I_S}$, versus retarding voltage, $\mathbf{V_R}$, is then collected at different temperatures.

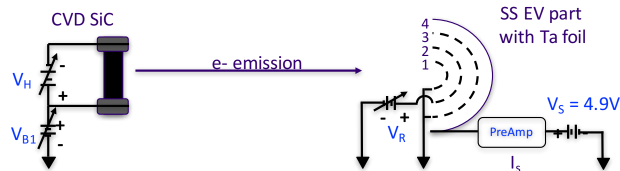

Figure 6.6 Experimental setup for control experiment 0, heating element only.

Although there are four set of data acquired for this purpose, at first, only one set of data acquired at 1030 ^{o}C, will be explained in detail (**Figure 6.7**) and the rest will only

be shown for reference (**Figure 6.8**). In **Figure 6.7(a)**, the emission current was plotted versus retarding voltage, $\mathbf{V_R}$; **Figure 6.7(b)** is an enlarged view of the emission current from $\mathbf{V_{B1}}$ = 8 to $\mathbf{V_{B1}}$ = 15 volts. Despite abnormal increasing in emission current for $\mathbf{V_{B1}}$ = 2 and $\mathbf{V_{B1}}$ = 3, there is a clear trend that the emission current decreased upon increasing $\mathbf{V_{B1}}$. In **Figure 6.7(c)**, the first derivative of emission current, $\mathbf{I_s}$, versus the retarding voltage, $\mathbf{V_R}$, for $\mathbf{V_B}$ = 1 to $\mathbf{V_B}$ = 5 is shown. One may infer the emission current from heating element carries about 10 volts from heat power supply with a width about 2 volts, provided from the heating voltage, $\mathbf{V_H}$, and thus it can be suppressed by providing bias voltage, $\mathbf{V_{B1}}$ .The resulting peak intensity moved incrementally toward the positive direction when the bias voltage increases. Since the number of electrons that can pass through the retarding voltage were limited by the application of bias voltage, $\mathbf{V_{B1}}$, we can also observe the reduction of intensity along with increasing bias voltage. As shown in **Figure 6.8**, the thermionic emission acquired from 1080 ^{o}C, 1105 ^{o}C and 1300 ^{o}C were also recorded. The absolute intensity increases with respect to heater temperature; however, the emission current can be eliminated in all temperature ranges upon applying proper bias voltages.

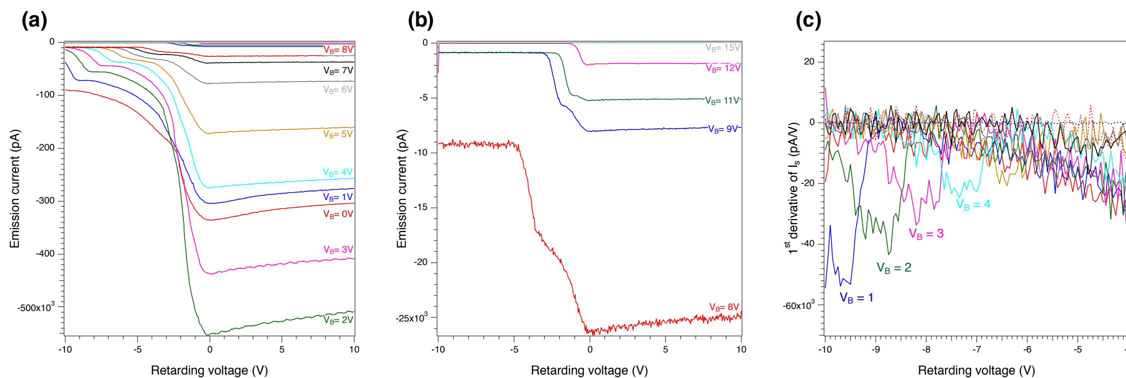

Figure 6.7 Emission current, $\mathbf{I_S}$, plotted versus retarding voltage, $\mathbf{V_R}$ for (a) $\mathbf{V_B}$ = 0 to $\mathbf{V_B}$ = 8, (b) $\mathbf{V_B}$ = 8 to $\mathbf{V_{B1}}$ = 15 and (c) first derivative of Is for $\mathbf{V_B}$ = 1 to $\mathbf{V_B}$ = 5 at 1030 ^{o}C.

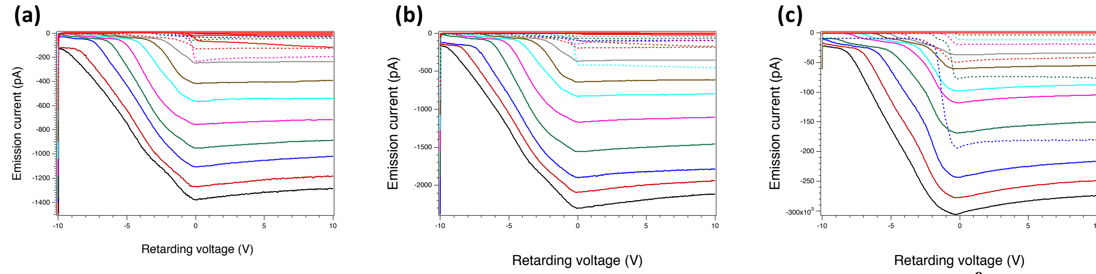

Figure 6.8 Thermionic emission current versus retarding voltage, taken at (a) 1080 ^{o}C, (b) 1105 ^{o}C and (c) 1300 ^{o}C, varying V_{B1} from 0 volt to 15 volts.

Next we take a closer look at different bias voltages ($\mathbf{V_{B1}}$). Since the heating voltage, $\mathbf{V_H}$, increases when we increase temperature, bias voltages ($\mathbf{V_{B1}}$) is not a universal indicator for this exploration. Alternatively, the voltage difference between the heating voltage ($\mathbf{V_H}$) and bias voltage ($\mathbf{V_{B1}}$), namely, $\mathbf{V_H} - \mathbf{V_{B1}}$ may be a better indicator for our reference. At this point, we expect the natural width of the electron emission only carry a few eV of kinetic energy, and thus, we are mostly interested in the magnitude of background emission at $\mathbf{V_R} = 0$. After acquiring multiple $\mathbf{I_s}$ versus $\mathbf{V_R}$ at different bias voltages ($\mathbf{V_B}$), at temperatures equal to 1030 ^{o}C, 1086 ^{o}C, 1105 ^{o}C and 1340 ^{o}C, we extract the emission current at $\mathbf{V_R} = 0$ for each condition and re-plotted in **Figure 6.9**. On the left-hand side, the background emission is suppressed within the shown range, namely $\mathbf{V_H} - \mathbf{V_B} = 0 \sim 2$, for temperatures below 1105 ^{o}C; on the right-hand side, closer examination shows the emission from heating element and its surrounding can be reduced to the magnitude of ten pico Amperes for all examined temperatures. The assumption that electrons are emitted from the specimen of interest may not hold true as we could introduce a second bias voltage, $\mathbf{V_{B2}}$, to the specimen. This does not hurt the validity for minimizing background emission at $\mathbf{V_R} = 0$.

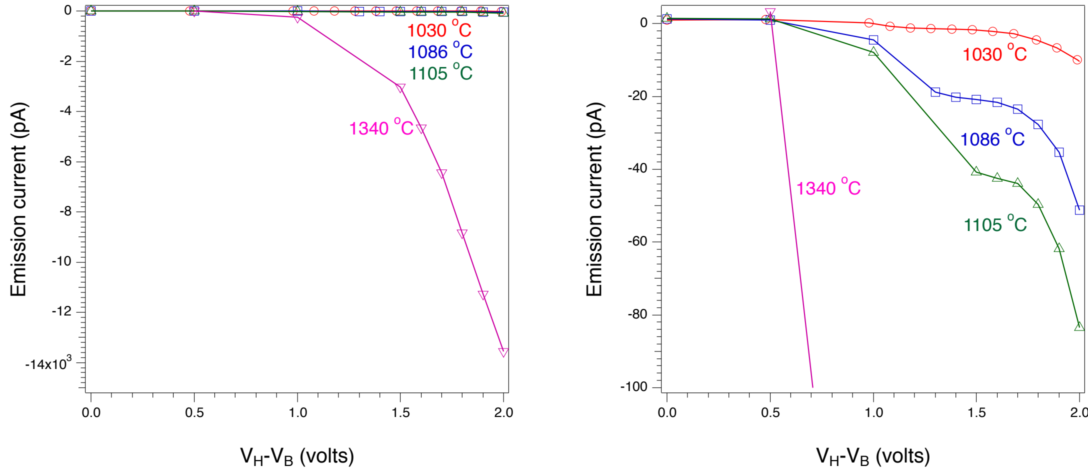

Figure 6.9 Emission current at various temperature were plotted with respect to the difference between heating voltage and bias voltage, $V_H - V_B$. Figure on the right is the enlargement for the figure on the left

6.2.2 Effect of V_{B1} in the presence of PIP SiC specimens

Once we understood the effect of bias voltage (**V_{B1}**) applied on the heating element, we went ahead to perform similar experiments with the presence of a desired sample, in this case, a polymer-infiltration-pyrolysis silicon carbide, PIPSiC_0B1C. The schematic setup can be seen in **Figure 6.5(b)**.

Figure 6.10 (a) to **(c)** and **Figure 6.11(a)** summarized the effects of **V_{B1}** on reducing emission from heating element. As shown in **Figure 6.10(a)**, for **V_{B1}** = 0, emission current from the heater dominates the emission, and the sample bias, **V_{B2}**, works like an energy barrier. With **V_{B2}** = -7 volts, the majority of the emission current is suppressed; increasing **V_{B2}** results in an increase for the collected current, which does not shift with respect to **V_{B2}**. Increasing **V_{B1}** to 5 volts, there is a clear onset on the retarding spectra (**Figure 6.10(b)**). The bias voltage to the heating element successfully pulled the electric potential down and thus the emitted electrons carried 5 volts less when compared to **V_{B1}** = 0. The same phenomenon holds true for **V_{B1}** = 10 volts, which is shown in

Figure 6.10(c). Lastly, we set $\mathbf{V_H} = \mathbf{V_{B1}} = 14.3$ volts. As shown in **Figure 6.11(a)**, **(b)** and **(c)**, all three sets of data were taken with $\mathbf{V_H} = \mathbf{V_{B1}} = 14.3$ volts. While the chamber was able to pump down to 1.1×10^{-8} Torr at rest, the outgassing during heating could bring the pressure up to 1.1×10^{-6} Torr.

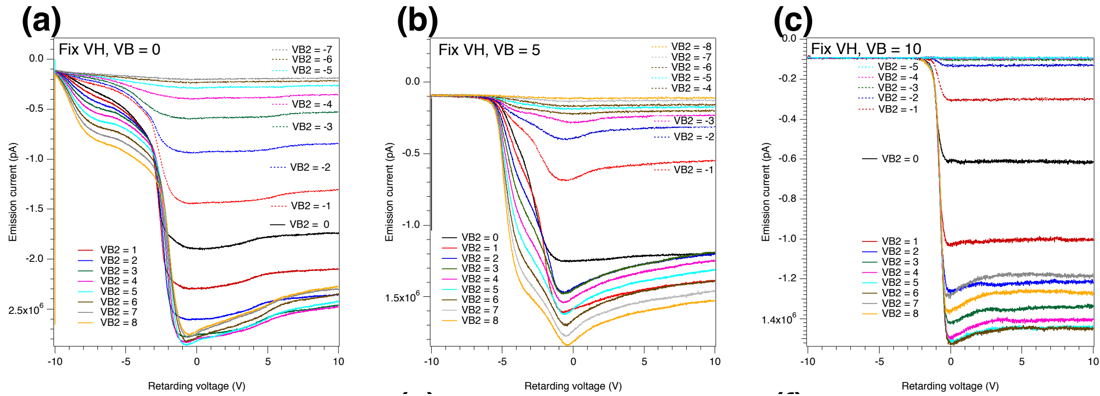

Figure 6.10 Emission current versus retarding voltage for PIP0B1C sample for various V_{B2}, at (a) $V_B = 0$, (b) $V_B = 5$, (c) $V_B = 10$ volts.

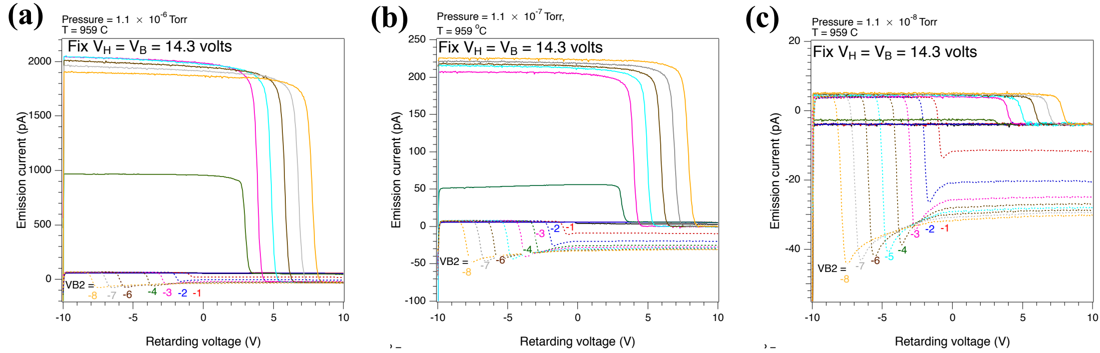

Figure 6.11 Emission current versus retarding voltage for $V_H = V_B$ at the same temperature (959 °C) while chamber pressure is at 10^{-6} Torr, 10^{-7} Torr and 10^{-8} Torr for (a), (b) and (c), respectively.

While maintaining $\mathbf{V_H}$ and $\mathbf{V_B}$, emission current versus retarding voltage was recorded at sample bias voltage ($\mathbf{V_{B2}}$) vary from -8 to + -8 volts. As expected, the bias voltage pulled down the potential of the emitted electron. We can observe a clear cut at a certain retarding voltage. From **Figure 6.9**, we learned that we can totally suppress electron emission when we put $\mathbf{V_H} - \mathbf{V_{B1}} < 1$ volt, and there is no observable emission at $\mathbf{V_R} = 0$ when $\mathbf{V_H} = \mathbf{V_{B1}}$. In **Figure 6.11(a)**, **(b)** and **(c)**, the emission current was collected

at almost identical conditions except chamber pressure differed by 1 order of magnitude. The magnitude of positive emission went from 2000, 250 to less than 10 pA. Despite the huge difference in positive emission, the magnitude of negative electron emission remains similar. The incremental shifting of negative emission indicates the electron is coming from the sample instead of the surrounding vacuum or the heater. We successfully peeled away the 10^6 pA background emission and see the ~50 pA desired signal from sample.

6.2.3 Tungsten

After successfully removing the electron emission of heating element and background, the next step is to prove the validity of the method. A polymorphous tungsten sheet (Midwest Tungsten Service) has been investigated as a reference study. The sample has been treated and cleaned per the regular tungsten cleaning method [66] and sputtered with the Ar ion gun followed by annealing at 1000 ^{o}C in a high vacuum chamber. The Auger spectra shows unexpected big peaks for carbon and oxygen (shown in **Figure 6.12**) at room temperature. However, the surface changed drastically and both the carbon and oxygen peaks diminished as the temperature rose. The Auger spectrum for tungsten at 1000 ^{o}C shows an identical pattern with spectrum from Auger handbook. [67]

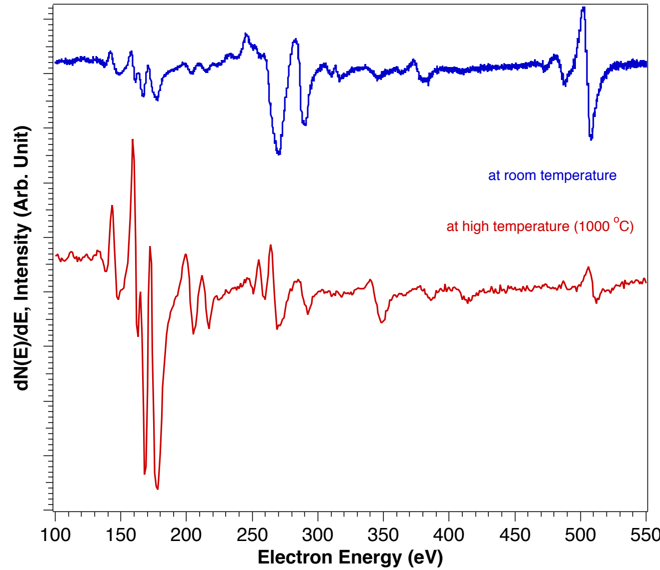

Figure 6.12 Auger electron spectra for polymorphous tungsten acquired at room temperature (blue) and at 1000 °C (red).

With confidence in the surface composition, we examined the thermionic emission current versus the retarding voltage for $\mathbf{V_{B2}}$ = -8 at the above temperature and plotted the result in **Figure 6.13(a)**. The abrupt current increase at around -8 volts can be attributed to thermionic emission from sample. The reason for choosing $\mathbf{V_{B2}}$ = -8 will be addressed in the next section. The magnitude of the emission current drop in the **Figure 6.13(a)** is extracted and attributed as thermionic emission current at the specific temperature. In **Figure 6.13(b)**, there are two sets of data acquired; one was acquired over the course of heating the sample which is shown in blue and the other was acquired while the sample was cooling which is shown in red. The emission current was extracted by measuring the difference the current difference on **Figure 6.13(a)** and plotted with respect to temperature (**Figure 6.13(b)**) and the Richardson-Dushman plot is shown in **Figure 6.13(c)**. The work function calculated from Richardson-Dushman equation is 4.35 ± 0.11 eV for cooling (higher temperature) and 4.63 ± 0.02 eV for heating (lower

temperature). For reference, the work function for tungsten is known to be 4.54 eV [68], 4.59 eV [62] and 4.60 eV [69].

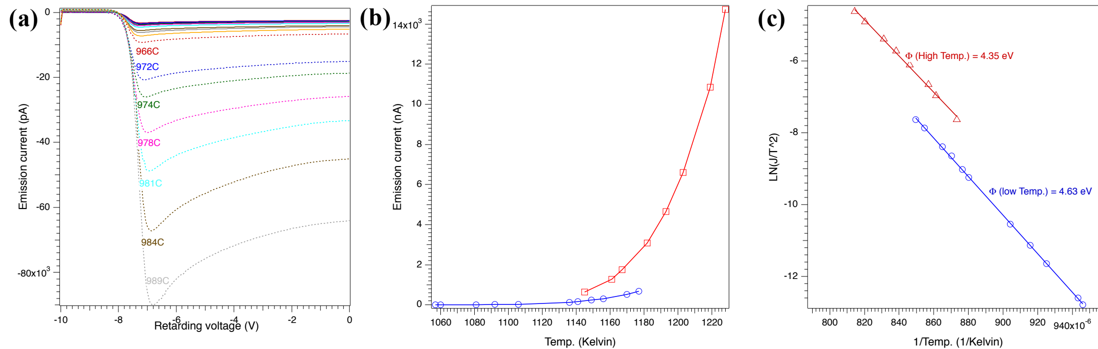

Figure 6.13 (a) Thermionic emission current versus retarding voltage for V_{B2} = -8 at the above temperature for polycrystalline tungsten; (b) emission current was plotted with respect to temperature and (c) the Richardson plot.

From the above information, the experimental procedure provided is as capable as what people have done in the past. In addition, the bias voltage method clearly "labeled" the number of electrons that came out of sample and the number of electrons that are considered background noise. The in-situ spectroscopy capability provides a tool to understand the materials composition at the working temperature. In the extreme case, such as tungsten (shown in **Figure 6.12**), the surface compositions differ at different temperatures as the surface may absorb chamber residue gas. Lastly, the method requires less chamber or cell out-gas procedures. Instead of thousands of hours at 1500 ^{o}C, the chamber can be baked 2 to 3 days and be ready for acquiring data. The discrepancy of heating and cooling will be addressed with energy distribution analysis in the following section.

6.2.4 Polymer-infiltration-pyrolysis (PIP) silicon carbide

There are two clarifications that need to be addressed before moving forward, 1. the temperature dependence of emission and 2. which $\mathbf{V_{B2}}$ to choose. In the section 5.2.1,

thermionic emission currents from tungsten were extracted from the magnitude of emission current drop without further clarification. We should first demonstrate the temperature dependence of electron emission and secondly we'll determine the emission current and sample bias voltage ($\mathbf{V_{B2}}$) relationship.

According to the Richardson-Dushman equation, the emission current at each temperature from a fixed surface area should be a fixed value. However, the amount of emission current varies with sample bias voltage ($\mathbf{V_{B2}}$). This variation may be attributed to the sample, collector geometry, and focusing effect from the retarding grid. In **Figure 6.14**, the emission current versus retarding voltage for the sample PIP0B0C were acquired with $\mathbf{V_{B2}}$ = -8 to + 8 volts at three temperatures, 977 ^{o}C, 993 ^{o}C and 1009 ^{o}C. This was among seven sets of data, which were not shown in this report. The chamber pressure was maintained at 1.5× 10^{-8} Torr. The emission current is consistently higher with a more negative bias voltage to the sample ($\mathbf{V_{B2}}$). Both the positive ion emission and negative electron emission increased when the temperature increased.

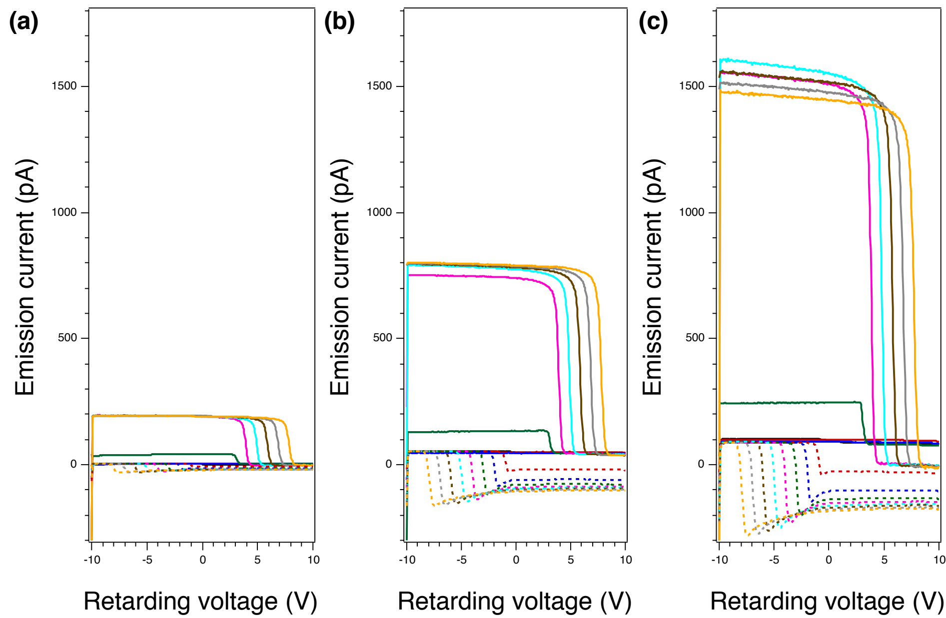

Figure 6.14 Emission current versus retarding voltage for sample PIP0B0C with V_{B2} = -8 to +8, V_H = V_B at (a) 977 ^oC, (b) 993 ^oC and (c) 1009 ^oC at 1.2×10^{-8} Torr.

From our previous experiment shown in **Figure 6.10(d)**, **(e)** and **(f)**, we learned that at the same temperature, despite the positive emission increasing with chamber pressure, the negative electron emission remained approximately the same. Extracting the emission current versus retarding voltage (**V_R**) at various temperatures, data for **V_{B2}** = -8 was shown in **Figure 6.15(a)** and data for **V_{B2}** = -4 was shown in **Figure 6.15(b)**.

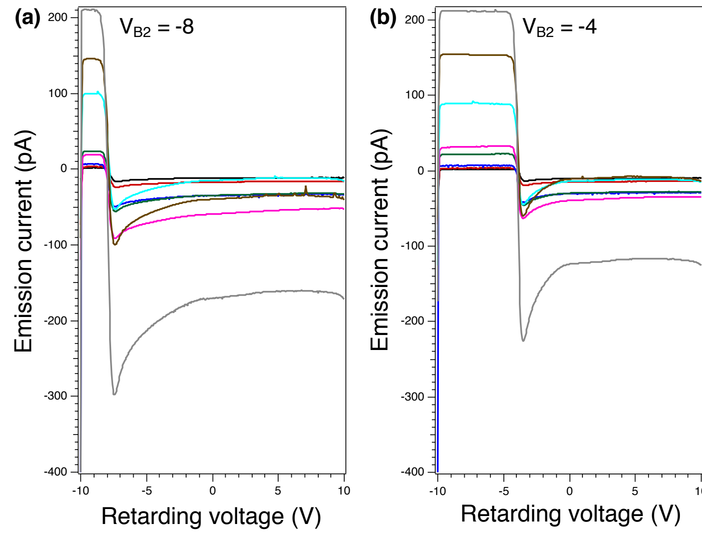

Figure 6.15(a) emission current versus retarding voltage at various temperature for V_{B2} = -8 and (b) emission current versus retarding voltage at various temperature for V_{B2} = -4.

Taking the difference between the upper plateau and lower plateau for the emission current unveils the number of electrons that carry enough kinetic energy to pass through the energy barrier from the retarding voltage. In **Figure 6.16(a)**, the extracted emission current was plotted with temperature for both $\mathbf{V_{B2}}$ = -8 and $\mathbf{V_{B2}}$ = -4; in **Figure 6.16(b)**, the same data were plotted in the form of Richardson-Dushman plot. [32] The slight difference may be attributed to reflection coefficients. There are two distinct types of reflective coefficients, one is defined as quantum mechanical reflection experienced by a charged particle in passing over a potential barrier, and the other is defined as the result of nonuniformity in the work function of the surface. [37] In the latter case, electrons with higher kinetic energy in the emission distribution pass through uniformly and the lowest-energy electrons originate only from the lowest work function surface. There is not disagreement between the two work function values: the work function deduced from data acquired when $\mathbf{V_{B2}}$ = -8 is 4.50 ± 0.15 eV and the work function deduced from data acquired when $\mathbf{V_{B2}}$ = -4 is 4.53 ± 0.13 eV. The work function calculated from the surface

electron emission suggests the surface is still predominantly covered with graphite, which has a work function reported to be 4.60 eV using a spectroscopic method. [70]

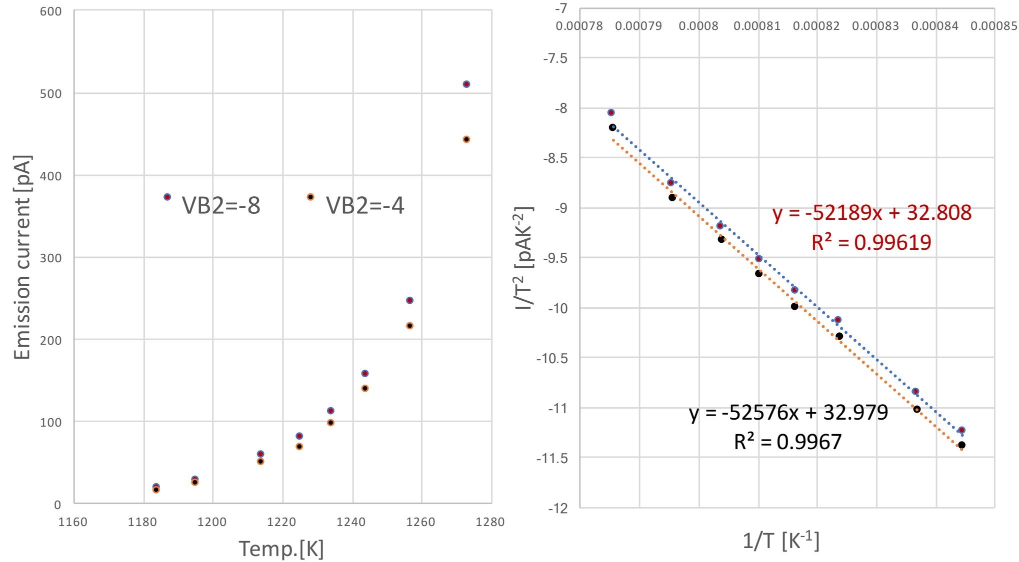

Figure 6.16(a) Emission current plotted with temperature (K) for sample PIPSiC0B1C with V_{B2} = -8 and -4; (b) Richardson-Dushman plot for (a).

The in-situ AES spectra for polymer-infiltration-pyrolysis (PIP) for elevated temperature were shown in **Figure 6.17**. As expected, the PIP specimen is considered carbon rich for all compositions. It was covered with graphitic carbon and after Ar sputtering, surface oxide layer was successfully removed. During the annealing process, from 850 to 1000 ^{o}C, the oxygen peak is completely removed and there is almost no change for both silicon *LVV* and carbon *KVV*. The AES composition analysis confirmed the finding from Richardson-Dushman plot that there is graphitic carbon layer dominating the surface.

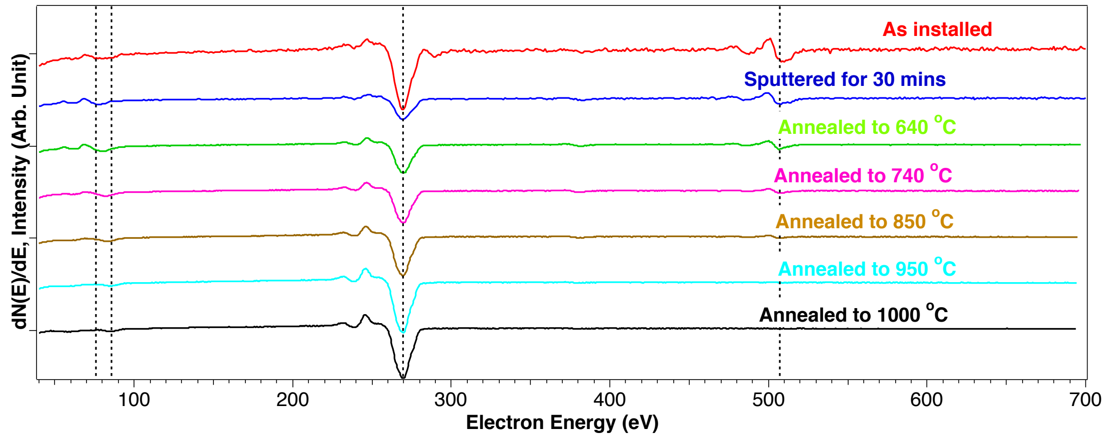

Figure 6.17 Auger spectra of the PIPSIC, red: as installed, blue: after Ar ion bombardment for 30 mins, green, pink, orange, light blue and black is acquired at 640 °C, 740 °C, 850 °C, 950 °C and 1000 oC, respectively.

6.2.5 Hot-pressed silicon carbide

An alternative fabrication process for polymer derived silicon carbide is the hot-pressed method. From the previous sections, Polymer-Infiltrated-Pyrolysis (PIP) provides conformal process and high porosity with 3C structure whereas the hot-pressed (HP) method provides a high relative density with mostly the 6H structure.

From the above observations, the surface composition does not vary within the temperature range in which we are going to acquire thermionic emission data. We examined the thermionic emission current versus retarding voltage for $\mathbf{V_{B2}}$ = -8 at the above temperature and plotted in **Figure 6.18(a)**. The abrupt current increase at around -8 volts can be attributed to thermionic emission from sample. In **Figure 6.18(b)**, emission current was plotted with respect to temperature and the Richardson plot was shown in **Figure 6.18 (c)**. The work function deduced from Richardson-Dushman equation is 4.82 ± 0.12 eV.

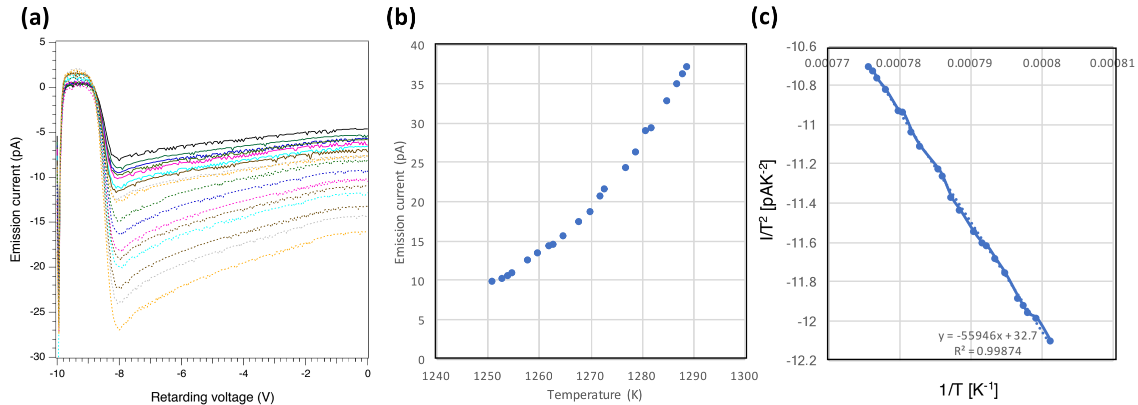

Figure 6.18 (a) Thermionic emission current versus retarding voltage for V_{B2} = -8 at the above temperature for HPSiC_1B1C; (b) emission current was plotted with respect to temperature and (c) the Richardson-Dushman plot.

To take advantage of in-situ AES capability, we first analyze the surface composition of the sample HPSiC1B1C. As shown in **Figure 6.19**, Auger spectra were acquired at the temperature labelled, after the sample was sputtered, annealed and sat at room temperature in vacuum overnight. With the temperature spanning from 835 ^{o}C to 1085 ^{o}C, there is no obvious change from spectrum to spectrum and we see the dominant carbon peak is graphitic as well.

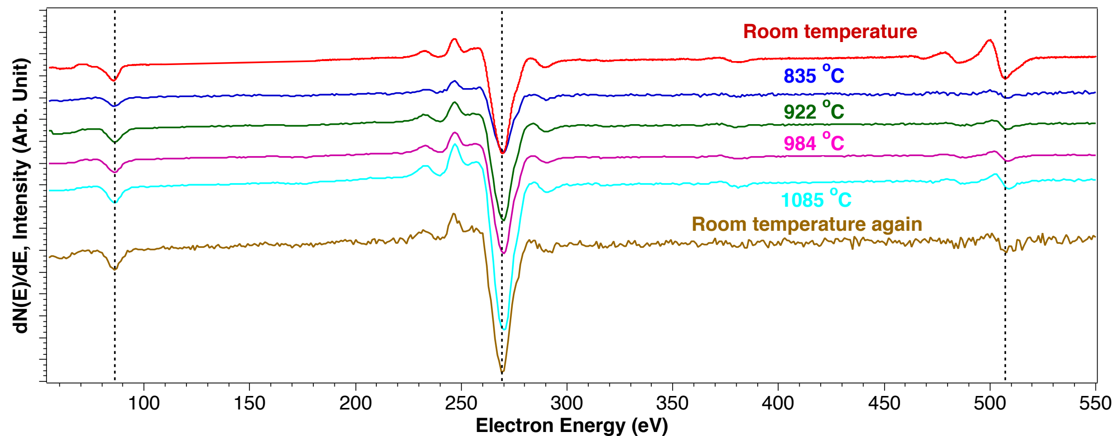

Figure 6.19 In-situ Auger spectra from a polycrystalline tungsten after the surface was sputtered by Ar ion and annealed at 1000 ^{o}C. The temperature labelled is the temperature when the spectra were acquired.

Although the heater is able to heat up sample to over 1000 ^{o}C, it is worth it to note that the chamber condition is not the best in terms of pumping efficiency and the chamber

pressure goes up drastically when input enormous amounts of heat. Thus, the suitable temperature ranges for thermionic emission data acquisition were limited to 1250 to 1290 K. At higher temperatures, the positive emission was collected and we believe that it affects the negative electron emission. We believe that this leads to underestimating the emission current in the higher temperature range.

6.3 Energy distribution of thermionic emitted electrons

The advantage of the in-direct heating for this versatile high vacuum chamber is not only the in-situ AES-TE surface analysis. With the modified LEED optics, the emitted current was collected with retarding grid, with which analyzing the energy distribution of the thermionic emitted electrons is possible. In this section, the thermionic emission energy distribution measured from tungsten, PIP silicon carbide and hot-pressed silicon carbide will be discussed separately. The effect of retarding voltage ($\mathbf{V_R}$) and bias voltage to specimen ($\mathbf{V_{B2}}$) will be addressed.

The typical emission spectrum (black) and its first derivative (red) versus retarding voltage are shown in **Figure 6.20.** The emission current was acquired from a PIP silicon carbide specimen with -8 volts of a bias voltage ($\mathbf{V_{B2}}$). Reading the black spectrum from left hand side, there is no electron collected from -10 volts, and the collector starts to pick up current about -8 volts, which is about the amount of the specimen's bias voltage ($\mathbf{V_{B2}}$). The blue dashed line indicates the on-set of the emission current, which indicates where the emitted electrons have enough kinetic energy to surpass the retarding voltage. Therefore, this on-set can be considered as the bottom of vacuum level.

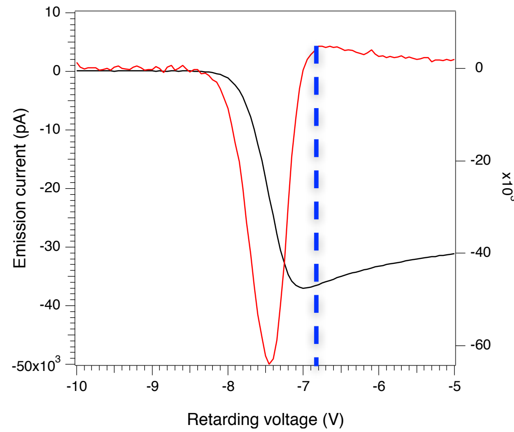

Figure 6.20 A typical thermionic emission versus retarding voltage spectrum and its first derivative with specimen bias voltage (V_{B2}) equals to 8 volts. Black: total current versus retarding voltage, red: the derivative of the total current versus retarding voltage.

6.3.1 The effect of specimen Bias Voltage (V_{B2}) to emission energy distribution

One advantage of this presented system is the ability to manipulate the emission from the specimen through adjusting the bias voltage to sample ($\mathbf{V_{B2}}$). However, due to the complexity of chamber environment, residual gas pressure and the induced emission from applied electric potential, it is necessary to look carefully into the effect that $\mathbf{V_{B2}}$ has on the emission energy distribution. The effects of space charge created from the applied bias voltage may alter the energy distribution of emitted electron.

Using a set of data partly shown in **Figure 6.14**, the emission current energy distribution (TEED) of PIP0C silicon carbide at 958, 968, 994 and 1009 ^{o}C with various $\mathbf{V_{B2}}$ is presented in **Figure 6.21**. It is worth noting that the TEED with 0 $\mathbf{V_{B2}}$ was also plotted in the figure in red, however, there is nothing but a noisy line around 0. Spectra from these four temperatures exhibited the same incremental shifting by about 1 volt. At the first glance, increasing $\mathbf{V_{B2}}$ resulted increasing the amplitude of the peaks for -1 volt to -4 volts and slightly decreasing the amplitude for -5 to -8 volts.

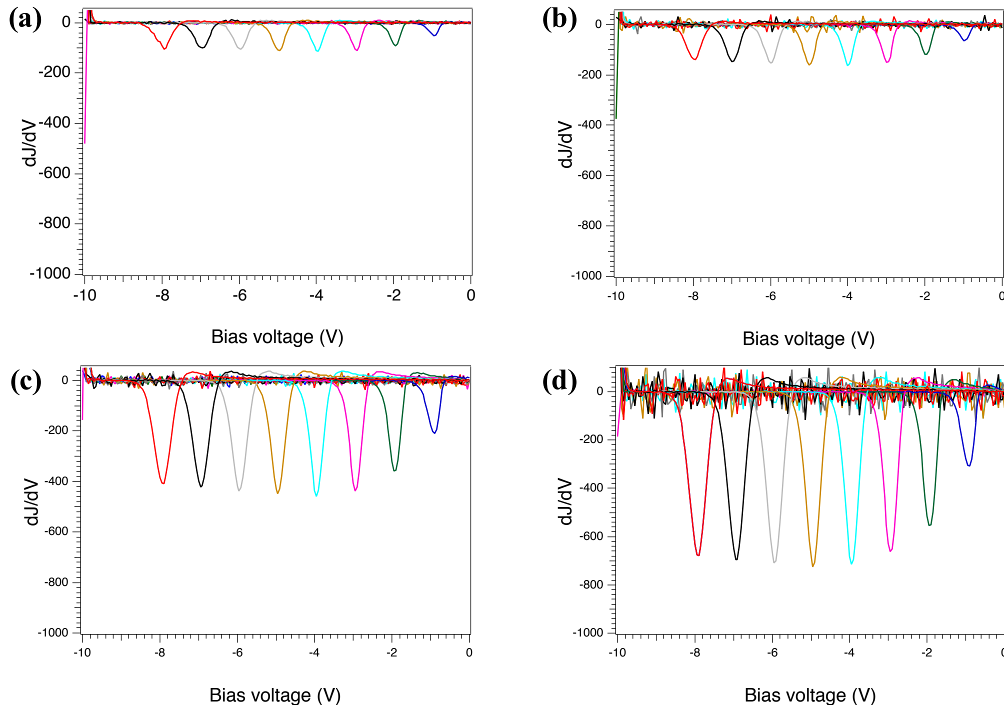

Figure 6.21 Thermionic emission energy distribution of PIP0C silicon carbide at (a) 958, (b) 968, (c) 994 and (d) 1009 ^{o}C with V_{B2} equals to -1, -2, -3, -4, -5, -6, -7, and -8 volts for blue, green, pink, light blue, brown, grey, black and red, respectively.

To better evaluate the effects of specimen bias voltage on the energy distribution spectra, we use the peak position and the full width half maximum (FWHM) as indicators for peak shift and peak broadening effect, respectively. In **Figure 6.22**, the peak positions were plotted with respect to temperature for different $\mathbf{V_{B2}}$. The peak positions vary within 30 meV for different $\mathbf{V_{B2}}$ at the same temperature while the error bar is around 100 meV. With the step size at 50 meV, it is safe to state that $\mathbf{V_{B2}}$ does not incur notable peak position shift. As for the FWHM, the summarized FWHM with respect to temperature for various $\mathbf{V_{B2}}$ is shown in **Figure 6.23**. As expected, the increasing of bias voltage incurred significant peak broadening at all temperatures measured. At a fixed $\mathbf{V_{B2}}$, there is a general trend that FWHM increases with respect to temperature.

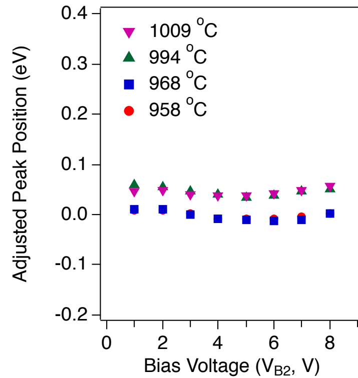

Figure 6.22 The peak positions of TEED with respect to sample bias voltage, with temperature at 958, 968, 994 and 1009 °C for red, blue, green and purple, respectively.

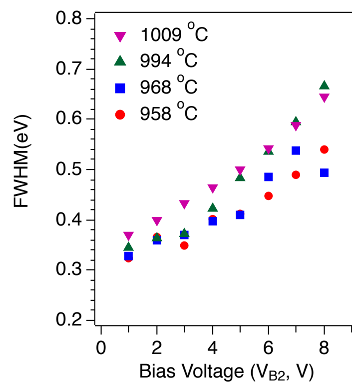

Figure 6.23 The FWHM of TEED with respect to V_{B2} for temperature equals to 958, 968, 994 and 1009 °C.

Since the FWHM seems to be flatten with the reduction of bias voltage, $\mathbf{V_{B2}}$, one may extrapolate the peak width around 0.3 eV for TEED without any bias voltage. The non-biased FWHM can be attributed to Fermi-Dirac distribution. However, it is not possible to acquire such data due to chamber environment. This is extraordinarily crucial for evaluating the "true" bandwidth of the emitted current since there is no current detectable without applying a sample bias voltage. On the other hand, the gradual increase of FWHM with respect to temperature under the same bias voltage represents shall be originated from the spreading of Fermi-Dirac distribution as the temperature increases.

6.3.2 Tungsten

Using planar polycrystalline tungsten as reference for calibration, work function extracted from a Richardson-Dushman plot varied from 4.35 ± 0.11 to 4.63 ± 0.02 eV depending on its heating history (as shown in **Figure 6.13(c))**. To address the issue of surface changes during heating, we examine this issue using the on-set of emission current energy distribution from tungsten. The AES for tungsten shown in **Figure 6.12** suggests there are carbon and oxygen species absorbed on the surface when the specimen has been at room temperature for extended period of time. This is confirmed by the retarded field analyzer (RFA) data, the derivative of emission current versus retarding voltage, as shown in **Figure 6.24**, it exhibits roughly 0.2 ± 0.05 eV shift. Since the step size of the retarding voltage is 0.1 volt, this shift is overlapping error bars with the Richardson –Dushman measurements. We utilize this correspondence to calibrate the Fermi level for our RFA apparatus.

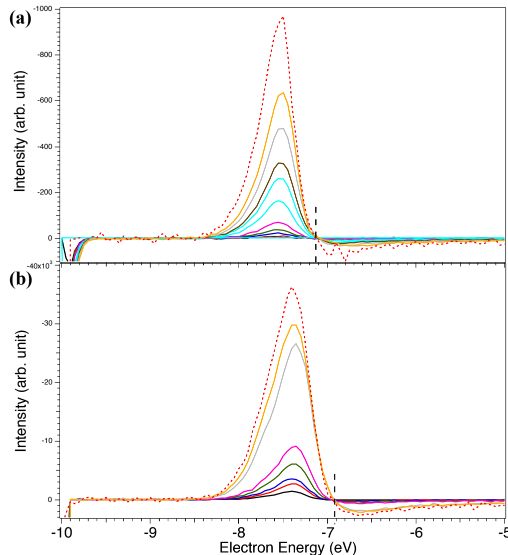

Figure 6.24 Energy distribution of emitted current from tungsten. (a) data was acquired while heating and (b) data was acquired during cooling. Chamber pressure is around 1×10^{-8} Torr.

Assuming the surface absorption is due to residual gas in the chamber, it may be affected by chamber pressure. The thermionic emission is still affected by the residue gas absorption at chamber pressure around 1×10^{-8} Torr. It would be interesting to know the limit of this experimental chamber. For this, a set of data were taken at chamber pressure around 1×10^{-7} Torr. The energy distribution of thermionic emitted electrons was shown in **Figure 6.25**. In **Figure 6.25(b)**, the spectra were normalized to the same height.

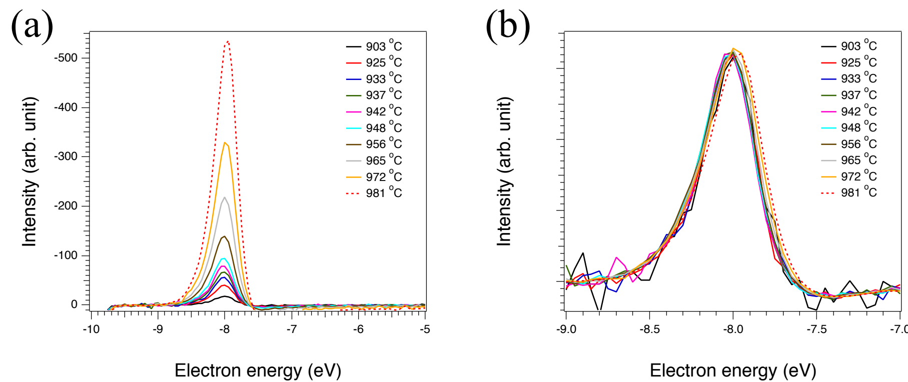

Figure 6.25 Energy distribution of emitted current from tungsten at chamber pressure around 1×10^{-7} Torr.

With low vacuum condition (1×10^{-7} Torr), the amount of residual gas is dominating the surface and therefore, its energy distribution is uniform after it is normalized. From the electron energy distribution spectra, the on-set shifted from -7.2 eV (from the heated tungsten) to -7.6 eV, surprisingly. This suggests that the work function increased and it is more difficult for electrons to leave the material's surface. Since the spectra were affected dramatically by the residual gas in the chamber, we'll only discuss the data taken when the chamber pressure is below 1×10^{-8} Torr.

6.3.3 PIP vs HP

As shown in **Figure 6.15**, the intensity of the emission current seems to increase by 10 percent over the sample bias voltage (**V_{B2}**) range -4 to -8 volts. The normalized

thermionic emission energy distribution (TEED) versus electron energy is shown in **Figure 6.26(a)** and **(c)** for TEED acquired from the hot-pressed specimen with 11 percent excess carbon (**HP11C**) with $\mathbf{V_{B2}}$ equals -4 and -8 and **(b)** and **(d)** for TEED acquired from the PIP specimen with 17 percent excess carbon (**PIP17C**) with $\mathbf{V_{B2}}$ equals -4 and -8, respectively.

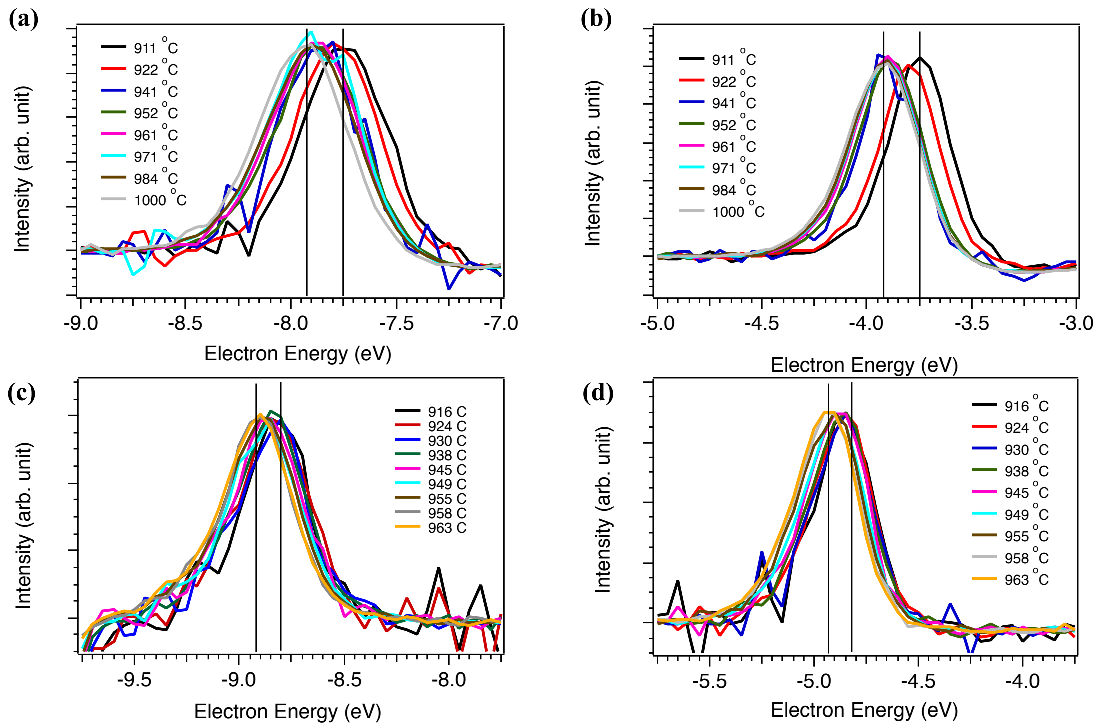

Figure 6.26 Normalized TEED acquired from HPSiC for (a) $\mathbf{V_{B2}}$ equals -4 volts and (c) $\mathbf{V_{B2}}$ equals -8 volts; normalized TEED acquired from PIPSiC for (b) $\mathbf{V_{B2}}$ equals -4 volts and (d) $\mathbf{V_{B2}}$ equals -8 volts.

Qualitatively, we notice there is a distinct shift toward higher energy (more negative) from the lowest emission temperature (~900 ^{o}C) to the highest emission temperature (~1000 ^{o}C) of about 0.175 eV and 0.1 eV for the PIPSiC and HPSiC specimens, respectively. Comparing the left ($\mathbf{V_{B2}}$ = -8 V) and the right ($\mathbf{V_{B2}}$ = -4 V) shows an increase FWHM at higher bias voltage, as previously observed for PIPSiC (**Figure 6.23**). Be specific. The small shift to higher work function with increasing

temperature was independent of bias voltage. Lastly, through combining the calibrated value for the W Fermi energy and with the vacuum level obtained from the high energy onset for the SiC samples, we can deduce their work function to compare with the result from the Richardson-Dushman plot. This is described below.

6.4 Detailed procedure and interpretation for TEED spectra

We take advantage of thermionic emission to reveal the material high temperature surface properties. While emission currents from different specimens were not measured at the same time, specimens were biased with known bias voltage ($\mathbf{V_{B2}}$) and thus the onset energy can be compared using an well-studied material, tungsten. To know the relative energy level between the specimen and collector while the collector work function is unknown, an internal calibration is needed. From the previous chapter, the tungsten work function calculated from the thermionic emission Richardson-Dushman equation has been identified. Since the on-set of the energy distribution in the retarding spectrum represents the bottom of vacuum level, the Fermi level can be calculated from the work function as the energy difference between the Fermi level and vacuum level.

For the ease of understanding, a very detailed description and visualization are shown in **Figure 6.27**. **Figure 6.27 (a)** is one set of thermionic emission energy distribution (TEED) spectra versus retarding voltage at various temperature as sample bias voltage $\mathbf{V_{B2}}$ = -8 volt. The spectra were shifted by 8 volts to compensate for the specimen bias voltage, $\mathbf{V_{B2}}$, shown in **Figure 6.27 (b)**. Because electrons carry negative charge, the energy of detected electron in electron volts (1.6×10^{-19} J) can be multiplying the retarding voltage by -1, which is shown in **Figure 6.27 (c)**. Lastly, using the work

function deduced from Richardson-Dushman plot, Φ = 4.36 eV. We can identify a new zero as the Fermi level by shifting the data so the vacuum-level onset appears at 4.36 eV. This required the data to be shifted by 5.35 eV (shown in **Figure 6.27 (d)**), which we identify as the work function of the detector. Assuming this remains constant, we use the same value to adjust silicon carbide spectra. This internal adjusting constant will be applied to the data sets from the PIP and HP silicon carbide.

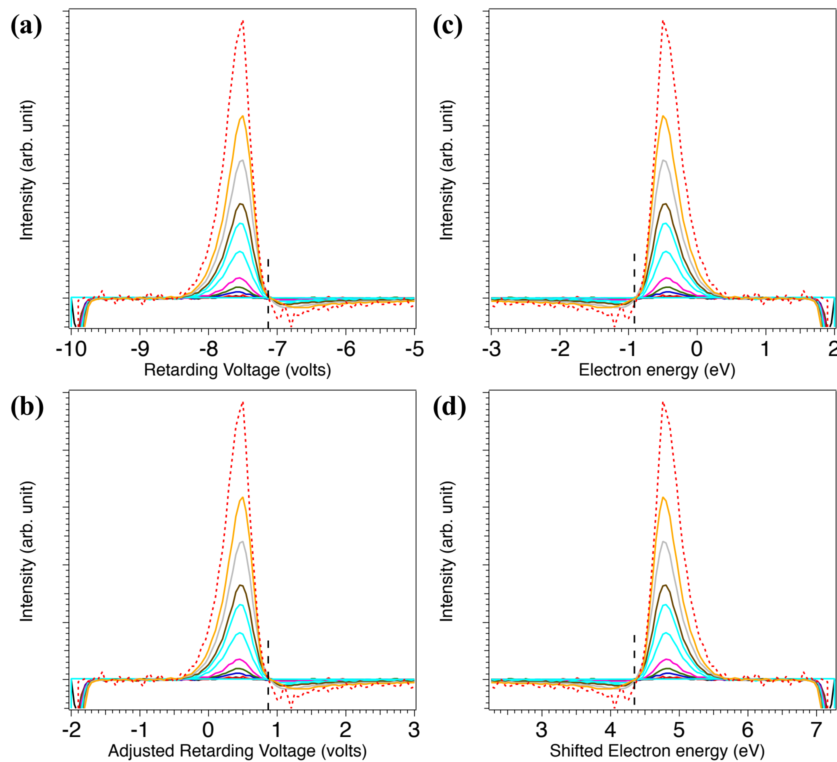

Figure 6.27 (a) Emission spectra versus retarding voltage for tungsten from various temperature, (b) adjust the retarding voltage by 8 volts to compensate specimen bias voltage (V_{B2}), (c) x-axis multiply by -1 so it's showing electron energy instead of retarding voltage, and (d) set the fermi energy to zero using work function deduced from RD plot for tungsten and the on-set energy to 4.36 eV.

As shown in **Figure 6.28**, TEED spectra for tungsten were shifted and flipped so the on-set energy matches its measured Richardson-Dushman work function, 4.36 eV. Applying the same procedure to TEED spectra acquired from PIP0C and HP1B1C silicon carbide, we identify the vacuum level for these materials relative to the Fermi level, i.e., the work function. The two-species exhibited different on-set energies found with the Richardson-Dushman work function. TEED spectra for PIP0C silicon carbide suggests the on-set energy is about identical to the work function extracted from its Richardson-Dushman plot; however, TEED spectra for HP1B1C silicon carbide's on-set energy is about 1 eV off from the Richardson-Dushman work function.

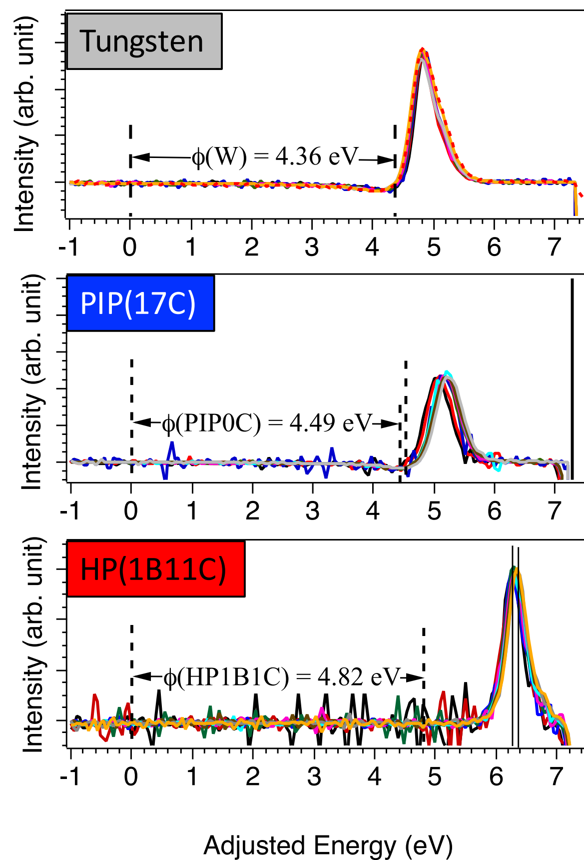

Figure 6.28 Adjusted TEED spectra for tungsten (top), PIP0C silicon carbide (middle) and HP silicon carbide (bottom). The energy was adjusted for tungsten on-set energy as 4.36 eV for all three figures.

Intuitively, this unexpected discrepancy suggests that the majority of charge carrier came from deeper energy bands instead of the energy bands close to the Fermi level. This would be the case if a semiconductor becomes intrinsic at high temperature, and the charge carriers were all excited. Under these circumstances, the Fermi level moves toward mid-gap, and the excited charge carriers should come from the valence band. This may explain the difference of ~1 eV between Φ_{RD} and on-set energy. However, it is more likely that the Richardson-Dushman theory assumptions are not valid for the semiconductors, which the Fermi level is within the gap. The TEED measurements indicate that E_f is in mid-gap (the vacuum level is tied to where the band edges are), and thus, the Richardson-Dushman assumptions are not valid.

Chapter 7 Conclusion

In the presented dissertation, the author emphasizes the issue of finding electronic materials for high temperature application with three aspects: a novel process of making high temperature electrical materials utilizing a polymer precursor, a custom designed measuring instrument for high temperature electrical resistivity due to the lack of conventional instruments, and thermionic emission behavior coupled with in-situ Auger electron spectroscopy to study material properties at high temperatures. Along the course of research, there are two specific processes of fabrication, hot-pressed (HP) and polymer-infiltration-pyrolysis (PIP) developed. As novel processing methods, silicon carbide samples fabricated from these two methods are examined and analyzed with various techniques.

7.1 Development of HP and PIP method for polymer derived silicon carbide synthesis and the properties of the resulting samples

The polymer derived ceramic (PDC) process opens the possibility for conformal fabrication and the ability to adjust electrical resistivity through tailoring its compositions. With the PDC process, specific specimens were fabricated through two material forming routes, polymer infiltration pyrolysis (PIP) and hot pressed (HP). The crystal structure of resulting specimens depends on the process: with the relatively low temperature PIP process (1700 ^{o}C), low relative density 3C polytype was with significant excess carbon; high temperature HP process (2130 ^{o}C) yields a majority of 6H polytype with over 90% relative density and less excess carbon incorporated from the precursor.

The compositional analysis compositional analysis by X-ray photoelectron spectroscopy (XPS), glow discharge optical emission spectroscopy (GDOES), silicon nuclear magnetic resonance (^{29}Si NMR), microscopic Raman spectroscopy and in-situ Auger electron spectroscopy (AES) were carried out. XPS only analyzes a thin layer and the surface is easily oxidized so it is not ideal for characterizing the materials. ^{29}Si NMR probes bulk silicon chemical state and it suggested there is no oxide formation in the bulk. Observed using Raman spectroscopy, specimens through PIP route exhibit SiC/C core covered with a graphite shell; specimens fabricated through HP route exhibit better intermixed SiC/C and there is no domination of either SiC or graphite found in the top micron from Raman spectroscopy. AES also probes surface elemental information and it could be useful confirming the surface compositions while doing thermionic emission experiments. Lastly, GDOES sputtered into several micro meters and it provides compositional insight for silicon to carbon ratio. In general, there is excess carbon detected from GDOES for samples fabricated from both HP and PIP methods with considerably more from the PIP process. The excess can be attributed to the intrinsic excess carbon from the polymer. The surface carbon enrichment observed from PIP samples through Raman spectroscopy is an indication of a different reactivity for polymer forming agent (AHPCS) and excess carbon additive (divinyl benzene) in the infiltration process, which involves repeated exposure to the polymer precursors.

Despite the ability to adjust the compositions, the corresponding electrical conductivity does not completely reflect the relative composition of excess carbon. From the examined specimens with excess carbon from 11% to 50%, the electrical resistivity asymptotically reaches about 0.1 Ωcm at 1500 ^{o}C for specimens fabricated through both

PIP and HP methods. However, the majority of the specimens reported in the dissertation exhibit moderate electrical conductivity and have met the resistivity requirement of < 2 Ωcm above 1500 ^{o}C for MHD application.

7.2 Proposed energy band structure for polymer derived silicon carbide

There were TEED spectra acquired from three different species presented; one is the well studied polycrystalline tungsten metal and the other two are novel materials which consist mainly of silicon carbide and graphite. Throughout the thesis, the structural characteristics of these two materials were identified. Despite its apparent structure from XRD information, both were covered with graphite layers at room temperature which depended on the amount of carbon additive. Upon heating, growth of graphite layers was observed from both HP and PIP silicon carbide specimens from in-situ AES.

Based on this information, the following summary could be made. A simplified band diagram for tungsten, **PIP0C** SiC and **HP1B1C** SiC were proposed in **Figure 7.1**. The free electron theory for thermionic emission [68] best fit the metal materials. Thus, the Φ_{RD} matched with literature value and we are confident in using it as an internal standard. Also due to its metallic behavior, the location of on-set energy barely changes. For PIP0C silicon carbide, after the course of data acquisition, we have identified graphitic carbon from our in-situ AES results. And thus, the Φ_{RD} for PIP0C silicon carbide specimens matched well with the location of on-set from TEED spectra. The slight temperature dependence indicates shifting of Fermi level. As such, we say it has a metal-like band diagram. Lastly, the Φ_{RD} for HP1B1C silicon carbide specimen does not match with the location of on-set energy from TEED spectra. In our in-situ AES, it

appears that **HP1B1C** although covered with graphitic carbon, there is still silicon and carbidic carbon signal shown on AES. As such, the total emission, which governs the Richardson-Dushman equation, suggests work function close to graphite; TEED spectra consider the number of charges in the dopant states and turned out to be ionization energy-like and the Fermi energy is somewhere in the band gap.

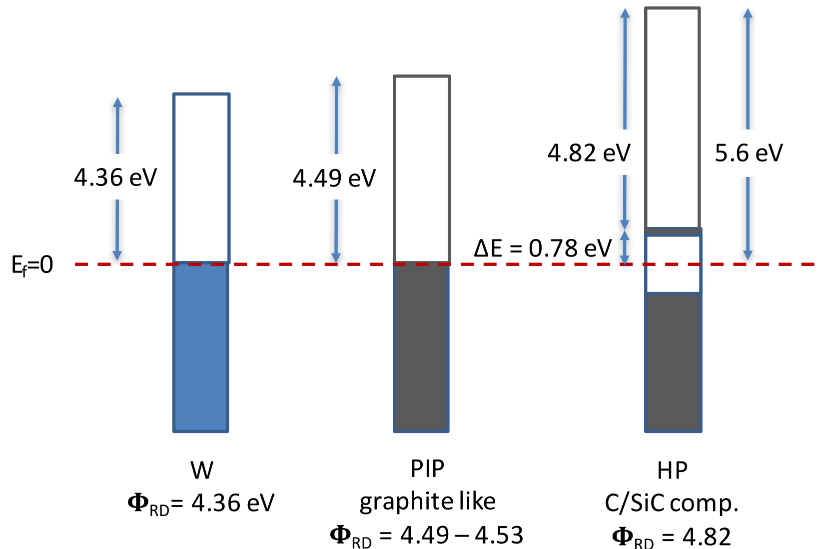

Figure 7.1 Simplified band diagram for tungsten, PIP0C silicon carbide and HP1B1C silicon carbide.

In conclusion, the presented data provide strong evidence that the presented procedures can not only probe thermionic emission Richardson-Dushman work function, through internal calibration using known materials, it is capable of researching materials for high temperature applications.

To study a material's high temperature surface properties and decipher its high temperature electrical resistivity, in-situ Auger electron spectroscopy (AES) coupled with a thermionic emission energy distribution (TEED) technique provides insight for a materials high temperature behavior. From in-situ AES, the material surface compositions at high temperature can be observed. There are three categories of materials

reported: polycrystalline tungsten plate, hot-pressed silicon carbide and polymer-infiltration-pyrolysis silicon carbide. In-situ AES for tungsten suggested that carbon monoxide adsorbent from residual gas in the vacuum chamber affected the composition. After measuring the surface work function utilizing thermionic emission, it also agreed with the finding from in-situ AES. Silicon carbide specimens fabricated from both HP and PIP process undergo graphitization during the heating process. A unique technique of biasing both the sample and the heating element unveiled the surface work function by measuring the energy difference between the Fermi level and vacuum level. This work function measurement method is faster than the well-known Richardson Dushman method and it is capable of performing measurements at one temperature. Moreover, being a metallic conductor is not necessary for this method to be applied.

With the gathered information, the polymer derived silicon carbide / graphite composite materials may be a promising candidate material for direct energy extraction applications.

7.3 Areas of future work

The results presented in the dissertation provides a set of material exploratory researches in which the materials for high temperature electric applications may be achieved. In the unique high temperature application regions, unconventional instruments are in general needed. Therefore, in the concluding section, the area of future research will be briefly described.

There are two parts of this dissertation, the first part emphasized the development of unique modularized experimental apparatus. Because of the modulation nature of

customized experimental apparatus, the author's developments including in-situ AES and TE/TEED and electrical conductivity measurement apparatus can be easily adopted for any material. For the second part, the author addressed the inconsistence of work function deduced from Richardson-Dushman equation and the on-set energy from TEED spectra. This opens an avenue for high temperature electrical property study for semiconductor. The work function at elevated temperature can be estimated as a function of temperature while the surface composition can be probed in-situ at the same time. Furthermore, the versatile UHV chamber is capable for valance band study using XPS and convoluted conduction band study using energy loss spectroscopy (ELS). With that said, a grand picture of materials surface properties and its electrical structure at elevated temperature. The success of such work may be expanded so as to explore the potential of other high temperature materials for electrical applications.

Appendix 1. Spectroscopic Two-Color Pyrometry

Temperature measurement is crucial for high temperature experiment. There are two catalogues, contact measurement such as thermocouples and non-contact measurement such as pyrometer. There are many restriction using thermocouple for thermionic emission and other MHD involve experiments because the wary of contaminations. Non-contact measurement method has gotten the advantage for precise spatial measurement, fast response and clean measurement.

In the presented research, we utilized a single wavelength pyrometer and assuming the emissivity of materials is a fix value (0.9) for silicon carbide and 0.95 for graphite. It is generally true but it may not be precise while self-replenish graphite layer grown on the surface at elevated temperature. The measurement of radiation is also limited with the detector wavelength. Practically, it is difficult to determine the spectral emissivity as a function of temperature of materials. As such reason, a universal remote temperature sensing technique is needed.

A1.1 Principle of the method:

Temperature measurements can be divided into two categories, contact methods and non-contact methods. Contact methods provide excellent accuracy at defined temperature region in different environments. One example is thermocouple (TC), which is consisting of two metal alloys forming electrical junctions at different temperature. A thermocouple produces temperature dependent voltage as a result of thermoelectric effect.

However, each thermocouple has its own limitations. For example, tungsten / rhenium alloy thermocouples (type C, type D and type G) is the highest graded temperature and it can measure temperature from 0 °C to 2315 °C. However, tungsten tends to oxidize and it is only practical to use it in vacuum or inert gas environments. On the other hand, platinum / rhodium alloy thermocouples (type B, type R, and type S) are great for severe oxidation, but it can only measure up to 1600 °C.

Non-contact temperature measurements are ideal for MHD applications. Convenient mono-wavelength non-contact pyrometry utilizes Plank's law for thermal radiation. The knowledge of spectral emissivity at the desired temperature range is necessary. However, the spectral emissivity at the temperature region itself is unknown to the scientific community. On the other hand, two-color-pyrometry assumes the emissivity at two wavelengths is identical and by taking the ratio of irradiation at two wavelengths, temperature can be determined. [71]

A black body thermal radiation at absolute temperature T can be described as following:

$$B_\lambda(\lambda, T) = \frac{2hc^2}{\lambda^5} \frac{1}{e^{\frac{hc}{\lambda k_B T}} - 1} \qquad \text{Eq.1}$$

where λ is the wavelength, k_B is the Boltzmann constant, h is Planck constant, c is the speed of light according to Planck's law. There are not many cases that real materials emit radiation energy as true black body. The real materials thermal radiation can be described as:

$$B_{real} = B_{black} \cdot \varepsilon(\lambda, T) \quad \text{Eq.2}$$

where *ε(λ,T)* is the emissivity of the material. The emissivity is a function of wavelength, temperature and surface condition. For the purpose of discussion, one can assume the surface has been polished and the surface condition can be ruled out.

$$B_{real}(\lambda, T) = \frac{2hc^2}{\lambda^5} \frac{1}{e^{\frac{hc}{\lambda k_B T}-1}} \cdot \varepsilon(\lambda, T) \quad \text{Eq.3}$$

At Wien's condition, $\frac{hc}{\lambda k_B T} \gg 1$, we can obtain the following expression:

$$\ln(B_{real}\lambda^5) - \ln(\varepsilon hc^2) = -\frac{hc}{k_B} \cdot \frac{1}{\lambda T} \quad \text{Eq.4}$$

One can take two irradiation data from two wavelengths, and the Two-Color temperature can be described as

$$T_{two-color} = \frac{-\frac{hc}{k_B}(\frac{1}{\lambda_1} - \frac{1}{\lambda_2})}{\ln(\lambda_1{}^5 B_{\lambda 1} - \lambda_2{}^5 B_{\lambda 2})} \quad \text{Eq.5}$$

It is worth to note that it is under the assumption of Wien's condition. As a result, this relation only holds when $\lambda \cdot T_m < 3669.7\ \mu m \cdot K$. [72]

To verify this relationship, one can plot the spectral irradiation (spectral intensity, kJ/sr nm m^2) verse wavelength according to previously described Planck's law and plug in the spectral intensity into the equation for two-color temperature. In **Figure A.**, left is the theoretical intensity verse wavelength according to Planck's law at temperature from 1000 K to 5000 K in 500 k spacing; right is the calculated two-color temperature generated from the wavelength plus minus 5 nm. It is clear that the method holds well at short wavelength (below 500 nm) for all plotted temperature (1000 to 5000 K), however there is a big discrepancy at longer wavelength for higher temperature range. In the MHD

application, the propulsion jet is around 3000 K at the edge of the barrow and it quickly cools down as it expands and propagates according to the theoretical calculation.

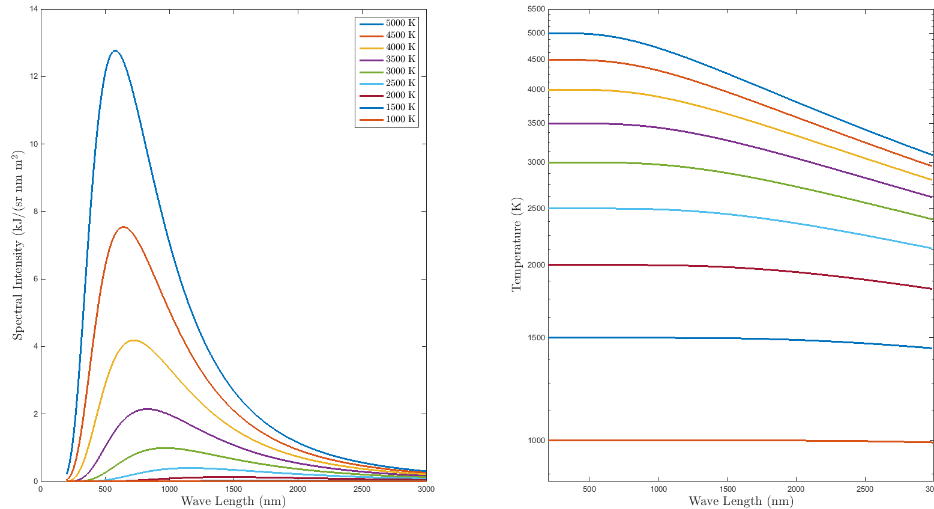

Figure A.1. Left figure is the spectral intensity verse wavelength generated from Planck's law; the right figure is the two-color temperature calculated from the above equation.

Two-color pyrometer is available and it is widely adopted in industrial application for targets with known spectral emissivity at the desired temperature range. The other restriction to this method is that it assumes uniform irradiation. For a target with non-uniform temperature, the irradiation contributed from different temperatures differs and the wavelength information is required for this application. Hence, we came up with this multiple-two-color pyrometry.

In our experiment setup, we utilize a miniature UV-VIS spectrometer to collect the thermal radiation. We design a LabVIEW program that is able to convert radiation to two-color temperature according to previous mentioned. Since there are over thousands of pixels for the CCD detector in the spectrometer, we get thousands of data points for two-color temperature with their wavelength dependency.

An alternative way to estimate from the Wien's displacement law, which is also derived from Planck's law. It describes that the spectral radiance of black body radiation per unit wavelength, peaks at the wavelength λ_{max} given by

$$\lambda_{max} = \frac{b}{T} \quad \text{Eq.6}$$

where T is temperature in Kelvin, and b is Wien's displacement constant, equals to 2.8978×10^{-3} (m• K^{-1}). This can also be achieved once the peak irradiance falls into the spectrometer detection range. With the above-mentioned two methods, the emissivity as a function of wavelength and temperature can also be calculated.

A1.2 Instruments:

UV-VIS spectrometer, wavelength ranges from 250 nm to 850 nm, Flame-S, Ocean Optics Inc.

Mercury – argon light source, SL Mercury Argon, StellarNet Inc.

Tungsten-halogen calibration light source, HL-2000-CAL-EXT, Ocean Optics Inc.)

Fiber optics cable, 600 um, Ocean Optics Inc.

Omnidriver + SPAM software development kit (SDK), Ocean Optics Inc.

LabVIEW, National Instruments

Black body radiator, Regasus R Model 970, Isothermal Technology Limited.

A1.3 Procedure:

A1.3.1 Calibration

Calibration is one of the most important steps amount the development of this measurement method.

There are two parts of calibration, the wavelength calibration and the intensity calibration. The wavelength calibration is very straightforward comparing to the intensity calibration. The wavelength calibration can be achieved with the mercury – argon light source. The source we used is SL2 mercury – argon, which provides emission line from 253.65 nm to 1013.98 nm. Once calibrated, the wavelength reading remains precise for a long time.

On the other hand, intensity / irradiation calibration is not that straightforward. In this activity, a halogen tungsten light source provides a well-defined absolute irradiance to calibrate the intensity. After taking the spectrum from calibration light source, a wavelength dependent calibration coefficient can be reduced. Ideally, the CCD detector should response linearly to its integration time. It is not the case for the spectrometer we use here. We need to generate calibration coefficient for the integration time we choose.

Lastly, the dark spectrum needs to be adjusted. The CCD detector outputs a small reading / noise constantly regardless the irradiation it takes. This drastically affected the two-color temperature results. Fortunately, upon observation, the noise remains a constant value regardless other spectrometer parameters. This can be adjusted by subtracting the intensity spectrum with the average counts between 200 nm to 250 nm (there should not be any irradiation at that wavelength range).

A1.3.2 Data smoothing

There are two limitations using the miniature spectrometer despite all the advantages, one is the dynamic range of the CCD detector and the other is very low response above 750 nm. The reason for the later is intrinsic to the bandgap of Si semiconductor. As for the dynamic range, since the irradiation is proportional to T^4, it is very easy to saturate the detector. As a result, it is necessary to both shorten the integration time and narrow the field of view. When the integration time is shorten, the signal to noise ratio decreases. In order to improve the data quality and to get rid of the noise that is intrinsic to a particular pixel, two improvements have been done.

First, we introduced an averaging method. For the irradiance B_1 to B_5 at λ_1 to λ_5, B_3' = Average(B_1:B_5) This method can reduce noise bound to the specific pixel. Secondly, we did a series of narrow range polynomial fitting to the irradiance. Each spectrum is divided into ~50 fragments, and each fragment contains roughly 10 nm wavelength range. Within this narrow range, the real irradiance spectrum is simple enough to be fitted with polynomial fitting. The fitted spectrum from each fragment is then recombined to new spectrum. This provides much better data quality than repeating and averaging over a hundred scans without lagging the program.

A1.4 Results:

A1.4.1 System verification with black body radiator

In order to verify the system, a black body radiator (a 1200 ^{o}C furnace with a graphite black body target) is used to provide thermal radiation. After reaching the desired temperature, the black body radiator was sat for another 15 mins for better

temperature homogeneity. After reaching the temperature, we used optical fiber to collect the thermal radiation. The integration time for acquiring the spectra varies in order to get ~ 80% counts for the CCD detector. For the temperature below 1300 K, the thermal radiation is very week and it took over 10 sec to acquire the spectrum. At this temperature range, it is evident to choose a contact method (such as thermal couple) over the spectroscopic method. Above 1300 K, a thermal radiation spectrum can be acquired with in 3 sec. The acquisition time reduced significantly as the temperature increased.

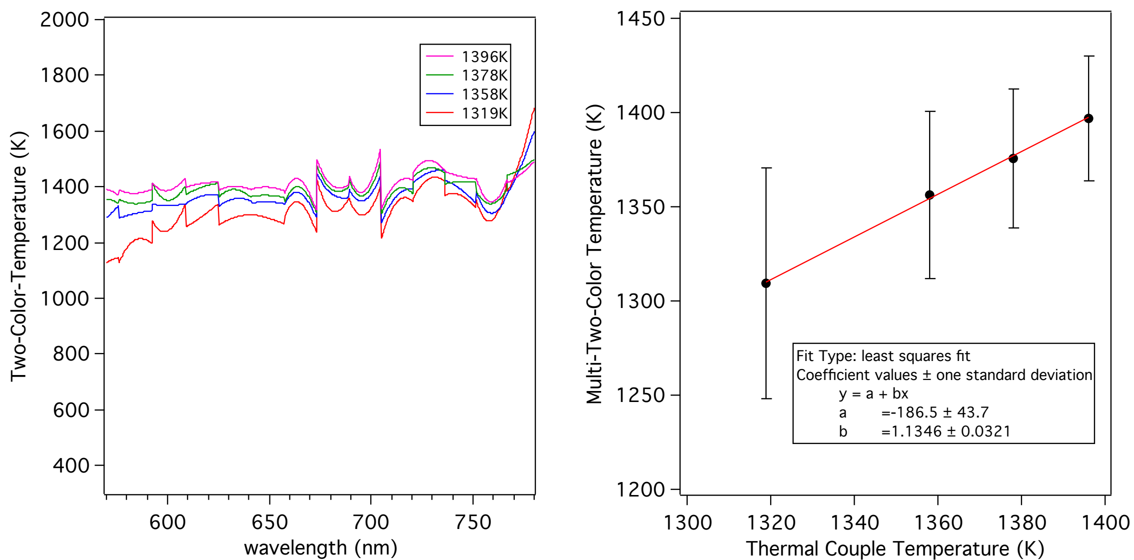

Figure A.2 Two-Color-Temperature reading from black body radiator. Left: X-axis is the average wavelength (± 15 nm) used to calculate Two-Color-Temperature and Y-axis is the calculated Two-Color-Temperature. Right: X-axis is the thermal couple temperature reading and Y-axis is the average of Two-Color-Temperature with the standard deviation as the error bar.

As shown in **Figure A.** (left), every point represents the result calculated from Eq.5 using the irradiance at indicated wavelength plus and minus 15 nm. It represented the thermal radiation collected from the optical fiber. As the current setup, the field of view is larger than the hot zone. As a result, it was collecting thermal radiation from both hot spot and the cooler surrounding. At shorter wavelength, there is almost no influence from lower temperature surrounding because the radiation is too low to be detected. In

contrast, the peak of thermal radiation shifts to longer wavelength as the temperature decreases and thus it tends to contribute more to the measured spectrum. By looking at the multiple two-color-temperature around 750-780 nm, an artificial takeoff is observed. That may be contributed from the lower temperature surrounding and creates this false temperature increase. The magnitude of the artificial takeoff is less significant for higher temperature since the intensity of desired radiation is much stronger then the cooler surrounding.

We only chose the data between 550 nm to 780 nm because the counts below 550 nm are simply too low and there is no meaningful data can be shown. Above 780 nm, there are too little counts from the CCD and it also creates some artificial reading. As shown in **Figure A.** (right), we can see the average of the multiple Two-Color-Temperature is very close to the thermal couple reading. The standard deviation of the results is about 61 for 1319K and 33 for 1396K. One can optimistic think as the temperature increase, the standard deviation may further reduce. However, the standard deviation is not most indicative in this measurement because each point represents an individual measurement. The knowledge behind to carefully choose the wavelength range is the most important factor.

A1.4.2 Demonstration using MgO specimen toward MHD combustion torch

To demonstrate this technology, a one-inch diameter MgO specimen was used as a temperature probe. The emissivity of the flame is usually below 0.1 and the emissivity of solid material is usually above 0.8. This difference gives us an advantage to only look at the much brighter materials. The melting point of MgO is about 2852 ^{o}C (3125 K). The

specimen was core drilled from an MgO brick without further treatment. The sample was installed on a linear slide whereas the optical fiber was installed on a holder, which is 4 inch away from the gun center.

The spectral integration time was set to 10 msec to avoid detector saturation. It takes about 1 sec integration time to get the spectrum from the torch. Upon test, the sample started to approach the gun center from one-inch distance. The sample moved 0.1 inch per step and waited for 5 mins before moved to next spot. When the distance shorter than 0.3 inch, we changed to 0.02 inch per step. There was no readable signal until 0.26 inch distance. We did not move further than 0.16 inch for this demonstration.

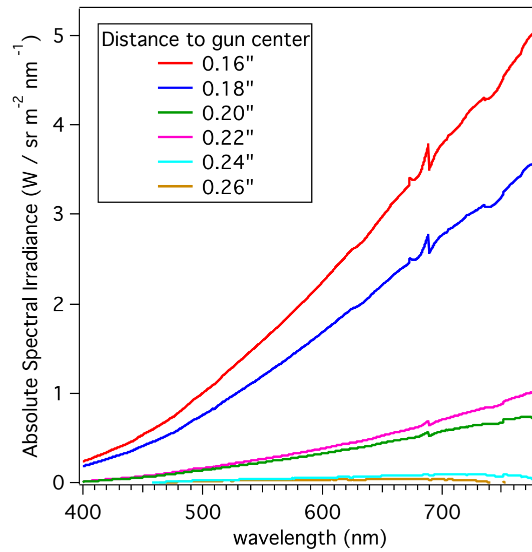

Figure A.3 Absolute spectral irradiance converted from the OceanOptics miniature spectrometer. The intensity can be grouped to three catalogues. The irradiance for distance above 0.24 inch is extremely low; the irradiance for distance between 0.22" to 0.2" is medium; the irradiance for distance below 0.18" increase drastically.

As shown in **Figure A.**, we can group the distance into three catalogues. While the distance is too far, it is essentially the torch irradiance because the sample is not hot enough. While the distance is close enough (0.16" to 0.18"), the sample surface is hot

enough and irradiance is much higher than the torch. As for the medium distance, the irradiance is the combination of the two, and thus, the reading may be misleading.

As shown in **Figure A.** (left), we are able to calculate the temperatures for four spots, from 2650 K to 2800 K. As we notice there is an unusual wiggles around 690 nm, we omitted the range and only calculate from 500 nm to 650 nm. The results were summarized in Figure A. (right). The temperature readings are flatted for distance of 0.16” and 0.18” and they varied a lot for 0.20” and 0.22”. The standard deviation is from 53.8 to 93.5 for these four distance.

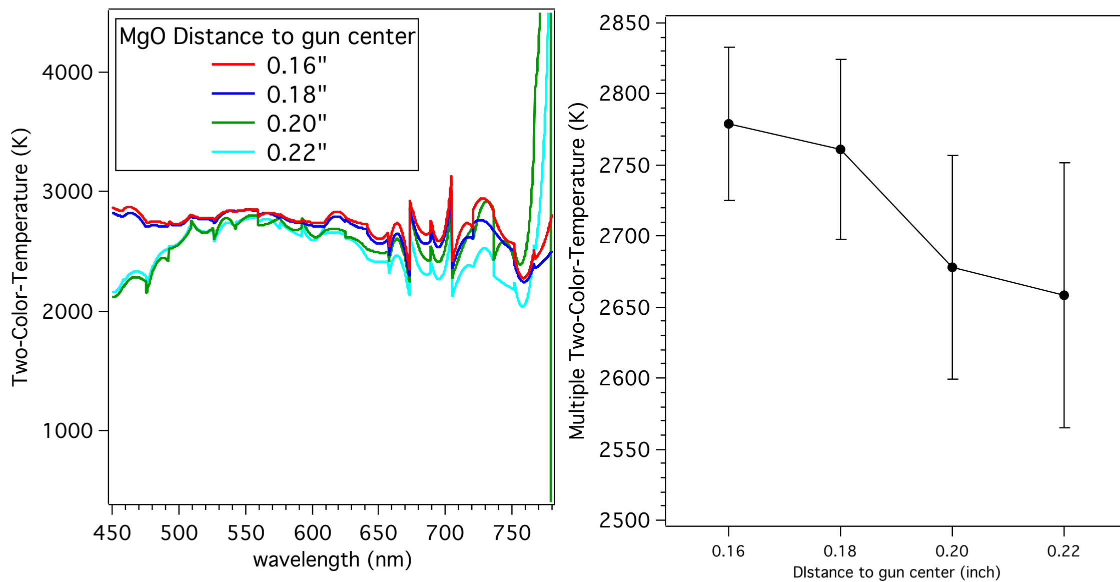

Figure A.4 Two-Color-Temperature reading from MgO demonstration. Left: X-axis is the average wavelength (± 15 nm) used to calculate Two-Color-Temperature and Y-axis is the calculated Two-Color-Temperature. Right: X-axis is the thermal couple temperature reading and Y-axis is the average of Two-Color-Temperature with the standard deviation as the error bar.

A1.5 Discussions and future work:

Why do we want to fit a short range instead of fit the whole spectrum range with the Planck’s equation? Fitting the whole spectrum with Planck’s equation is time consuming but viable with the computing power nowaday. However, by fitting the

spectrum, we can only get one temperature indication without the spectral relationship. We will lose a lot of information comparing to the multiple two-color-temperature method.

There are multiple applications to fully utilize this method. We are going to develop a more rigorous experiment using the above-developed technique. With a set of X-Y linear slide, we should be able to probe the temperature of the torch. We are also able to install two more thermal couples on the specimen to measure the thermal conductivity of the interested materials at the MHD working temperature range.

By carefully quantify the absolute irradiance and compare with the Planck's law, we can directly measure the materials spectral emissivity and the temperature relationship. In the future, once the spectral emissivity has been determined, one can prepare optics and CCD detectors that fit the desired wavelength and so the low cost customized two-color pyrometers can be made accordingly.

Reference

[1] D. M. Rowe, (1995).

[2] G. N. Hatsopoulos and E. P. Gyftopoulos, *Thermionic Energy Conversion* (MIT Press, Cambridge, 1973).

[3] R. J. Rosa, *Magnetohydrodynamic Energy Conversion* (McGraw-Hill, New York, 1963).

[4] V. K. Rohatgi, Bull. Mater. Sci. **6**, 71 (1984).

[5] R. C. Woodside, (2017).

[6] M. J. Hernandez, L. A. Cabrera, O. Vidana, M. Chaidez, and N. D. Love, in *54th AIAA Aerosp. Sci. Meet.* (American Institute of Aeronautics and Astronautics, Reston, Virginia, 2016).

[7] H. K. Bowen, *Ceramics for Coal-Fired MHD Power Generation* (Elsevier, 1979).

[8] E. G. Acheson, J. Franklin Inst. **136**, 279 (1893).

[9] G. Rudins, *U. S. and USSR MHD Electrode Materials Development* (1974).

[10] W. E. Young and E. W. Frantti, *Development, Testing and Evaluation of MHD Materials and Component Designs* (Pittsburgh, 1975).

[11] *Final Report On The Joint U.S.-U.S.S.R. Test of The U.S. MHD Electrode System In The U-02 Facility-Phase II* (Pittsburgh, 1977).

[12] J. W. Sadler, J. A. Dilmore, J. A. Kuszyk, J. Bein, A. G. Eggers, J. Lempert, D. L. Black, E. W. Frantti, B. R. Rossing, L. H. Cadoff, E. L. Kochka, and S. J. Schneider, *Development , Testing and Evaluation of MHD Materials and Component Designs Quarterly Report* (Pittsburgh, 1978).

[13] J. L. Bates, *Final Report on the Joint U.S.-U.S.S.R. Test of the U.S. MHD*

Electrode System in the U-02 Facility - Phase III (Pittsburgh, 1979).

[14] J. L. Bates and D. D. Marchant, *Development of Materials for Open-Cycle Magnetohydrodynamics (MHD): Ceramic Electrode , Final Report* (Richland, 1986).

[15] *Monthly Energy Review - September 2016* (2016).

[16] P. A. Kistler-De Coppi and W. Richarz, Int. J. High Technol. Ceram. **2**, 99 (1986).

[17] J. B. Casady and R. W. Johnson, Solid. State. Electron. **39**, 1409 (1996).

[18] A. H. Rashed, editor , *Properties and Characteristics of Silicon Carbide* (Decatur, TX, 2002).

[19] W. Wesch, Nucl. Instruments Methods Phys. Res. Sect. B Beam Interact. with Mater. Atoms **116**, 305 (1996).

[20] R. RIEDEL, G. MERA, R. HAUSER, and A. KLONCZYNSKI, J. Ceram. Soc. Japan **114**, 425 (2006).

[21] G. Fritz and B. Raabe, Zeitschrift Für Anorg. Und Allg. Chemie **286**, 149 (1956).

[22] S. Yajima, J. Hayashi, and M. Omori, Chem. Lett. 931 (1975).

[23] S. YAJIMA, Y. HASEGAWA, K. OKAMURA, and T. MATSUZAWA, Nature **273**, 525 (1978).

[24] P. Colombo, G. Mera, R. Riedel, and G. D. Sorarù, J. Am. Ceram. Soc. **93**, no (2010).

[25] H. ICHIKAWA and T. ISHIKAWA, *Comprehensive Composite Materials* (Elsevier, 2000).

[26] E. Kroke, Y.-L. Li, C. Konetschny, E. Lecomte, C. Fasel, and R. Riedel, Mater. Sci. Eng. R Reports **26**, 97 (2000).

[27] R. Riedel, A. Greiner, G. Miehe, W. Dressler, H. Fuess, J. Bill, and F. Aldinger, Angew. Chemie Int. Ed. English **36**, 603 (1997).

[28] J. Chojnowski, M. Cypryk, and J. Kurjata, Prog. Polym. Sci. **28**, 691 (2003).

[29] E. Lara-Curzio, editor , *Mechanical Properties and Performance of Engineering Ceramics and Composites: Ceramic Engineering and Science Proceedings, Volume 26, Number 2* (John Wiley & Sons, Inc., Hoboken, NJ, USA, 2005).

[30] A. Saha, R. Raj, and D. L. Williamson, J. Am. Ceram. Soc. 060428035142017 (2006).

[31] (n.d.).

[32] S. Dushman, Phys. Rev. **21**, 623 (1923).

[33] C. Herring and M. H. Nichols, Rev. Mod. Phys. **21**, 185 (1949).

[34] E. L. Murphy and R. H. Good, Phys. Rev. **102**, 1464 (1956).

[35] M. (Mino) Green, *Solid State Surface Science.* (M. Dekker, 1969).

[36] R. Garg, N. Dutta, and N. Choudhury, Nanomaterials **4**, 267 (2014).

[37] E. B. Hensley, J. Appl. Phys. **32**, 301 (1961).

[38] E. A. Burgemeister, W. von Muench, and E. Pettenpaul, J. Appl. Phys. **50**, 5790 (1979).

[39] F. Ma, Synthesis and Characterization of Thermoelectric Oxides at Macro- and Nano-Scales, ProQuest Dissertations Publishing, 2015.

[40] W. A. Groen, J. G. van Lierop, and J. M. Toonen, J. Eur. Ceram. Soc. **11**, 353 (1993).

[41] Z. Zhou and C. Uher, Rev. Sci. Instrum. **76**, 023901 (2005).

[42] J. Boor, C. Stiewe, P. Ziolkowski, T. Dasgupta, G. Karpinski, E. Lenz, F. Edler,

and E. Mueller, J. Electron. Mater. **42**, 1711 (2013).

[43] R. N. Blumenthal and M. A. Seitz, in *Electr. Conduct. Ceram. Glas.*, edited by N. M. Tallan, 1st ed. (Marcel Dekker Inc., New York, 1974), pp. 36–168.

[44] R. N. Blumenthal, J. Coburn, J. Baukus, and W. M. Hirthe, J. Phys. Chem. Solids **27**, 643 (1966).

[45] T. B. Massalski and H. Okamoto, *Binary Alloy Phase Diagrams*, 2nd ed. (Materials Park, Ohio : ASM International, Materials Park, Ohio, 1990).

[46] C. C. Chang, Surf. Sci. **25**, 53 (1971).

[47] R. L. Gerlach and T. N. Rhodin, Surf. Sci. **19**, 403 (1970).

[48] C.-K. Choo, D. Suzawa, and K. Tanaka, Surf. Sci. **600**, 1518 (2006).

[49] L. V. Interrante, K. Moraes, Q. Liu, N. Lu, A. Puerta, and L. G. Sneddon, Pure Appl. Chem. **74**, 2111 (2002).

[50] A. J. Regis and L. B. Sand, Geol. Soc. Am. Bull. **69**, 1633 (1958).

[51] A. L. Hannam and P. T. B. Shaffer, J. Appl. Crystallogr. **2**, 45 (1969).

[52] J. F. Moulder, W. F. Stickle, P. E. Sobol, and K. D. Bomben, *Handbook of X-Ray Photoelectron Spectroscopy* (Perkin-Elmer Corp., Eden Prarie, 1992).

[53] K. Miyoshi and D. H. Buckley, Appl. Surf. Sci. **10**, 357 (1982).

[54] T. Nelis and R. Payling, *Glow Discharge Optical Emission Spectroscopy - A Practical Guide* (Royal Society of Chemistry, 2003).

[55] M. F. Richardson, J. S. Hartman, D. Guo, and B. G. Winsborrow, Chem. Mater. **4**, 318 (1992).

[56] D. C. Apperley, R. K. Harris, G. L. Marshall, and D. P. Thompson, J. Am. Ceram. Soc. **74**, 777 (1991).

[57] H. Harima, Microelectron. Eng. **83**, 126 (2006).

[58] Y. Ward, R. J. Young, and R. A. Shatwell, J. Mater. Sci. **39**, 6781 (2004).

[59] B. Román-Manso, E. Domingues, F. M. Figueiredo, M. Belmonte, and P. Miranzo, J. Eur. Ceram. Soc. **35**, 2723 (2015).

[60] H.-Y. Ryu, Q. Wang, and R. Raj, J. Am. Ceram. Soc. (2010).

[61] N. J. Lee, J. W. Yoo, Y. J. Choi, C. J. Kang, D. Y. Jeon, D. C. Kim, S. Seo, and H. J. Chung, Appl. Phys. Lett. **95**, 222107 (2009).

[62] A. A. Brown, L. J. Neelands, and H. E. Farnsworth, J. Appl. Phys. **21**, 1 (1950).

[63] B. S. Rump and B. L. Gehman, J. Appl. Phys. **36**, 2347 (1965).

[64] R. D. Larrabee, J. Opt. Soc. Am. **49**, 619 (1959).

[65] (n.d.).

[66] K. Zakeri, T. R. F. Peixoto, Y. Zhang, J. Prokop, and J. Kirschner, Surf. Sci. **604**, L1 (2010).

[67] L. E. Davis, (1976).

[68] B. J. Hopkins and J. C. Rivière, Proc. Phys. Soc. **81**, 590 (1963).

[69] H. B. Wahlin and L. V. Whitney, Phys. Rev. **50**, 735 (1936).

[70] T. Takahashi, H. Tokailin, and T. Sagawa, Phys. Rev. B **32**, 8317 (1985).

[71] B. K. Tsai, R. L. Shoemaker, D. P. DeWitt, B. A. Cowans, Z. Dardas, W. N. Delgass, and G. J. Dail, Int. J. Thermophys. **11**, 269 (1990).

[72] W. Zhigang, Infrared Phys. **33**, 313 (1992).